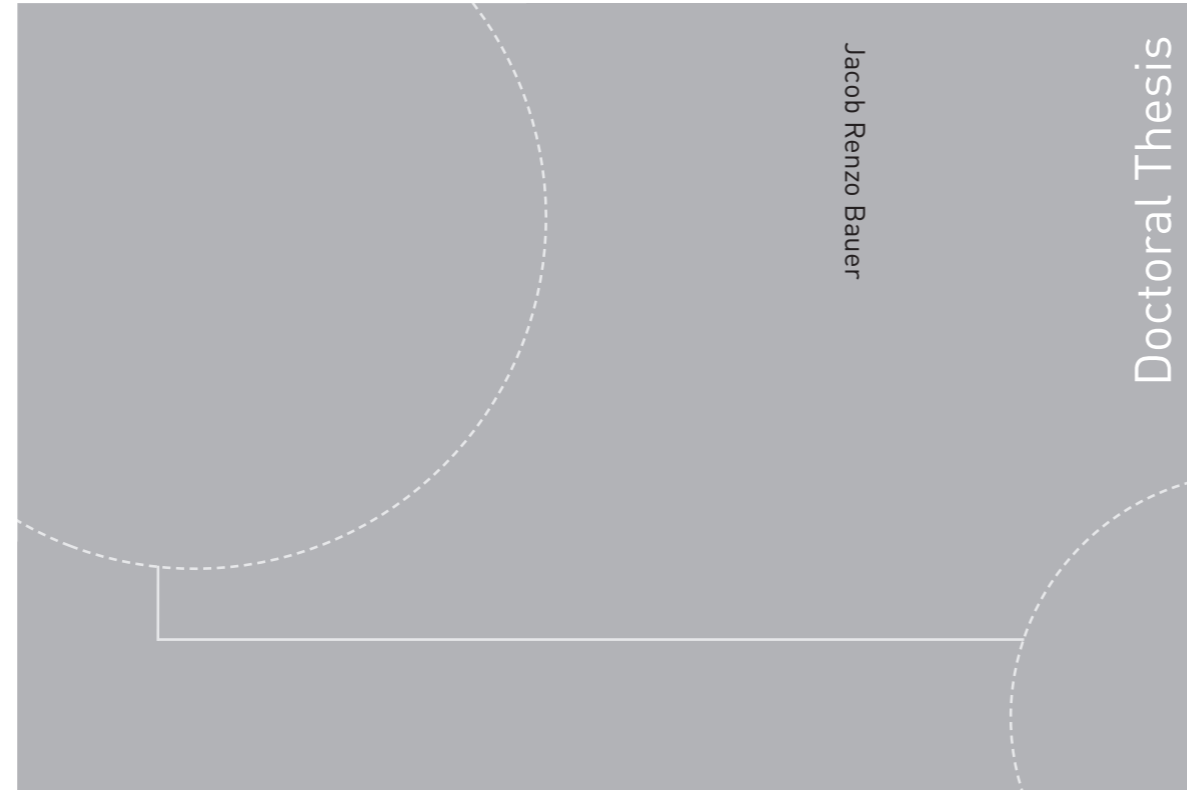


ISBN 978-82-326-4464-3 (printed version)
ISBN 978-82-326-4465-0 (electronic version)
ISSN 1503-8181



Doctoral theses at NTNU, 2020:55

Jacob Renzo Bauer

Spectral filter array cameras as a diagnostic skin imaging tool

Doctoral theses at NTNU, 2020:55

NTNU
Norwegian University of
Science and Technology
Faculty of Information Technology
and Electrical Engineering
Department of Computer Science

Jacob Renzo Bauer

Spectral filter array cameras as a diagnostic skin imaging tool

Thesis for the degree of Philosophiae Doctor

Gjøvik, March 2020

Norwegian University of Science and Technology
Faculty of Information Technology
and Electrical Engineering
Department of Computer Science



Norwegian University of
Science and Technology

NTNU

Norwegian University of Science and Technology

Thesis for the degree of Philosophiae Doctor

Faculty of Information Technology
and Electrical Engineering
Department of Computer Science

© Jacob Renzo Bauer

ISBN 978-82-326-4464-3 (printed version)

ISBN 978-82-326-4465-0 (electronic version)

ISSN 1503-8181

Doctoral theses at NTNU, 2020:55



Printed by Skipnes Kommunikasjon as

Declaration of Authorship

I, Jacob Renzo Bauer, hereby declare that this thesis and the work presented in it is entirely my own. Where I have consulted the work of others, this is always clearly stated.

Signed:

(Jacob Renzo Bauer)

Date: 17th February 2020

Abstract

Skin is the human's largest organ and has many vital functions including protection from pathogens, temperature regulation, touch sensation, vitamin D synthesis and protecting the water inside the body. It does not only protect the body from the environment but also carries information about the health of individuals.

Diagnosis and monitoring of skin and vital functions measured in non-contact is a broad field of research. Measuring vital signs, monitoring oxygenation and skin diagnosis can benefit from spatially resolved images of the tissue. Standard three-channel colour imaging provides the ease of use and acquisition speed for a clinical setup but lacks the spectral resolution to identify specific narrow bands of interest containing the essential information. Spectral imaging has been used to quantify diagnostically relevant physical properties of living tissue but suffers from slow acquisition speed and time delays between the acquisition of different bands. Recent sensor development has led to so-called spectral filter array (SFA) cameras, which combine the acquisition speed and ease of use of standard RGB imaging with the spectral resolution of spectral cameras. To utilise all the benefits of this new imaging modality, additional processing steps are required. This thesis explores SFA imaging in the context of skin diagnosis, and the imaging is enhanced with physical skin simulation models.

Skin models based on Monte Carlo simulation allow change and control over optical properties and resulting spectral reflectance from skin can be recorded. The simulated spectral reflectance with known optical properties is used in three different ways within this research. First, they are tested, by studying the impact of the optical properties on a resulting colour patch. This provides a better understanding of the relationship between colour shade and different combinations of optical properties. Secondly, the simulations are used to enhance the interpretability of spectral measurements regarding important physical skin properties with diagnostic value. This approach is applied to two different spectral filter array cameras and an RGB imager in conjunction with multiple LEDs. Thirdly, skin

simulations are performed to generate an exhaustive spectral reflectance database, for training and enhancement of spectral reconstructions of skin reflectance. This specialised database covers a wide range of physically, but not physiologically possible optical properties.

Different spectral imagers in the visual and near-infrared spectrum are applied to measuring oxygenation spatially resolved in living tissue. Additionally, a processing framework is proposed for spectral filter array cameras. This framework combines several SFA camera-specific processing steps and shows transferability to other cameras. It is tested by comparing oxygenation estimations from both a visual range (VIS) and a near-infrared (NIRS) spectral filter array camera with the de facto clinical standard in an upper arm occlusion test.

Finally, this work proposes a framework for selecting and testing SFA cameras for skin diagnosis tasks without the need of (extensive) clinical studies. This framework could aid in the development of SFA cameras for specific tasks and explores currently commercially available models for skin oxygenation measurements. In the future, it can be expected that spectral filter array cameras will become cheaper and more common. This work establishes a solid foundation for applying this new versatile form of spectral imaging in the context of skin diagnosis. Both general practitioners, dermatologists and, anesthesiologists can benefit from an easy to use, spatially resolved, real-time oxygenation measurement tool.

Acknowledgments

I would not have been able to carry out my research without the relentless help of my supervisors: Rudolf Verdaasdonk and Jon Yngve Hardeberg. Both helped me to develop as a scientist and as a person and I want to thank you for everything.

Special gratitude belongs to Jean Baptiste Thomas, who has a way to ask the questions that need to be answered and always helps to clear things up. John Klaessen's years of experience in the field of clinical research and his attitude to help me on my journey deserve special acknowledgment! Having had the chance to sit down with one of the greats in the field of biomedical optics has made an invaluable impact and I want to thank Steve Jacques for taking the time and inviting me to Portland. Not even a snow storm could keep your wisdom at bay and I cherish the lessons learned forever. I would also like to thank Ton van Leeuwen for taking me into his department at the AMC in Amsterdam and Maurice Aalders for his valued feedback and open nature about joining the forensics team in the basement.

Of course, I would like to thank my parents Michael and Susanne Bauer, who have helped me throughout my life and whenever needed as role models, advisors, inspirations and support throughout all stages of my life. I thank my sister Jenny Bauer for the great relationship we have and her support whenever needed and I wish her and Nico all the best and more for the years to come. Anete my girlfriend has helped me to maintain a good spirit and shows me day in and day out what is important in life putting the Ph.D. in perspective. I am excited for all the years to come and thank you for being there for me.

Of course, I want to thank all of my collaborators in Amsterdam namely Arnoud and Diederick, who showed me the medical scientific perspective. My time and life would not be the same without the infamous Lunch boys, Alex, Fabian, Jim, Omar and Martin, who filled the Vumc and Amsterdam with life and laughter. I consider meeting you one of the most important outcomes of my Ph.D. since I have found friends for life. The friendship with you always helped to put the struggles of the Ph.D. in perspective and it is great to spend time with you. Also, my friends at the

AMC in Amsterdam have had a great impact on this work. Not only in the way I was welcomed in the group, but also because of the friends I made. Especially Leah, who was not only my office neighbor she is always open for a mental escape from the Ph.D. and at the same time up for in-depth discussion with a beer after a hard day at work. Xavier has helped me with his sharp mind to reflect on many of the concepts and it was always great to discuss topics with him or spend some of our free time together exploring all sorts of ideas.

The friendship with my Ph.D. fellows namely Ahmed Mohammed and Mohib Ullah not only showed me a unique perspective into completely different backgrounds but also opened my eyes and I am often in awe about their determination, drive, and understanding. More friends for life, whom I wish all the best in the future and hope to share many more moments.

Of course, I would like to thank the Colourlab and everybody involved for providing a stimulating and great environment for science. Especially Marius Pedersen, who always has an open door if he can spend a moment to discuss the logistical inquiries of a Ph.D. project. I would also sincerely thank Irina, Fereshteh, Helena, Aland, Majid, Davit, Michael, and Congcong for always being open for a good conversation and the positivity whenever needed! Also, Peter Nussbaum has helped me immensely during the final phase of my Ph.D. by just reminding me of the fact that the Ph.D. is, indeed manageable.

This thesis is part of the IQ-MED: Image Quality enhancement in MEDical diagnosis, monitoring and treatment project and funded by the Research Council of Norway under project no. 247689. I hereby acknowledge the financial support from the Research Council of Norway.

Contents

Declaration of authorship	iii
Abstract	v
Acknowledgments	vii
I Overview	1
1 Introduction	3
1.1 Motivation	3
1.2 Aims and research questions	5
1.3 List of published papers	8
1.3.1 Original contributions	9
1.3.2 Roles of the authors	9
1.4 Thesis organization	11
2 Background	13
2.1 Skin	13
2.1.1 Skin anatomy and physiology	13
2.1.2 Skin optical properties	15
2.1.3 Skin modeling	19
2.2 Spectral imaging	20

2.2.1	Illumination	22
2.2.2	Spectral filter array cameras	22
2.3	Processing	24
2.3.1	Preprocessing	24
2.3.2	Interpretation	25
2.3.3	Visualisation	26
2.4	Medical Applications	27
2.4.1	Skin imaging	27
2.4.2	Vital signs	28
2.4.3	Occlusion test	29
3	Summary of included papers and contributions	31
3.1	Introduction	31
3.2	Paper A: Skin color simulation - review and analysis of available Monte Carlo-based photon transport simulation models	32
3.2.1	Abstract	32
3.2.2	Motivation	33
3.2.3	Methods	33
3.2.4	Results	33
3.2.5	Conclusions	34
3.3	Paper B: Optical skin assessment based on spectral reflectance estimation and Monte Carlo simulation	34
3.3.1	Abstract	34
3.3.2	Motivation	35
3.3.3	Methods	35
3.3.4	Results	35
3.3.5	Conclusions	35
3.4	Paper C: A Spectral Filter Array Camera for Clinical Monitoring and Diagnosis: Proof of Concept for Skin Oxygenation Imaging	35
3.4.1	Abstract	36
3.4.2	Motivation	36
3.4.3	Methods	36
3.4.4	Results	37
3.4.5	Conclusions	37

3.5	Paper D: Towards real-time non-contact spatial resolved oxygenation monitoring using a multispectral filter array camera in various light conditions	37
3.5.1	Abstract	37
3.5.2	Motivation	38
3.5.3	Methods	38
3.5.4	Results	38
3.5.5	Conclusions	38
3.6	Paper E: An Evaluation Framework for Spectral Filter Array Cameras to Optimize Skin Diagnosis	39
3.6.1	Abstract	39
3.6.2	Motivation	39
3.6.3	Methods	39
3.6.4	Results	40
3.6.5	Conclusions	40
3.7	Paper F: The vascular occlusion test using multispectral imaging: a validation study. The VASOIMAGE study.	40
3.7.1	Abstract	40
3.7.2	Motivation	40
3.7.3	Methods	40
3.7.4	Results	41
3.7.5	Conclusions	41
4	Discussion	43
4.1	Connections between the included papers	43
4.2	<i>RQ1</i> : How to use Monte Carlo simulation to improve the interpretation of measured skin reflectance data?	45
4.3	<i>RQ2</i> : How to use SFA imaging systems for oxygenation level measurements?	47
4.4	<i>RQ3</i> : How to select the correct spectral filter array camera and how to guide development?	50
4.5	<i>RQ4</i> : Can SFA cameras actually be used in the clinic?	53
4.6	Summary of the main limitations	54
5	Conclusion and perspectives	55
5.1	Conclusion	55

5.2 Perspectives	56
Bibliography	58
II Original Papers	71
Paper A: Skin color simulation - review and analysis of available Monte Carlo-based photon transport simulation models	73
Paper B: Optical skin assessment based on spectral reflectance estimation and Monte Carlo simulation	81
Paper C: A Spectral Filter Array Camera for Clinical Monitoring and Diagnosis: Proof of Concept for Skin Oxygenation Imaging	93
Paper D: Towards real-time non contact spatial resolved oxygenation monitoring using a multi spectral filter array camera in various light conditions	118
Paper E: An Evaluation Framework for Spectral Filter Array Cameras to Optimize Skin Diagnosis	131
Paper F: The vascular occlusion test using multispectral imaging: a validation study.	154

Part I

Overview

Chapter 1

Introduction

1.1 Motivation

The human skin is the largest organ and protects our body from external threats like heat, infection, impact and harmful radiation. The skin is affected by our health, mood, diet, age, well-being, and visual inspection of the skin is an ancient and widely used form of health assessment.

Visual inspection allows minimally invasive large scale non-contact diagnosis of disease, decreasing the infection risk, and avoiding weakening or hurting patients. This is especially important for critical care patients, new-borns and situations with high risks of infections.

The skin itself should be assessed for skin cancer, inflammations, and other skin pathology's and carries relevant systematic information about the health condition for health monitoring. Visual diagnosis is subjective to the examining physician and objective and quantitative tools are desirable and can aid physicians. Optical diagnosis is based on the interaction of light with living tissue. The color of the reflected light from the skin contains chemical and physiological information.

One technological equivalent to visual diagnosis is digital imaging. Digital imaging allows objective measurement of light reflected from the surface of an object. It provides a two-dimensional image that allows spatial interpretation of the reflected light signal. Standard three-channel (RGB) imaging systems acquire three wide bands along the visual spectrum of light. These wide bands can lack the spectral resolution to sense small changes in the spectral signature and are usually limited to the visual spectrum of light.

Multispectral imaging is a technique to acquire multiple narrow spectral bands of a scene to increase the spectral resolution. Different approaches have been developed and used in the medical field including liquid crystal tuneable filters, filter wheel cameras, and tuneable illumination imaging systems. All of these approaches sample the spectrum temporally, which introduces short delays in the moment of acquisition for each of the spectral bands. Spectral bands are acquired in sequence with these techniques rendering snapshot image capture impossible. This makes these techniques less suitable for capturing dynamic processes.

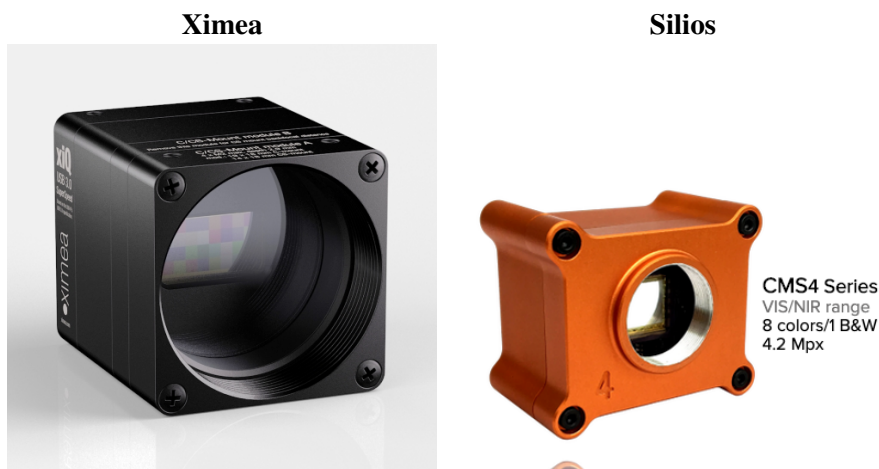


Figure 1.1: Examples of commercially available spectral filter array cameras. Ximea [1] (on the left). Silios [2] (on the right).

The recent development in sensor technology-enabled so-called spectral filter array cameras (with commercial examples in Figure 1.1). Each pixel of this type of camera has a unique spectral sensitivity curve and acts as a spectral filter. Therefore, each of the sub-pixels or pixels represents one wavelength allowing the reconstruction of a full spectral image. This captures both spectral and spatial aspects of the scene in a snapshot. It could allow physicians to distinguish between small changes in the spectral reflectance signature and can exceed the visual range of the spectrum. The special architecture of the sensors requires hardware aware processing of the data and adequate methods to analyze the data in a medically relevant context.

General practitioners and dermatologists are facing increasing amounts of patients. Easy to use non-contact imaging techniques could be beneficial to aid in tackling the increasing amounts of patients and provide an objective, sterile way of measuring. Telemedicine is also of increasing importance especially in areas where

specialists are rare or far away. For telemedicine, it is important to acquire dense data sets and provide the physicians with detailed information about the patient. Spectral filter array imagers could be beneficial for these applications.

1.2 Aims and research questions

This research aims to provide additional tools for physicians to analyze the skin and visualize processes invisible to the human eye. In particular enabling spectral filter array cameras as a medical imaging modality, while maintaining acquisition speed, spectral and spatial resolution, ease of use and versatile applicability of this new technology. Skin simulations are used as a tool aiding the interpretation of measured data and used to create controlled data sets. The thesis is centered around the principles of imaging and focused on the estimation of physiological properties from skin images. Skin imaging is a diverse field of research and this study focuses on skin oxygenation as the main application.

The main contributions of this work fall within the triangle of imaging, skin (as the object) and processing and medical applications in the center, this is illustrated in Figure 1.2. All three elements are investigated to help develop tools for physicians with concrete medical applications. Spectral imaging is used as the main mode of data acquisition.

Images of the skin face the challenge to provide physiologically relevant information. This process is not trivial and often referred to as the inverse problem. Specific knowledge of skin light interaction serves as a way to select bands of interest and aims to enhance the interpretability of images of the skin. Monte Carlo simulation, in particular, allows to numerically simulate optical properties and spectral reflectance of skin. Objective measurements of the color of skin, interpretation, and quantification of chemical and physiological parameters provide additional value for physicians. With processing tailored to the image acquisition and utilizing specific knowledge about skin optics via simulations, the image analysis is enhanced for medical applications.

The overall goal of this research is to develop new imaging tools for physicians with clinical value. To achieve this goal different aims were formulated to guide the research.

The first aim is to use computational simulations of optical properties of the skin to improve imaging. Ideally the models could be used to generate skin spectra with known optical properties in a controlled environment. These controlled simulations could then be used for training and testing and to guide the design of spectral skin imaging devices. It is then the aim to utilize these models in conjunction with new types of imaging methods.

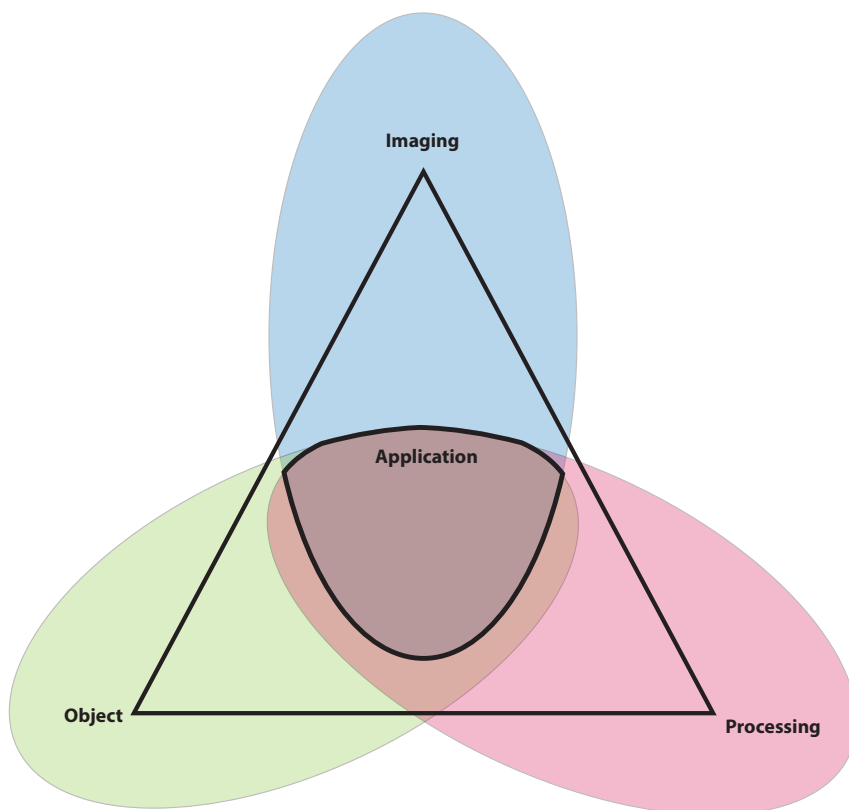


Figure 1.2: Triangle of imaging, processing and object aiming towards specific applications.

The second aim is to establish spectral filter array cameras, which combine acquisition speed, spatial and spectral resolution as a viable medical imaging modality. Specific processing is required to obtain a spectral image cube that can be analyzed and useful for physicians. This framework should apply to many instances of spectral filter array cameras and this research also aims to test this.

The final aim is to provide tools that can be used to guide design and optimize spectral filter array imagers for specific applications and to provide a comparison of currently commercially available cameras. This can be useful for other research to get an overview of existing spectral filter array techniques and should provide a tool to develop this novel technique further. Lastly it should be studied how useful SFA cameras are for physicians and in a clinical setup.

From these aims four research question (*RQ*) can be formulated and are presented

here:

RQ1: How to use skin simulations to improve the inter operation of measured skin reflectance data?

RQ2: How to use spectral filter array cameras efficiently for medical skin imaging?

RQ3: How to select spectral filter array cameras for specific applications and what to focus on for further development?

RQ4: How useful are SFA cameras in a clinical setup?

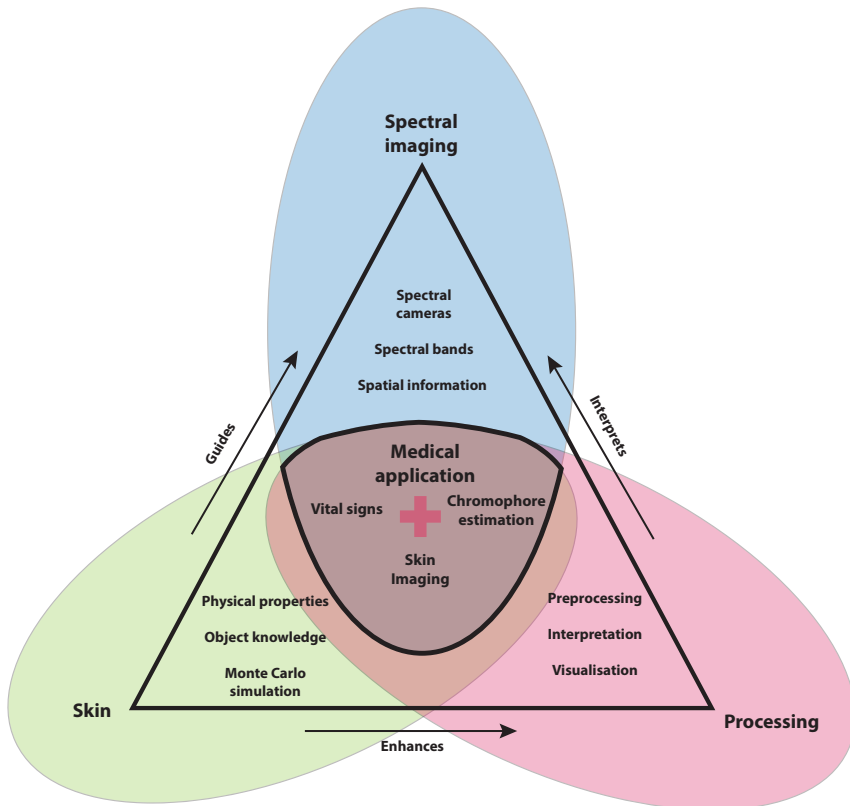


Figure 1.3: Concrete organisational triangle of spectral imaging, processing, and skin. Illustrating the specific application.

Figure 1.3 shows the above-mentioned triangle with examples of the aspects studied in this thesis and their connections. Spectral imagers can be used, among other

applications, to monitor vital signs, provide chromophore maps and, to visualize the oxygenation levels spatially resolved. The main medical applications studied in this research is the estimation of oxygen levels in the skin.

1.3 List of published papers

This research is represented in six papers. All are published and available online. A list of the papers included in this thesis is provided below. These six papers are included and constitute the core of this thesis. **Paper F** is as clearly stated a collaborative effort with medical doctors from the Vrije Universiteit Amsterdam medical center. The contributions by the author to this work will be clearly stated in Chapter 3 which provides a summary of each paper. Figure 1.4 provides an overview of the locations of the papers in the organisational triangle. **Paper A** focused on Monte Carlo skin simulation, **Paper B, C and D** exploring spectral imaging, **Paper E** proposing a framework for SFA cameras, and **Paper F** showing a medical application of the research.

List of included papers:

Paper A Jacob R. Bauer; Marius Pedersen; Jon Y. Hardeberg; and Rudolf M. Verdaasdonk; “Skin color simulation - review and analysis of available Monte Carlo-based photon transport simulation models,”; CIC25, *25th Color and Imaging Conference: Color Science and Engineering Systems, Technologies, and Applications*, 2017, Lillehammer, Norway.

Paper B Jacob R. Bauer; Jon Y. Hardeberg; and Rudolf M. Verdaasdonk; “Optical skin assessment based on spectral reflectance estimation and Monte Carlo simulation,”; Proceedings of SPIE Volume 10057, *Multimodal Biomedical Imaging XII* 1005703; Event: SPIE BIOS, 2017, San Francisco, California, United States.

Paper C Jacob R. Bauer; Arnoud A. Bruins; Jon Y. Hardeberg; Rudolf M. Verdaasdonk; “A Spectral Filter Array Camera for Clinical Monitoring and Diagnosis: Proof of Concept for Skin Oxygenation Imaging” *Journal of Imaging* 2019, 5, 66.

Paper D Jacob. R. Bauer; Karlijn v. Beekum; John H.G.M Klaessens; Herke J. Noordmans; Christa Boer; Jon Y. Hardeberg, and Rudolf M. Verdaasdonk; Towards real-time non contact spatial resolved oxygenation monitoring using a multi spectral filter array camera in various light conditions; Proceedings of SPIE Volume 10489, *Optical Biopsy XVI: Toward Real-Time Spectroscopic Imaging and Diagnosis*; Event: SPIE BIOS, 2018, San Francisco, California, United States.

Paper E Jacob R. Bauer; Jean-Baptiste Thomas; Jon Y. Hardeberg and Rudolf M. Verdaasdonk; “An Evaluation Framework for Spectral Filter Array Cameras to Optimize Skin Diagnosis” *Sensors* 2019, 19(21), 4805.

Paper F Arnoud A. Bruins; Diederik G.P.J. Geboers; Jacob R. Bauer; John H.G.M. Klaessens; Rudolf M. Verdaasdonk; Christa Boer; “The vascular occlusion test using multispectral imaging: a validation study.” *Journal of Clinical Monitoring and Computing* (2020).

1.3.1 Original contributions

Paper A can be considered an overview of three Monte Carlo methods for tissue optics simulation. Additionally the paper provides a visualization technique by simulating camera responses to spectra simulated with different optical configurations. **Paper B** is a proof of concept for a low cost spectral imaging device in combination with Monte Carlo simulations to retrieve oxygenation measurements. It showcases the combination of spectral estimation techniques in conjunction with Monte Carlo models to extract skin optical properties from reflectance measurements. **Paper C** explores a spectral filter array camera as a non contact oxygenation measurement and addresses unique preprocessing steps for this novel spectral imaging modality. These processing steps are developed into a framework and tested in a clinical setup. **Paper D** tests the transferability of the developed framework with a spectral filter array camera in the near infrared region. Both showcasing the validity of this spectral region for oxygenation measurements and showing the adaptability of the developed framework for other camera instances. **Paper E** can be considered a further abstraction of the developed framework and allows a complete investigation into most suitable spectral filter array cameras for specific biomedical optics tasks. This can be used as a guideline for the development of application specific spectral filter array cameras and as a complete overview of all aspects that need to be considered if applying these cameras in the medical domain. **Paper E** applies the complete SFA setup in a clinical research environment in collaboration with medical doctors. While **Paper C** describes the technical details **Paper E** describes the medical implications and tests the proof of concept clinically.

1.3.2 Roles of the authors

Paper A Jacob Renzo Bauer was responsible for conceptualization, carrying out the research, writing of the manuscript, creation of the figures and validation of the research results. All Monte Carlo Simulations were performed and submission handled by Jacob Renzo Bauer. The work was presented at CIC by Jacob Renzo Bauer as a poster presentation. Marius, Pedersen and Jon

Y., Hardeberg and Rudolf M. Verdaasdonk were supervising the work and reviewing the manuscript prior to submission.

Paper B Jacob Renzo Bauer was responsible for conceptualization, carrying out the research, writing of the manuscript, creation of the figures and validation of the research results. The work was presented at SPIE by Jacob Renzo Bauer as a conference presentation. Jon Y. Hardeberg and Rudolf M. Verdaasdonk were supervising the work and reviewing the manuscript prior to submission.

Paper C Jacob Renzo Bauer was responsible for conceptualizing, carrying out the research, implementation of python code, writing of the manuscript, creation of the figures, validation of the research results and the corresponding author for the review process. All revisions were done by Jacob Renzo Bauer. Arnoud A. Bruins provided medical background and validation and carried out the patient measurements. Measurement protocol and handling of the spectral camera was co developed by Jacob Renzo Bauer and Arnoud A. Bruins. Jon Y. Hardeberg and Rudolf M. Verdaasdonk were supervising the work and reviewing the manuscript prior to submission.

Paper D Jacob Renzo Bauer was responsible for conceptualizing, carrying out the research, writing of the manuscript, creation of the figures and validation of the research results. The work was presented at SPIE by Jacob Renzo Bauer as a conference presentation. Karlijn v. Beekum carried out measurements under supervision by Jacob Renzo Bauer and John H.G.M. Klaessens. Additional analysis software used in the research was implemented by Herke J. Noordmans and Jacob Renzo Bauer. John H.G.M. Klaessens, Jon Y., Hardeberg and Rudolf M. Verdaasdonk were supervising the work and reviewing the manuscript prior to submission. Christa Boer and Rudolf M. Verdaasdonk provided the spectral camera for this research.

Paper E Jacob Renzo Bauer was responsible for conceptualizing, carrying out the research, implementation of python code, writing of the manuscript, creation of the figures, validation of the research results and the corresponding author for the review process. All revisions were done by Jacob Renzo Bauer. Jean-Baptiste Thomas co-developed the concept for this research. Jean-Baptiste Thomas, Jon Y. Hardeberg and Rudolf M. Verdaasdonk were supervising the work and reviewing the manuscript prior to submission.

Paper F This paper can be considered the medical extension of Paper C. Jacob Renzo Bauer developed the technical solution and contributed to the creation of figures, validation of the research results and revision of the technical

parts of the paper. All implementations in python and the spectral camera measurement concept and its data analysis were performed by Jacob Renzo Bauer. Arnoud A., Bruins and Diederik G.P.J., Geboers were responsible for carrying out the research, writing of the manuscript and Arnoud A., Bruins was the corresponding author for the review process. John H.G.M, Klaesens, Rudolf M. Verdaasdonk and Christa, Boer were supervising the work and reviewing the manuscript prior to submission.

1.4 Thesis organization

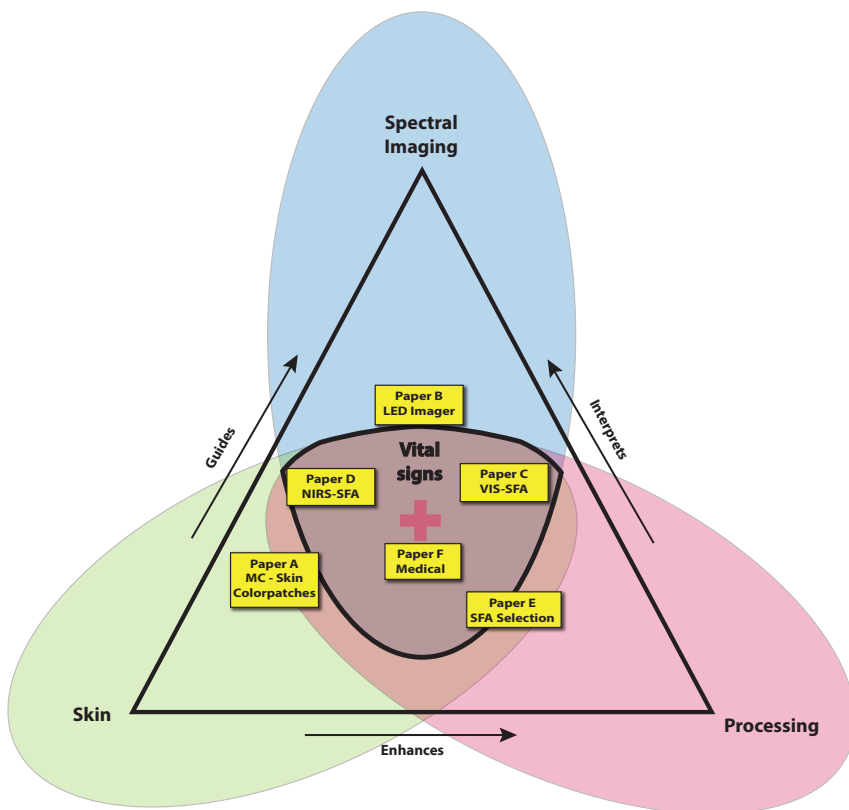


Figure 1.4: Overview of the included papers organized in to the triangular structure of skin, processing and spectral imaging.

This thesis provides context and background for clinically relevant imaging and diagnostics using spectral filter array cameras in particular. It is intended to provide context for the papers published during this research. The thesis has two main Parts. For most readers **Part I Overview** will provide a more readable text. **Part**

II Original Papers consists of reprints of all papers included in this thesis.

Part II has five chapters: The introduction Chapter 1 motivates the study in Section 1.1 formulates the research aims and Research Question (*RQ*) in Section 1.2, provides a list of the published and included papers in Section 1.3, and finally provides this structure of the thesis in Section 1.4.

The background Chapter 2 is organised around the triangle illustrated in Figure 1.3 and introduces skin, spectral imaging, processing, and medical applications. The interdisciplinary nature of the topics covered resulted in an attempt for each paper to be "stand-alone" and they provide extensive background information for readers of multiple fields. Therefore, the background included in this document is not exhaustive and is a starting point and overview for all the topics covered. Each section provides literature references for further reading.

Chapter 3 provides a summary of the included papers and is composed of one section for each of the published and included papers.

Chapter 4 is a discussion and organised around the *research questions (RQ)* formulated in Section 1.2. Conclusions with a future outlook for the research are presented in Chapter 5.

Chapter 2

Background

This background chapter is included to provide information to appreciate the contributions and topics covered in this thesis. It is not the intention to cover all topics in-depth, but rather to provide an overview and starting point. Each of the papers included in this thesis also contains a significant background, due to their wide and interdisciplinary audiences. The background is organised around the three pillars of this research introduced in Figure 1.3, skin as the main object of measurement, spectral imaging as the tool for acquisition and processing as the way to make use of the acquired data.

2.1 Skin

The main subject of investigation in this research is the complex tissue skin. It is important to understand the basics of skin anatomy, physiology, and physics (skin optical properties), which are in-fact intertwined. The skin is the largest organ and a protective layer against temperature, radiation, mechanical impact, infection and dehydration [3], [4]. Other than protection, skin has two other functions, namely regulation and sensation. All of these functions are represented in the physiology of skin and impact its optical properties directly.

2.1.1 Skin anatomy and physiology

The three-layer skin model is a simplified, but commonly used model of skin [3], [7] explaining the main functional components. Each of the layers presented in this work is the combination of multiple sub-layers.

Epidermis can be subdivided into five sublayers from the surface: stratum corneum, stratum lucidum, stratum granulosum, stratum spinosum and stratum basale with

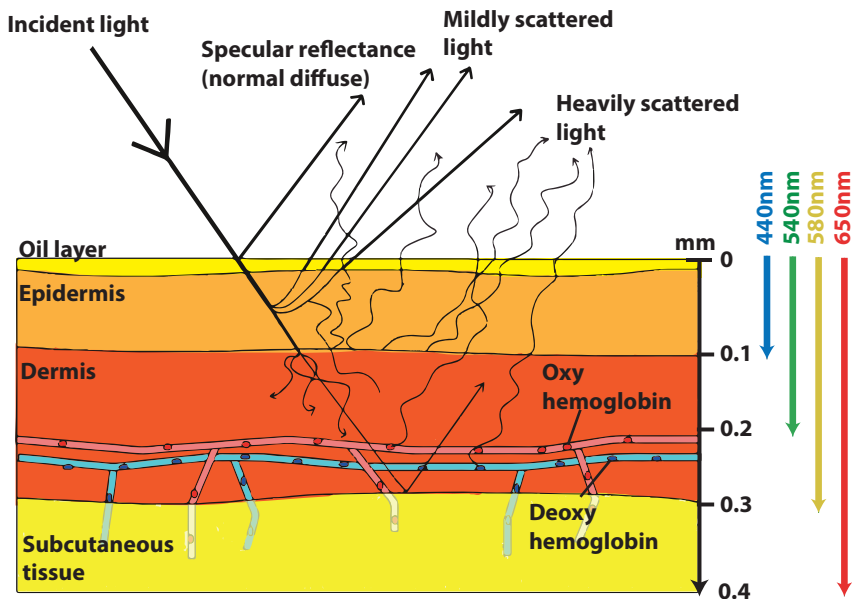


Figure 2.1: Overview of skin layers and penetration depths of different wavelengths into the the tissue [5]. Penetration depths from [6].

different functions. The thickness of the epidermis depends on the body location, age, ethnicity and dietary habits, but it is typically from $50\mu m$ to $200\mu m$. Essentially the epidermis forms skin cells or keratinocytes in the stratum basale and transports them outward towards the skin surface. The stratum spinosum contains many of the newly formed keratinocytes, Langerhans and Merckels cells that protect against infections [3]. This basale layer also contains optically important melanocytes that are responsible for the creation of melanin. Melanin is the main absorber of UV light in skin and the concentration of melanin strongly influences the skin color [8]. Common values for the coverage of the epidermis by melanosomes varies from 1.3 % – 6.3 % for lightly pigmented adults, 11 % – 16 % for moderately pigmented adults and 16 % – 43 % for darkly pigmented adults [8]. Stratum granulosum contains more keratinocytes moving towards the surface of the skin. The stratum lucidum only exists at the palm of the hands and sole of the feet and is a thicker protective layer of keratinocytes [9]. The outermost layer is the stratum corneum and consists mainly of dead keratinocytes cells. It is the first protective layer against infection, mechanical impact and prevents the body from drying out.

The **Dermis** layer of skin is the thickest (1 – 4mm) and most complex layer of skin containing, hair follicles, sweat glands, sensory nerve systems, blood vessels and,

connective tissue [10]. It provides the nourishment for the upper layers through interconnected blood vessels throughout the dermis [11]. The sensation of touch and thermal changes also stems from the dermis. Hair follicles originate in the dermis region and the hair grows through the epidermis to the surface providing additional protection from radiation and thermal insolation. Oxygen is delivered through the blood vessel network present in the dermis and diffused into the lower epidermal region.

The final layer considered for this research is the so-called **subcutaneous tissue** which is an additional thermal insulator and shock absorber consisting of mainly fat cells. Subcutaneous Tissue is the third layer of skin it can be up to 3 cm thick [8]. It mainly consists of fat cells, which reflects most of the visual range of light to the upper skin layers [8]. This increases the absorption events in the dermis and epidermis layers of skin, since the light passes through the both layers twice.

Figure 2.1 provides an overview of the three main layers and the penetration depth of different wavelengths.

2.1.2 Skin optical properties

Skin optical properties are directly connected to the anatomy and physiology of skin. If light is considered as a near-normal ray incident on the skin surface a portion of the light is reflected [12]. The characteristics of the reflected light are changed through interaction with the skin. Consequently, it contains information about skin characteristics based on intensity, wavelengths, polarization, coherence, etc [7]. In this work, we will focus on wavelength intensity distributions of reflected light.

Some of the light that enters the skin interacts with specific particles in the skin changing the intensity of some wavelengths based on absorption profiles of the particles. Penetration depth of visible light into skin depends on wavelength as shown in Figure 2.1 [6]. The longer the wavelength the deeper it penetrates the skin. After multiple scattering and absorption events, some of the light will be scattered back to the surface of the skin and make up the spectral reflectance and appearance of skin with information from different layers.

For an in-depth study of the complex optical properties the reader is referred to published work including [3], [4], [10]–[14] which also provide the basis for the following sections.

Absorption and scattering

The photons entering the skin are either absorbed, reflected, scattered or transmitted [15]. Concentrations of specific scattering or absorbing particles and the

wavelength of the incoming light define the path and interactions of the light within the tissue.

Absorption is the physical phenomenon in which a photon transfers its energy to matter. This transfer depends on resonance between the photon and the energy levels of molecules in the absorbing medium and is wavelengths dependent. A medium containing many absorbing particles can be described with $\mu_a = \rho_a \sigma_a$. ρ_a describes the volume density of particles in the medium and $\sigma_a = Q_a A$ the effective cross-section with Q_a as the absorption efficiency and A as the area of each particle [16]. The Lambert-Beer law is commonly used to describe the absorption in a homogeneous non scattering medium as [15], [17]: $I(x) = I(0)e^{-\mu_a x}$. $I(0)$ describes the incoming light and μ_a describes the absorption coefficient of the medium. The total absorption of a medium is the sum of all absorbing particles within the tissue. This energy transfer results in an excited energy state in the receiving molecule in the form of vibrations or electronic charges.

Scattering is the second physical interaction between photons and matter. When a photon hits specific particles in the medium it will be deflected. The size of the particle plays an important role in this interaction. For particles smaller than the wavelength of the photon the so-called Rayleigh scattering occurs. One commonly known phenomenon, caused by Rayleigh scattering is the blue shade of the sky. Since the air and atmosphere molecules scatter shorter wavelength stronger than longer wavelength more of the blue light reaches the surface of the earth. The interaction for particles larger than the wavelength is described through Mie theory. Mie scattering is predominantly forward scattering and common examples are clouds in the air or fat molecules in milk that scatter the light according to Mie theory.

The distance the light travels without hitting any scattering particles is called the mean free path l_s . This is usually described as a property of a medium with $l_s = 1/\mu_s$, where μ_s describes the scattering coefficient. The scattering coefficient monotonically decreases with increasing wavelength. In the case of diffuse skin reflectance, scattering needs to be examined based on countless scattering events. For these kinds of environments, it is important to consider the angular distribution or directionality of scattering. After each scattering event the direction of light will change depending on the amount and scattering efficiency of the present particles. The anisotropy factor describes the average cosine angle in which the photons travel after scattering events $g = \overline{\cos\Theta}$. Θ describes the scattering angle and the direction of the photon after the scattering event. In the case of skin, the scattering is predominantly forward scattering and a g is approximately 0.8 [14]. It is, however, wavelengths dependent and has been determined experimentally

with: $g(\lambda) = 0.62 + 29 \cdot 10^{-5} \cdot \lambda$ [16]. With λ describing the wavelength. After many scattering events the photons lose all information about incident angle, this is described as reduced scattering mean free path with: $l'_s = \frac{l_s}{1-g}$.

Reduced scattering coefficient μ'_s is therefore given with: $\mu'_s = \frac{l}{l'_s}$. A combined transport coefficient is then the addition of the reduced scattering coefficients and absorption coefficients of a medium with $\mu_{tr} = \mu'_s \mu_a$.

The combination of scattering and absorption is given for a medium with the attenuation coefficient $\mu_t = \mu_a + \mu_s$ [15].

Chromophores

The main particles in the skin tissue that interact through scattering and absorption with light are chromophores [18]. The Skin's diffuse reflectance spectrum is directly connected to the chromophore concentrations and locations in the tissue.

The unique absorption profile of the different skin layers defines a specific optical or spectral window [13] for diagnostics. Shorter wavelength in the ultraviolet range is absorbed by proteins, the longer wavelengths of the infrared region are absorbed by tissue and water contained in the skin. This leaves the visual and near-infrared region as an optical window. In this spectral region, the diagnostically less important particles absorb low amounts of light [19]. Blood, on the other hand, is a strong absorber in this NIR wavelength range. Low concentrations of blood in the outermost layers of the skin, allow the light to travel deeper into the tissue in this wavelength region. The outer layer epidermis contains another absorber: melanosomes and melanin [20].

These two absorbers, hemoglobin and melanin, play an important role in the skin color. Hemoglobin as the carrier of oxygen occurs in two different states: oxyhemoglobin and deoxyhemoglobin with different absorption spectra. Figure 2.2 shows the extinction coefficients or molar extinction coefficients ($e(\lambda)$) of the main chromophores and absorbers in skin tissue. The absorption of a medium depends on the concentration of absorbing particles in the medium. A typical μ_a (absorption) of blood can be calculated with:

$$\mu_a(\lambda) = 2.303e(\lambda) \cdot 150 \text{ (g/L)} / 64500 \text{ g (Hb/mole)},$$

which assumes 150 gHb/L and 64,500 gram as the molecular weight of hemoglobin [16].

Deoxyhemoglobin has an absorption maxima at around 430 nm, 555 nm and 760 nm, whereas oxyhemoglobin at 415 nm, 540 nm and 576 nm [19]. The low absorption at wavelength longer than 600 nm explains the red color of blood. Hemoglobin is

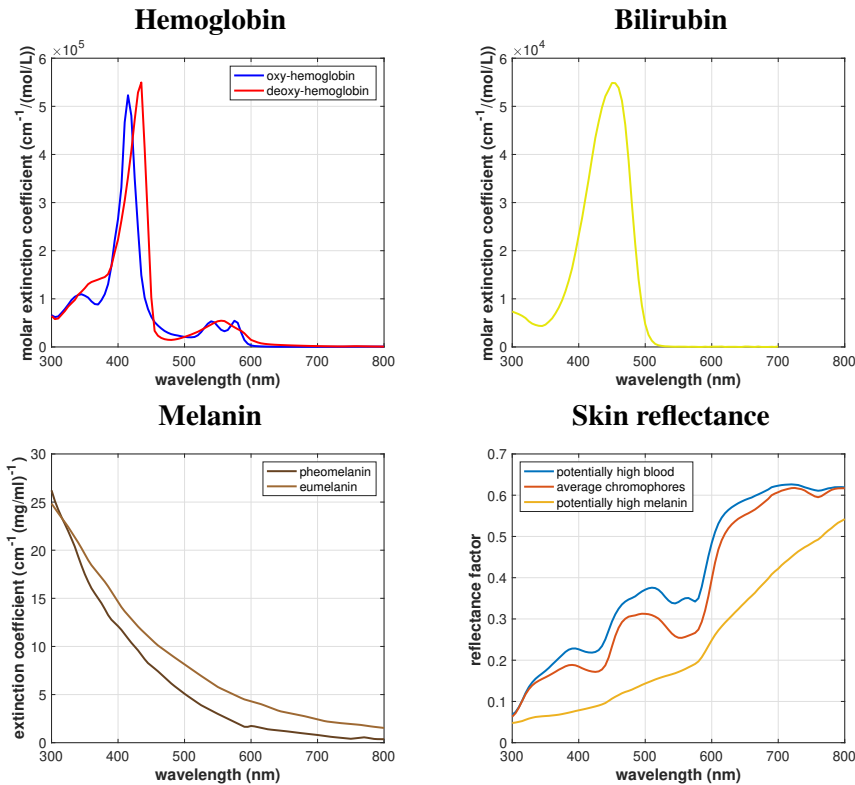


Figure 2.2: Molar extinction coefficient of oxy and deoxy hemoglobin (top left). Molar extinction coefficient of bilirubin (top right). Extinction coefficient of pheomelanin and eumelanin (bottom left). All data obtained from Jacques *et al.* [16]. Representative normalized skin reflectance spectrum (bottom right) data obtained from Cooksey *et al.* [21]

mainly found in the dermis typically at least 500 μm below the skin surface.

The strongest absorber in the visible range of light is melanin. Melanin is the colorant of hair, skin and eye color. Among humans, there are many different melanin concentrations in the skin ranging from very low in light Caucasians to very high in dark skin. These different types of skin colors were classified by Fitzpatrick *et al.* [22] into 6 different skin types.

Bilirubin is another absorbing chromophore and a decomposition product of hemoglobin. When skin is compressed due to impact blood can diffuse into the surrounding tissue. This misplaced blood will be decomposed by the body and bilirubin is a product of hemoglobin. As a result, bruises can occur yellowish, due to increased bilirubin concentrations in the tissue. These decomposition processes

are well studied and spectral reflectance can provide information about the age of bruises [23]. Bilirubin is also important in newborns, who lack the ability to further decompose the bilirubin. In high concentrations and if it enters the bloodstream it can be toxic and fatal. Neonatal jaundice is a common complication for newborns and a diagnostic tool to detect it early could save lives and has been studied intensively [24], [25].

2.1.3 Skin modeling

Skin modeling is the process of solving complex skin tissue light interactions numerically. In the process, spectral reflectance of skin with pre-defined optical properties can be generated in a controlled simulation environment. Three main models have been applied to skin analysis, straightforward models based on the Kubelka-Munk theory [26], diffusion approximation as described by Spott *et al.* [27] and Randeberg *et al.* [15], [28] and Monte Carlo based methods. Human skin modeling has also found importance in the computer graphics domain [13], [29]–[34]. In that domain, the general goal is to create realistic-looking skin in various situations based on advanced modeling [34]–[36]. The complexity of these models has been increasing in recent years with more and more realistic looking results [13], [29], [30], [32]–[34]. In this research, Monte Carlo models were utilized to simulate skin reflectance spectra with known optical properties.

Monte Carlo simulation

Monte Carlo simulation is a random sampling method numerically solving for physical quantities. This non-deterministic method is used in the context of optics as a ray-tracing method. Each photon propagates through the medium and the direction of propagation and interaction with other particles is based on probability distributions. Through simulation of thousands of photons skin tissue interaction with light can be simulated. This method is computationally demanding since each photon interaction needs to be calculated individually. In recent years the introduction of parallel computing and the computational power and design of graphical processing units (GPU) have significantly improved the computational time necessary for Monte Carlo simulations [37], [38]. These techniques allow simulating the independent photon particle interactions in parallel.

Monte Carlo simulation has been widely adopted to simulate light tissue interactions in the field of biomedical optics and has been studied intensively [24], [39]–[46].

The models have been used to simulate particles in different depth of the skin [47]. Monte Carlo Skin modeling has been often used to model the relationship between reflectance spectra and underlying chromophore concentrations [48].

To decrease the computational time Yamamoto *et al.* [49] have proposed the optical path length matrix method. The optical path length matrix is obtained by a probabilistic density histogram of the optical path length in skin based on Monte Carlo simulation. They report a decreased computational time of 26,000 times shorter than conventional Monte Carlo simulation. Naglic *et al.* [45] have proposed a combination of diffusion approximation and Monte Carlo simulation to overcome known inaccuracies of diffusion approximation and maintain fast processing.

For a comprehensive summary of the skin simulation tools used in this research reading Wang *et al.* [39] is recommended. Additionally, Atencio *et al.* [24] describes a practical application of the models and they provide the source code for the adapted simulation environment used for this research.

2.2 Spectral imaging

Imaging usually describes three-channel (RGB) digital imaging. The three color channels are based on mimicking the human visual system and provide accurate color reproduction for human observers. Imaging can also incorporate spectral information usually referred to as multispectral or hyperspectral imaging. Multispectral imaging has a lower number of bands compared to hyperspectral imaging.

In opposition to the commonly used three-channel digital imaging, multispectral imaging allows capturing more spectral bands in the same instance making it analogue to spectral measurements at each pixel. These spectral measurements are spatially resolved and provide a spectral map or spectral image cube of the scene.

Multiple techniques to measure these spectral image-cubes have been proposed. These include scanning methods where the spectral resolution is achieved through the temporal decomposition of the signal and recently proposed snapshot methods, where all bands are acquired in the same instance. The scanning and temporally resolved spectral imaging techniques include liquid crystal tunable filter (LCTF), acousto-optical filters (AOTF) and so-called filter wheel systems. Another big category of recent spectral imaging devices is a combination of selected illuminations and an imaging sensor. The illumination has multiple discrete narrow spectral bands and through sequential illumination of the object and consecutive image acquisition a spectral cube can be generated.

Most of the mentioned spectral imaging modalities rely on a temporal decomposition of the spectral signal. Recent sensor development resulted in so-called spectral filter array cameras. This is a new spectral imaging modality that allows acquiring a complete spectral image cube with one snapshot. Details of this particular spectral imaging modality will be discussed in the following Section 2.2.2.

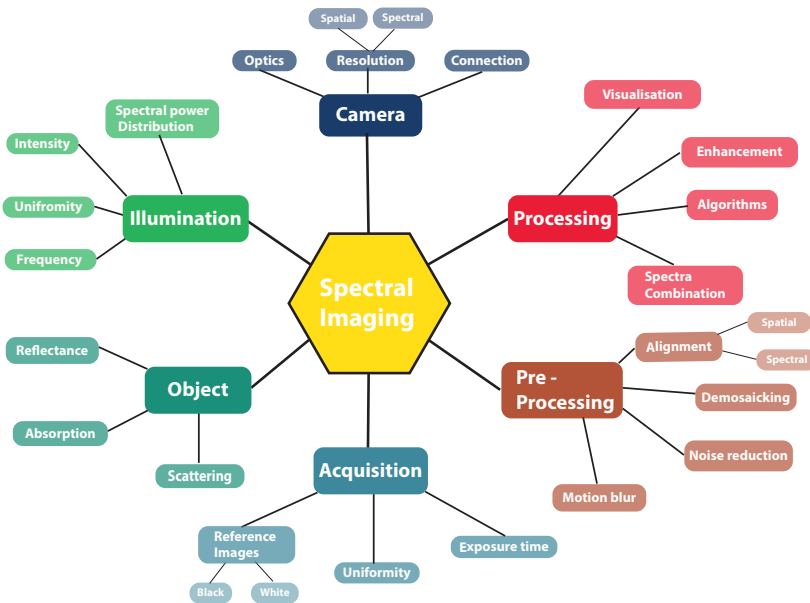


Figure 2.3: Overview of things to consider for spectral imaging.

Spectral imaging has some unique requirements and aspects that need to be specifically considered and Figure 2.3 provides an overview of these aspects. Some of these aspects interact with each other and need to be considered together. It includes six main aspects that need special attention: The camera or the imaging system used, acquisition parameters, illumination, object, preprocessing of the signal and finally the processing or the interpretation. Each of these has multiple aspects that need to be considered for the successful application of spectral imaging.

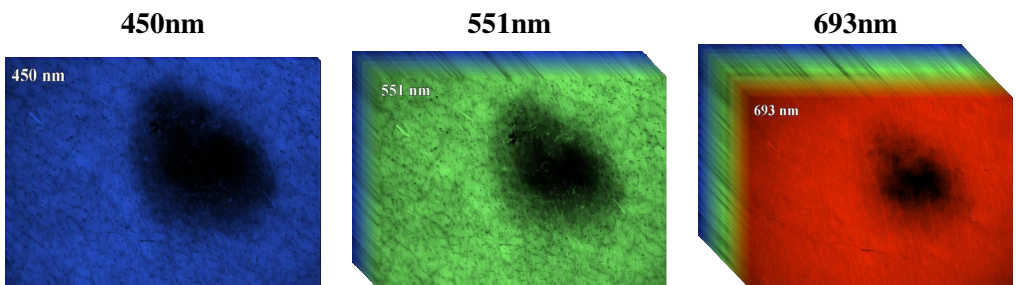


Figure 2.4: Different spectral bands of the same skin area, illustrating the wide range of information captured with multiple wavelengths. Image courtesy to Rudolf Verdaasdonk and Herke Jan Noordmans.

Figure 2.4 shows an illustration of the difference of information captured with different spectral bands. Each of the images is captured of the same area with different wavelengths sensed. The tissue light interaction differ depending on the wavelengths and therefore useful information can be gathered from these different spectral bands.

An overview of different spectral imaging techniques is provided by Hardeberg [50].

2.2.1 Illumination

Another important aspect to consider when designing spectral imaging measurements is the illumination. Both frequency and spectral power distribution can affect the measurements drastically. Since many of the spectral imaging techniques are based on temporal decomposition of the spectral signal it is important to select the illumination frequency adequately. The spectral power distribution should be selected as a smooth as possible and with adequate intensity at the bands of interest. The delivered energy should be as homogenous as possible over the spectral range of interest.

2.2.2 Spectral filter array cameras

A recent summary of spectral filter array cameras has been provided by Lapray *et al.* [51] and a review of this novel technique has been published by Hagen *et al.* [52].

Spectral filter array imaging is a new form of spectral imaging [53]. The core concept is based on a spectral filter pattern on top of a sensor similar to the conventional Bayer pattern. The increasing spatial resolution of sensors in recent years coupled with the advancement in interference filters allowed this new technology. Some of the spatial resolution is sacrificed for more spectral bands. The advancements in interference filters allow producing narrow spectral bands.

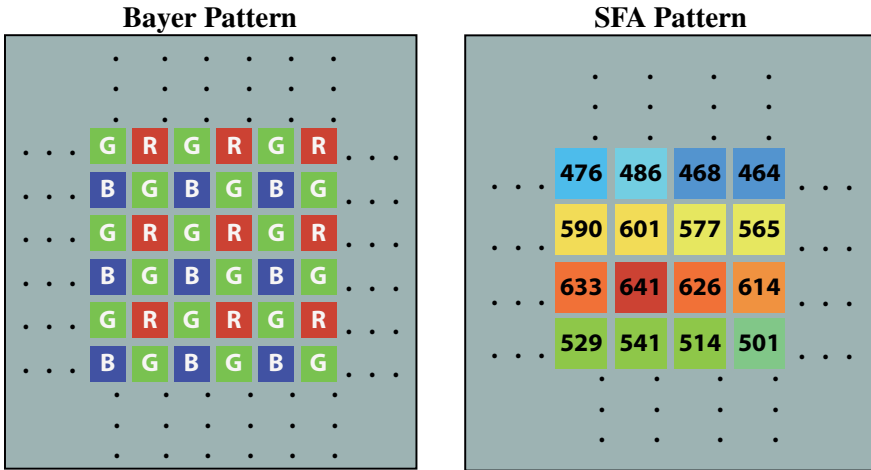


Figure 2.5: Illustration of standard RGB image sensor pixel pattern compared to spectral filter array image sensor patterns.

These narrow spectral bands allow more robust recognition of particular features in the skin spectrum this is illustrated in Figure 2.6. A normal skin reflectance spectrum is shown and juxtaposed with relative sensor sensitivities illustrating that the RGB sensor misses important features of the skin spectrum. The SFA camera on the other hand does pick up the difference in skin reflectance of the 540nm and 560nm wavelengths.

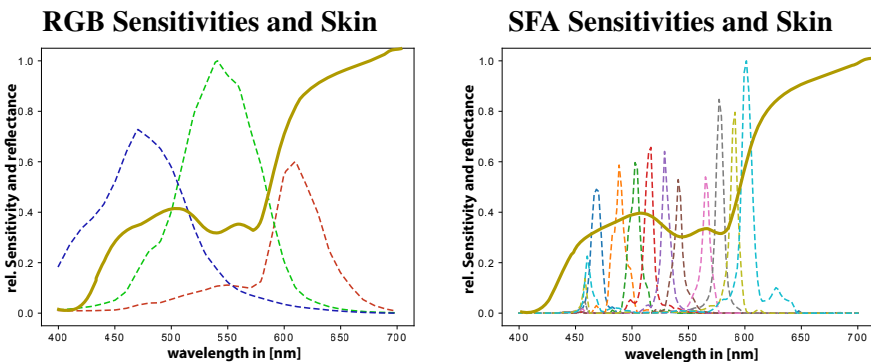


Figure 2.6: Illustration of standard RGB image sensor sensitivities compared to spectral filter array sensitivities, juxtaposed with the spectral reflectance of skin.

This new type of spectral imaging requires specific processing steps that will be touched upon in the next section.

2.3 Processing

Processing is an important step of the pipeline necessary to make data acquired with spectral imaging devices useful. These steps with different goals are usually included in common imaging pipelines. Usually, the signal is preprocessed, which includes calibration steps, corrections, and possibly noise handling. This is followed by an interpretation step where the measured data is processed into the domain of interest. And finally, the acquired data is visualized in a way that is use-full for the end-user. These steps are illustrated in Figure 2.7 and discussed in the next section.

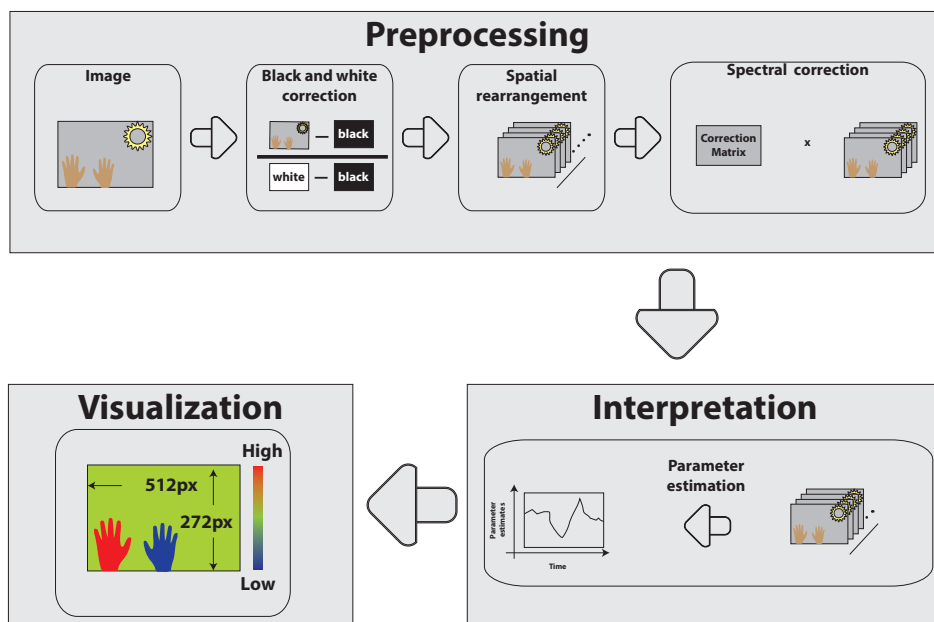


Figure 2.7: Overview of common processing steps

The details of the particular processes in each of the included articles can be found in the publications.

2.3.1 Preprocessing

Preprocessing is the first step in common imaging pipelines. Often the first step is to incorporate calibration steps like black and white corrections. The white correction can in some cases account for the spectral power distribution of the light sources and convert the measured signal to a reflectance signal. The black correction on the other hand is in order to suppress the impact of dark current noise. SFA cameras in particular require unique hardware-specific processing steps.

SFA specific preprocessing is necessary, since spectral filter array cameras are a unique spectral imaging modality. SFAs decompose the spectral signal spatially as opposed to most other spectral imaging techniques, which decompose the spectral information temporally. This spatial decomposition needs to be converted to a spectral imaging cube. Each slice of this imaging corresponds to one spectral band and the full spatial resolution of the sensor.

These sensors often based on Fabry-Pérot interference have second-order harmonics that need to be accounted for. The passing wavelengths depend on destructive and constructive interference, but the chosen wavelengths will always have a secondary wavelength peak that also interferes constructively. This results in two wavelengths peaks being transmitted. These second-order harmonics can be filtered out by large bandpass filters. Depending on the intended spectral sensitivity range of the imager the possibility for hardware-based filtering of these extra sensitivity peaks can be limited.

Some SFA cameras, therefore, require a spectral calibration which is equivalent to mathematically transposing the spectral sensitivities to new theoretical sensitivities correcting for the inadequacies. The new virtual filter bands are corrected of the second-order harmonics.

2.3.2 Interpretation

The interpretation step is important to transfer the measured data into useful information. It includes to transfer physical measurements into relevant parameters for the end user.

Spectral estimation or reconstruction is a common technique in the field of spectral imaging [54]–[58]. The goal is to reconstruct spectral reflectance curves from a limited number of bands. Generally, these estimation methods are based on inverting a common imaging model.

$$P_i = \int_{\lambda} E(\lambda)R_j(\lambda)Q_i(\lambda)d\lambda, \quad (2.1)$$

where P_i is the channel response of the i^{th} channel of the sensor. $E(\lambda)$ is the illumination spectral power distribution (SPD) per wavelength, $R_j(\lambda)$ is the spectral reflectance of sample j , and $Q_i(\lambda)$ describes the spectral sensitivity of the i th channel of the sensor. This equation is inverted and pairs of training reflectances and the camera responses to these training reflectances utilised to calculate a transformation matrix that minimises the error between reconstructions and the training data. The pre-calculated matrix can then be used to reconstruct spectra based on camera channel responses to a given spectral signal. Several different techniques to estimate this matrix have been proposed including the pseudo-inverse

method (least-square fitting) or linear least-square fitting in a lower-dimensional space (Imai–Berns method) [59]. Another widely used method that includes a possible noise term in the imaging model is called the Wiener estimation [55]–[57], [59]–[61] method.

Chromophore estimation is one processing step that can be applied to estimated or measured spectra. Chromophore concentrations are of clinical value for physicians. The concentration and location of specific chromophores, like melanin, can help physicians to distinguish between different skin pathologies. Measuring these concentrations with optical methods to avoid scaring, scarring and hurting the patient is beneficial. Spectral reflectances of skin have been used to estimate or measure the concentrations of particular chromophores. The differences in absorption of these particles allow distinguishing between different chromophores when measuring reflected light from a defined light source. Many different methods have been proposed to estimate these chromophores from the reflectance spectrum [28], [62]–[74]. Many of the approaches utilize ratios of specific spectral bands to emphasize differences in the absorption spectrum [73]. Other methods are based on solving equation systems to solve for a complex combination of given absorption spectra [72]. Inverse Monte Carlo [75] methods are based on the idea to simulate spectra with given optical properties and create lookup tables to find the best fit between measured spectrum and previously simulated spectrum. Other techniques are based on different photon transport models fitting the modeled spectra to measured reflectance spectra [28]. Often the Beer-Lambert law is modified or enhanced to account for scattering events [64]. Also, simple color measurements have been applied to chromophore estimation and correlations between color coordinates and specific chromophore concentrations have been formulated [67].

2.3.3 Visualisation

Another important aspect for clinicians is the visualisation of parameters they can use for diagnostics. These parameters can be invisible for the human eye or the physicians benefit from false color maps which are intuitive.

Chromophore maps are a common and well studied application of visualizations of the skin surface [70], [76]–[80]. They can visualize pigmentation [81], or provide color coded distribution maps as proposed by many groups including [70], [77]. These maps help the physicians to judge distributions of important chromophores and provides additional information about the skin surface.

2.4 Medical Applications

The final goal of this research is to develop new tools applicable for physicians in the field of skin imaging. A special focus is the measurement of oxygenation levels.

2.4.1 Skin imaging

Several different imaging modalities are applied to skin with unique use-cases for each of them. Optical coherence tomography (OCT) is a sophisticated imaging modality allowing to image into the skin tissue and visualize its structure [82], [83]. OCT is based on interference imaging resulting in a structural vertical cross-section of the skin and can even incorporate color information of the layers [84]. The penetration depth is in the order of 1mm with a few micrometer resolution.

Reflectance confocal microscopy (RCM) is another optical technique that provides high-resolution imaging of very small areas of the skin. RCM can be tuned to different penetration depth into the skin [85].

Dermatoscopy is the most widely used technique to examine skin and provides physicians with impressions of a couple cm in areas. These magnifiers of 10x to 400x suppress skins specular reflection and some provide digital images of important areas for the physicians [86].

Other commonly diagnostic measurements of the skin are performed as point reflectance measurements (spectroscopy) [87]. The reflected signal from the skin is measured as an average over an area of the skin tissue. This assumes skin as a homogeneous or uniform surface. The heterogeneity and spatial information about chromophore concentrations are lost. It can not be distinguished between dark skin with uniformly distributed higher melanin concentration or a localized lesion within the captured area. For dermatologists, this information can be beneficial. The shape of suspicious lesion is another indicator for dermatologists and carries diagnostic value.

Skin imaging, on the other hand, provides a spatially resolved measurement of the reflectance spectrum. Each pixel corresponds to a measurement and differences in location can be captured. It allows us to quantify the heterogeneity of skin and visualize the shapes of lesions. Many three-channel digital cameras have been applied in dermatology as techniques for tracking changes over time or to characterize and categorize different skin pathologies. In recent years recommendation systems have also been developed to show dermatologists different examples of their diagnoses in other patients based on digital images. The role of digital images for telemedicine and personalized medicine will also most likely increase

dramatically [88]. Standard three-channel digital images have the advantage to acquire a spatially resolved image of the pathology but do not capture subtle spectral differences.

Spectral skin imaging techniques have been applied to a variety of different applications [89]. For instance the severity or maliciousness of cancers have been studied using spectral imaging techniques [90]–[92], it has been applied for verification of effectiveness of treatments [93], for segmentation tasks in dermatology [94], cervical cancer screening [95], bruise analysis [47], cholesterol [96], skin lesions [97] and others.

Another application of spectral imaging is a relatively new field of study the so called spatial frequency domain imaging (SFDI) [63], [98]–[103]. This technique has been popularized in the medical field by Cuccia *et al.* [63], [99]–[102]. It is based on displaying spatial line patterns on the tissue and acquiring spectral images at the same time. Through some complex mathematical operations, the images of different spatial line patterns can then be decomposed into absorption and scattering images of the tissue. Separating these two components during the imaging process.

Some spectral filter array cameras have already been studied. First, commercially available models have been applied in studies to measure hemodynamics of brain tissue Pichette *et al.* [104], or oxygenation of skin tissue by Saager *et al.* [105].

An extensive hardware focused analysis of spectral imagers for biomedical applications is provided by Gutiérrez-Gutiérrez *et al.* [106]. The main focus of their work are the technical limitations including acquisition speed, efficiency, object plane curvature, spatial resolution, distortions, and noise. Another comprehensive emulation framework has been proposed by Saager *et al.* [107]. Saager *et al.* provide an emulation framework and an overview of the performance of different spectral imagers. They include two experiments a burn wound mouse model and an experiment concerning photoaging (sun exposure experiment). For all experiments, high-resolution spectral measurements using an SFDS system are required. Validation of the performance of SFA cameras is usually based on application-specific measurements [107].

2.4.2 Vital signs

Another area that benefits from non-contact measurement is the monitoring of vital signs. Four primary vital signs are of specific clinical importance quantifying the body's life-sustaining functions: Body temperature, blood pressure, pulse (heart rate) and respiratory rate are most commonly referred to as the main vital signs. Often the so-called oxygen saturation is added as a fifth vital sign quantifying the

oxygen saturation of the blood. The body maintains a stable oxygen saturation to keep tissue a-life. Clinically oxygen saturation is commonly measured with so-called pulse oximeters as a point measurement and quantified as a systematic value. The peripheral oxygen concentration of the blood is estimated using the absorption differences of oxygenated hemoglobin and deoxygenated hemoglobin [108].

2.4.3 Occlusion test

A widely used experiment to analyze oxygenation levels is the so called upper arm occlusion test (vascular occlusion test - VOT) [55], [109]–[113]. The blood delivery to the volunteer's hand is occluded by using an inflatable cuff on one of the upper arms. This occlusion results in reduced blood delivery to the hand. Tissue needs oxygen to survive and consumes the oxygen in the blood decreasing the total oxygen concentration in the blood. After a certain time has passed or until the oxygen concentration in the blood reaches a certain level the occlusion is released. Allowing the blood flow back into the hand and causing an oxygen overshoot for a short time. The behavior is illustrated in Figure 2.8. Three different phases can

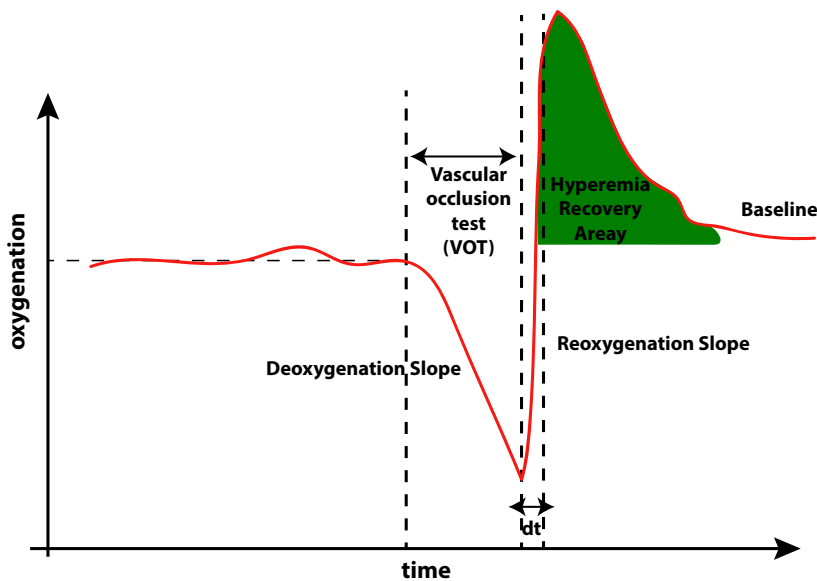


Figure 2.8: Example of oxygen concentration levels during the upper arm occlusion and shortly after the release of the inflatable cuff. Including the oxygen overshoot after release.

be described in the oxygenation pattern throughout the experiment. First, the so-called baseline oxygenation, represented in the beginning and during unprovoked

measurement. It is followed by the deoxygenation or desaturation slope invoked by the occlusion and inflation of the cuff. This time frame within the experiment is usually called the vascular occlusion test (VOT) and has been correlated with the health status of patients or as an indicator for complications during surgery or the application of anesthesia [109], [110]. The last phase of this VOT is the so-called reoxygenation or resaturation, where the oxygenation overshoots the baseline very rapidly after cuff deflation. After this, the hyperemic phase is the time frame where the oxygen levels decrease back to baseline. The area under the curve is also known as the hyperemia recovery area has been correlated to venal health [109] metrics. Finally, the oxygenation levels return back to the baseline. Since the behavior of oxygenation levels is well understood for this provocation it is a good experiment to test new oxygenation level estimation methods.

Chapter 3

Summary of included papers and contributions

The following chapter will summarize the included and published papers. All abstracts of the papers are included together with short sections of motivation, methods, results, and conclusion. The introduction section will provide an overview of the contributions and connections between the papers.

3.1 Introduction

As explained in the Chapter 1 all papers fall into a triangle spun from the object, the imaging technology and the processing of the image data. The medical application is the final goal for these processing steps and illustrated in the center of the triangle. The papers can be placed within this triangle as illustrated in Figure 1.4.

Paper A is mainly related to skin modeling utilizes some processing and has a small medical application. The skin modeling is studied to find a relation between optical properties and RGB camera values in a controlled setup. Different simulation environments are publicly available and the paper provides an overview. The skin modeling is also used to enhance the interpretation of spectra obtained with the different imagers introduced in **Papers B, C and D**.

Papers B, C, and D all fall into the imaging side, and focus on concrete imaging devices to acquire oxygenation level estimations from non-contact reflectance images during an upper arm occlusion experiment. In order to interpret the data from the imagers both processing and simulated skin spectra are utilized to enhance the interpretation. **Paper B** is focused on a multi-illumination prototypical spectral imaging system. This imager is then used for spectral reconstruction and the

estimated spectra are analyzed regarding the medical interpretability and in particular the estimation of oxygenation levels during the upper arm occlusion test. For **Paper C** a spectral filter array camera processing framework is proposed and used for the same diagnosis with a volunteer study including 58 volunteers. **Paper D** utilizes the same general framework with a spectral filter array camera in the near-infrared spectrum and shows the generality and transferability of the proposed framework.

In **Paper E** different spectral filter array cameras and an RGB camera are compared proposing a framework to guide the selection and design of spectral filter arrays. This paper builds upon simulations from **Paper A** since the simulation environment is extended to simulate 10.000 combinations of optical properties and to generate a training set of skin samples for spectral reconstruction. The proposed framework compares different commercially available spectral filter array models including theoretical Gaussian based filter sensitivities. All of the investigated models are compared regarding different metrics including an oxygenation level estimation metric. The influence of different data sets for training is also analyzed in this publication.

Paper F is the result of a collaboration with medical doctors and it analyses the same dataset as **Paper C** of 58 volunteers. The main information that is analyzed from the dataset is the venal health status of the volunteers. The framework first proposed in **Paper C** is used in conjunction with the same camera.

3.2 Paper A: Skin color simulation - review and analysis of available Monte Carlo-based photon transport simulation models

Jacob R. Bauer; Marius Pedersen; Jon Y. Hardeberg; and Rudolf M. Verdaasdonk; "Skin color simulation - review and analysis of available Monte Carlo-based photon transport simulation models,"; CIC25, *25th Color and Imaging Conference: Color Science and Engineering Systems, Technologies, and Applications*, 2017, Lillehammer, Norway.

3.2.1 Abstract

Optical assessment is a useful tool for non-invasive skin assessment avoiding scarring, time-delayed diagnosis, hurting, and inconvenience for patients and practitioners. This has led to the wide adaption of digital imaging and other optical technologies in dermatology. Many of these optical technologies lack quantifiabil-

ity, therefore, the reproduction, comparison or absolute meaning of measurements or images is an open challenge. Monte Carlo simulation for multi-layered turbid media provides an accurate tool for simulating the optical path of photons traversing in the skin and the diffuse spectral reflectance of skin. With this tool at hand the missing link between health metrics and measurable optical phenomena can be provided and it can help to establish optical assessment and digital images as a standard for health monitoring of skin. A number of publicly available simulation codes and several different approaches have been proposed. In this work, we give an overview of three Monte Carlo simulation tools and compare the different approaches. Furthermore, we will use Monte Carlo Simulations to generate different spectra based on varying optical properties and use these spectra to generate colour patches to analyse the impact of different optical properties on the resulting RGB colour patches.

3.2.2 Motivation

Monte Carlo simulation is a useful and well-known technique to simulate the optical properties of tissue. The simulation environment allows to specify particular chromophores in the skin and numerically simulate the light tissue interaction. This Paper aims to provide an overview of available Monte Carlo tissue simulation tools. Direct influence on skin color or shading in connection to specific chromophores is of great interest for physicians and a direct link between colour appearance and physiological properties would be useful. Therefore, the Paper explores the effects of chromophore concentrations on color patches generated from Monte Carlo simulations with defined chromophore concentrations.

3.2.3 Methods

The overview of different techniques is obtained by summarizing the state of the art tools and compiling an overview of the different methods that are publicly available. As a case study, several concentration levels of particular chromophores were simulated and color patches were generated from the resulting spectral reflectance curves. The color-patches assumed D65 lighting and were presented in the display sRGB colourspace.

3.2.4 Results

The color-patches confirm visually that particular chromophores influence the color of skin in different cardinal colour directions. Bilirubin influences mainly the blue-yellow axis, whereas higher melanin shifts the appearance towards the brown or darker shades of skin color. Increasing the hemoglobin or total blood volume shifts the color shades as expected towards the red region of the colourspace.

3.2.5 Conclusions

Chromophore color changes behave mainly as expected. New Monte Carlo simulation models are being developed and utilize the processing power of graphics processing units and an overview of these developments has been provided.

3.3 Paper B: Optical skin assessment based on spectral reflectance estimation and Monte Carlo simulation

Jacob R. Bauer; Jon Y. Hardeberg; and Rudolf M. Verdaasdonk; “Optical skin assessment based on spectral reflectance estimation and Monte Carlo simulation,”; SPIE Proceedings Volume 10057, *Multimodal Biomedical Imaging XII*; 1005703 (2017); Event: SPIE BIOS, 2017, San Francisco, California, United States.

3.3.1 Abstract

Optical non-contact measurements in general and chromophore concentration estimation in particular have been identified to be useful tools for skin assessment. Spectral estimation using a low cost hand held device has not been studied adequately as a basis for skin assessment. Spectral measurements on the one hand which require bulky, expensive and complex devices and direct channel approaches on the other hand which operate with simple optical devices have been considered and applied for skin assessment. In this study we analyse the capabilities of spectral estimation for skin assessment in form of chromophore concentration estimation using a prototypical low cost optical non-contact device. A spectral estimation workflow is implemented and combined with pre-simulated Monte Carlo spectra to use estimated spectra based on conventional image sensors for chromophore concentrations estimation and obtain health metrics. To evaluate the proposed approach we performed a series of occlusion experiments and examined the capabilities of the proposed process. Additionally the method has been applied to more general skin assessment tasks. Results obtained are both compared to chromophore estimations based on spectral measurements and to direct channel approaches. The proposed process provides a more general representation in form of a spectral image cube which can be used for more advanced analysis and the comparisons show good agreement with expectations and conventional skin assessment methods. Utilising spectral estimation in conjunction with Monte Carlo simulation could lead to low cost, easy to use, hand held and multifunctional optical skin assessment with the possibility to improve skin assessment and the diagnosis of diseases.

3.3.2 Motivation

Low cost handheld skin imaging tools could be useful for general practitioners (GP), dermatologists and other physicians. This work explores to combine spectral reconstruction from a prototypical spectral imaging device with simulations of tissue using Monte Carlo spectra. The simulated Monte Carlo spectra allow the calculation of physiologically relevant parameters from estimated spectra. A compact handheld non-contact multi-band LED illumination imaging device is used to acquire the data for reconstruction of full spectra.

3.3.3 Methods

Monte Carlo simulations are performed prior to the measurements with a variety of different configurations regarding the chromophore contents in the skin. The prototypical imaging device is based on an RGB sensor and six LEDs illuminating the scenes with different spectral. This multi-band imaging device is used to estimate full spectra and measurements of six volunteers are conducted during the upper arm occlusion test. The final estimated spectra are then used in conjunction with the Monte Carlo simulations to estimate chromophore concentrations among the volunteers.

3.3.4 Results

The combination of spectral estimation and prior simulation of chromophore concentration via Monte Carlo shows expected occlusion experiment results. Spectral estimation allows us to generate a full spectral cube from RGB+ data and the interpretability of these has been enhanced through Monte Carlo simulations.

3.3.5 Conclusions

Combining spectral reconstruction from an RGB imaging system with Monte Carlo simulations showed expected occlusion test results. The full spectral cubes could be used for other diagnoses, for which the accuracy of spectral estimation needs to be tested.

3.4 Paper C: A Spectral Filter Array Camera for Clinical Monitoring and Diagnosis: Proof of Concept for Skin Oxygenation Imaging

Jacob R. Bauer; Arnoud A. Bruins; Jon Y. Hardeberg; Rudolf M. Verdaasdonk; "A Spectral Filter Array Camera for Clinical Monitoring and Diagnosis: Proof of Concept for Skin Oxygenation Imaging" *Journal of Imaging* 2019, 5, 66.

3.4.1 Abstract

The emerging technology of spectral filter array (SFA) cameras has great potential for clinical applications, due to its unique capability for real-time spectral imaging, at a reasonable cost. This makes such cameras particularly suitable for quantification of dynamic processes such as skin oxygenation. This is useful, for instance, for assessment of the healing of burn wounds, and as an indicator of patient complications in the operating room. Due to their unique design, in which different pixels of the image sensor are equipped with different optical filters, SFA cameras require suitable image processing to obtain meaningful high-quality spectral image data, including spatial rearrangement, SFA interpolation, and spectral correction. In this Paper, the feasibility of a commercially available SFA camera for clinical applications is tested. A suitable image processing pipeline which is generalizable to other SFA cameras is proposed. As a 'proof of concept' a complete system for spatial dynamic skin oxygenation measurements is developed and evaluated. In a study including 58 volunteers, oxygenation changes during upper arm occlusion were measured with the proposed SFA system and compared with a validated clinical device for localized oxygenation measurements (INVOS 5100C-PA). The comparison of the INVOS and SFA results shows a good correlation for the relative oxygenation changes, which are of clinical value. The proposed processing chain for SFA cameras is thus shown to be effective for imaging relative oxygenation changes. It can be implemented in real-time and further developed to yield absolute spatial oxygenation measurements.

3.4.2 Motivation

In this work, we propose an imaging pipeline that solves limitations of spectral filter array cameras and shows their applicability to the medical field with a 58 volunteer upper arm occlusion comparison study. Comparative golden standard measurements are obtained with a clinically accepted oximeter. The main goal is to provide a straight forward processing pipeline for spectral filter array cameras and show the effectiveness of these cameras for oxygen level estimation. Oxygenation estimation is a clinically relevant measurement for physicians and provides a measurement of nutrition delivery to the living tissue, new ways of measuring this parameter in real-time with non-contact to the patient is useful.

3.4.3 Methods

The image processing pipeline is based on spatial rearrangement, spectral calibration and finally oxygenation estimation. Spectral calibration takes the unique spectral sensitivities of each of the channels into consideration and reduces spectral double lobes mathematically. The influence of this spectral calibration step

is shown regarding the spectral reconstruction accuracy. Finally, the spectral data from the camera is used to estimate oxygenation levels and compared to a clinical golden standard.

3.4.4 Results

The spectral reconstruction and image processing pipeline increase the spectral accuracy. Comparing the clinical golden standard oxygenation level measurement and the estimated estimates good agreement of the general shape of the curves was found. Additionally, some key features of the oxygenation curves were extracted and compared to the clinical golden standard device. For the 58 volunteer study, these showed lower correlations.

3.4.5 Conclusions

Spectral filter array cameras have the potential to be a powerful clinical imaging tool. Some of the challenges with this new imaging technique have been solved with the proposed transferable image processing pipeline. The agreement between estimated oxygenation curves was strong whereas correlation, between the key slope features was lower.

3.5 Paper D: Towards real-time non-contact spatial resolved oxygenation monitoring using a multispectral filter array camera in various light conditions

Jacob. R. Bauer; Karlijn v. Beekum; John H.G.M Klaessens; Herke J. Noordmans; Christa Boer; Jon Y. Hardeberg, and Rudolf M. Verdaasdonk; Towards real-time non-contact spatial resolved oxygenation monitoring using a multispectral filter array camera in various light conditions; SPIE Proceedings Volume 10489, *Optical Biopsy XVI: Toward Real-Time Spectroscopic Imaging and Diagnosis*; Event: SPIE BIOS, 2018, San Francisco, California, United States.

3.5.1 Abstract

Non-contact spatial resolved oxygenation measurements remain an open challenge in the biomedical field and patient monitoring. Although point measurements are the clinical standard until this day, regional differences in the oxygenation will improve the quality and safety of care. Recent developments in spectral imaging resulted in spectral filter array cameras (SFA). These provide the means to acquire spatial-spectral videos in real-time and allow a spatial approach to spectroscopy. In this study, the performance of a 25 channel near-infrared SFA camera was studied

to obtain spatial oxygenation maps of hands during occlusion of the left upper arm in 7 healthy volunteers. For comparison, a clinical oxygenation monitoring system, INVOS, was used as a reference. In case, of the NIRS SFA camera, oxygenation curves were derived from 2-3 wavelength bands with a custom made fast analysis software using a basic algorithm. Dynamic oxygenation changes were determined with the NIR SFA camera and INVOS system at different regional locations of the occluded versus non-occluded hands and showed to be in good agreement. To increase the signal to noise ratio, algorithm and image acquisition were optimised. The measurements were robust to different illumination conditions with NIR light sources. This study shows that imaging of relative oxygenation changes over larger body areas is potentially possible in real-time.

3.5.2 Motivation

This Paper can be considered as a proof of concept for using a spectral filter array camera operating in the near-infrared wavelengths regime for oxygenation level estimation. Melanin as the main absorber of the outer layer of skin is semi-transparent in the near-infrared wavelengths regime. This means that a spectral camera operating in that regime will be more suitable for oxygenation level estimation. Furthermore, wavelengths exceeding 800nm are not visible for the human eye and could allow implementation of oxygen estimation in the dark.

3.5.3 Methods

The unique spectral sensitivities of the camera were considered and a spectral calibration, correcting for overlaps within the sensitivities mathematically was applied. Spectral calibration was followed by a straight forward oxygen level estimation. A limited proof of concept experiment including six volunteers and upper arm occlusion with parallel clinical golden standard measurements was carried out using different light-sources. The resulting oxygenation level curves were then compared.

3.5.4 Results

Golden standard oxygenation levels and its estimations from the spectral filter array camera were in good agreement under different illuminations. The included control of the right hand which was not occluded within the experiment displayed no provocation of the oxygenation levels.

3.5.5 Conclusions

This work shows that the near-infrared regime is a valid regime for oxygenation level estimations. It is additionally robust regarding illumination and showed good agreement with the golden standard oximeter measurements.

3.6 Paper E: An Evaluation Framework for Spectral Filter Array Cameras to Optimize Skin Diagnosis

Jacob R. Bauer; Jean-Baptiste Thomas; Jon Y. Hardeberg and Rudolf M. Verdaasdonk; “An Evaluation Framework for Spectral Filter Array Cameras to Optimize Skin Diagnosis” *Sensors* 2019, 19(21), 4805.

3.6.1 Abstract

Comparing and selecting an adequate spectral filter array (SFA) camera is application-specific and usually requires extensive prior measurements. An evaluation framework for SFA cameras is proposed and three SFA cameras are tested in the context of skin analysis without the need for measurements. Spectral sensitivities and the number of bands are the main focus and spatial aspects are excluded. A skin optical model and skin spectral measurements are used in conjunction with known filter sensitivities for training and testing of a spectral reconstruction matrix. The quantitative comparison of the cameras is based on spectral reconstruction, colorimetric accuracy, and oxygenation level estimation differences. Specific spectral sensitivity shapes influence the results directly and a 9 channel camera performed best for spectral reconstruction metrics. Whereas Sensitivities at key wavelength influenced the performance for oxygenation level estimation the most. The proposed framework allows to compare and guide the development of application-specific spectral filter array cameras and provides recommendations for the case of skin analysis.

3.6.2 Motivation

This work aims to guide the selection and development and provides a processing pipeline for spectral filter array imagers. Selection criteria for spectral filter array cameras are application-specific, this is illustrated with the example of skin imaging. The influence of specific spectral sensitivity shapes and different spectral filter implementations need to be compared. A standardized way of comparison is amiss and this study aims to provide a possible framework.

3.6.3 Methods

Different spectral sensitivities of SFA cameras and idealized Gaussian sensitivities are considered. Through spectral estimation using varying training sets the cameras are compared regarding spectral reconstruction accuracy. As a specific application, the suitability of each of these cameras is tested for oxygenation level estimation.

3.6.4 Results

Spectral reconstruction accuracy is not directly analogous to estimating the oxygenation level. The RGB camera performed the worst if compared to multi-band spectral imaging devices. Specialized training sets had a positive effect on skin spectra estimation and spectral shapes are important for spectral reconstruction quality.

3.6.5 Conclusions

A framework for comparing different spectral filter array cameras has been proposed and tested with four available spectral cameras. Spectral sensitivity shapes influenced the spectral reconstruction stronger than sensitivities at key wavelengths, which in turn influences the oxygenation level estimation stronger.

3.7 Paper F: The vascular occlusion test using multispectral imaging: a validation study. The VASOIMAGE study.

Arnoud A. Bruins; Diederik G.P.J. Geboers; Jacob R. Bauer; John H.G.M. Klaessens; Rudolf M. Verdaasdonk; Christa Boer; “The vascular occlusion test using multispectral imaging: a validation study. The VASOIMAGE study” *Accepted in Journal of Clinical Monitoring and Computing (JCMC)*.

3.7.1 Abstract

This study aims to validate multispectral imaging (MSI) as a measure for microcirculatory perfusion. Vascular occlusion tests for fifty-eight volunteers were performed with an MSI and near-infrared spectroscopy in parallel and correlations calculated. Moderate correlation were found, that could be ascribed to differences in physiology of measurement areas.

3.7.2 Motivation

Multispectral Imaging (MSI) is a new, non-invasive method to continuously measure oxygenation and microcirculatory perfusion, validation on healthy volunteers has been limited. The present study aimed to validate the potential of multispectral imaging in the detection of microcirculatory perfusion disturbances during a vascular occlusion test (VOT).

3.7.3 Methods

Two consecutive VOT's were performed on healthy volunteers and tissue oxygenation was measured with MSI and near-infrared spectroscopy (NIRS). Correlations

between the rate of desaturation, recovery and the hyperemic area under the curve (AUC) measured by MSI and NIRS were calculated.

3.7.4 Results

Fifty-eight volunteers were included. The MSI oxygenation curves showed identifiable components of the VOT, including a desaturation and recovery slope and hyperemic area under the curve, similar to those measured with NIRS. The correlation between the rate of desaturation measured by MSI and NIRS was moderate: $r = 0.42$ ($p = 0.001$) for the first and $r = 0.41$ ($p = 0.002$) for the second test.

3.7.5 Conclusions

Our results suggest that non-contact multispectral imaging is able to measure changes in regional oxygenation and deoxygenation during a vascular occlusion test in healthy volunteers. When compared to measurements with NIRS, correlation of results was moderate to weak, most likely reflecting differences in physiology of the regions of interest and measurement technique.

Chapter 4

Discussion

In this chapter, we will discuss the logic behind selecting specific techniques and methods and provide more context for the progression of this research. The connections of the papers will be revisited and explained in detail. All research questions posed for this research project are revisited. Most of the initial research questions (*RQ*) have evolved and are reformulated here. The discussion should give the reader an answer to all of the research question according to the published papers. Limitations of the approaches are be pointed out and discussed.

4.1 Connections between the included papers

This research is from start to finish an **interdisciplinary** attempt to develop new imaging-based solutions with clinical value. Spectral reflectance of skin carries useful health metrics and is the main physical property that can be measured by imaging. The spectral reflectance has to be measured with the right equipment and and has to be interpreted to be of value for physicians. The connections between the papers are illustrated in Figure 4.1.

Skin modeling can be seen as a tool to enhance the interpretation of measured spectra regarding clinically relevant parameters like oxygenation levels. At the same time, it provides a simulation environment in which all skin parameters are controllable and allows to simulate meaningful data sets for data-driven learning algorithms. In this research, it has been used to enhance the interpretation of measured spectra and extract information of particular chromophores from tissue reflectance spectra, furthermore a data set of 10000 skin reflectances is generated and used for spectral reconstruction training.

Paper A studied Monte Carlo simulation as a commonly used skin modeling en-

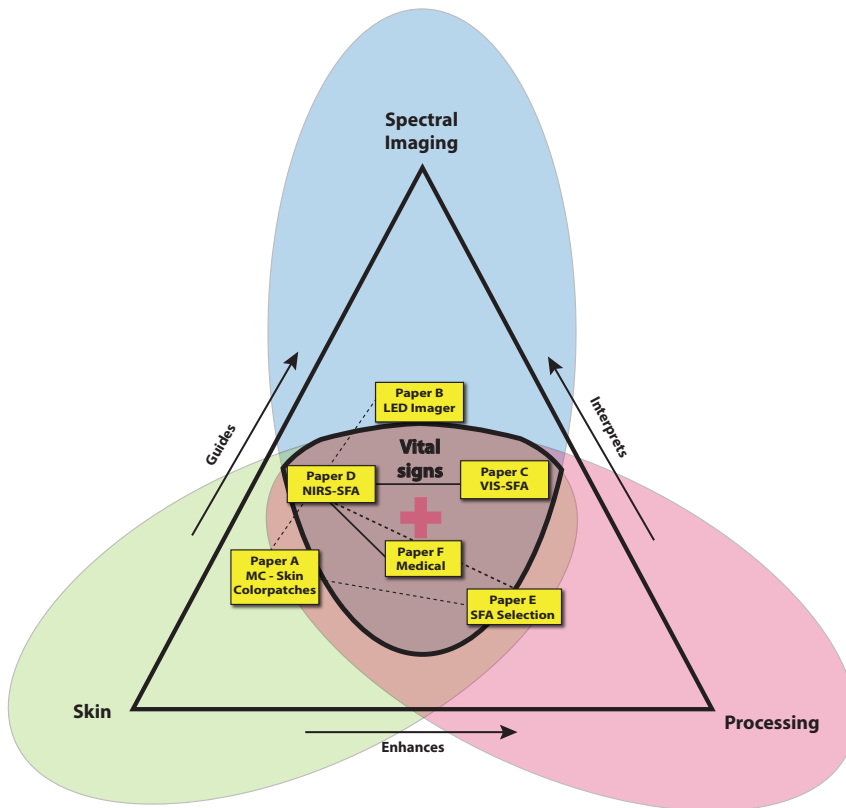


Figure 4.1: Overview of the included papers organized in to the triangular structure of skin, processing and spectral imaging. Illustrating the connections between the different publications

vironment. It focused on the impact of changes in chromophore concentration on measurable physical properties like the reflectance spectrum and colour. In **Paper B** these simulated spectra were utilized to extract physiological information from estimated spectra. It investigates if the accuracy of estimated spectra could be sufficient to quantify chromophores.

With the development of spectral filter array cameras, spectral single-shot capture in real-time is possible. Each of the bands can be acquired simultaneously and the spectral resolution is greater in comparison to RGB cameras. The estimated spectra from the multichannel RGB and LED system from **Paper B** had promising results for oxygenation level estimations, but the versatility of SFA cameras for medical applications had to be explored. SFAs are not yet a mature imaging modality and are currently prototypical. A lot of processing had to be developed

to use these imaging systems with clinical relevance. The Monte Carlo simulations were further developed and served as a way to interpret measured spectra for physiologically relevant parameters in **Paper B**, **C** and **D**. In **Paper C** a camera operating in the visual spectrum is tested as a two-dimensional spectral acquisition of parameters relevant for physicians.

The proposed framework was designed to be transferable and this was tested for an SFA camera operating in the near-infrared region of the spectrum in **Paper D**. This wavelength region is closer to the wavelengths used by the clinical standard and has the advantage of penetrating the skin deeper. Also epidermal (outer layer of the skin) melanin is more transparent in this wavelength region allowing to measure in the presence of high melanin concentrations. Another potential advantage of measuring in the near-infrared region is that it could be possible to design a light-source invisible for the human eye providing enough light to carry out measurements in the dark. It could be a way to measure oxygenation levels while a patient is sleeping.

Paper E proposes a framework, which allows to compare different SFA cameras and to tests the applicability of SFA cameras for specific applications. Monte Carlo simulations are used to create an exhaustive database of spectral reflectances and applied for training the spectral reconstruction in this paper. **Paper F** is a collaborative extension of the framework introduced with **Paper C** and demonstrates the value for physicians.

4.2 *RQ1*: How to use Monte Carlo simulation to improve the interpretation of measured skin reflectance data?

Related to *RQ1* we discuss Monte Carlo simulation in particular for interpreting measured skin reflectance data. Monte Carlo has been chosen for its long history of application to optical skin simulations and the validations it has gone through in the medical field.

In **Paper A** the concept of Monte Carlo skin simulation is introduced and recent implementations of Monte Carlo algorithms and their differences discussed in a brief **review**. The recent development in graphic processing units (GPU) and new implementations leveraging this different processing architecture lead to new Monte Carlo model implementations. Monte Carlo Modeling of Light Transport in Multilayered Tissues - MCML is a publicly available open source code written by Wang *et al.* [40].

For **Paper A**, this source code has been modified and extended to simulate reflectance spectra of skin based on changing optical properties defined as inputs for

the simulation. These simulated reflectance spectra were tested to generate **skin colour patches** with known optical properties. For each of the patches the concentration of chromophores was known. These colour patches based on Monte Carlo simulation were then generated with increasing blood level, melanin levels and bilirubin levels in their respective locations within the layered skin model. The main purpose of this experiment was to test the influence of these common chromophores on the final simulated skin colour.

This type of **visualisation** with a direct connection between the concentration of particular chromophores and colour patches can be of interest to dermatologists and anesthesiologists as educational systems. An interactive tool could provide dermatologists with a better understanding of the impact of depths, concentration, and interactions between the chromophores regarding colour. The depth of melanin, for instance, can be important information for some skin diagnoses like vitiligo and dermatosis [114], [115]. **Paper A** not only provides an overview of the available Monte Carlo simulation tools but also explores the cardinal colour axis affected by changes in the concentration of one particular chromophore as seen by the human eye.

The reflectances generated with known concentrations of chromophores are also used in **Paper B,C, and D**. These papers focus on spectral imaging with multiple bands and the controlled simulation environment allows enhancing the interpretation of spectra measured. With corresponding optical characteristics to each simulated spectral reflectance, they can be used to find close matches between estimated or measured spectral reflectances and enhance the accuracy of chromophore level estimations. Monte Carlo simulations are also the basis for generating an exhaustive training data set used to enhance spectral reconstructions in **Paper E**. A database of 10.000 skin spectra with varying concentrations of the main chromophores is used as a specialized training dataset improving the chromophore estimations from different camera models.

Paper A is missing a final and quantitative comparison of the different Monte Carlo models. Different implementations are discussed, but the simulation of colour patches is only carried out with one of the models. A comparison between the different models would be very interesting and could be extended by comparing the Monte Carlo based methods to the others including Kubelka-Munk diffusion theory approximations [12], [116]. These other approximations have the advantage that the processing times can be faster.

The comparison of colour patches based on Monte Carlo models is novel, but comparisons like these have been widely used in the computer graphics field. Within that field, the complexity of optical models is ever-increasing and physically ac-

curate models are able to generate realistic looking visualizations of the skin in many lighting situations. A quantitative comparison with these types of models could have been included. These two fields; computer graphics and medical skin modeling should be connected more and it can be considered a shortcoming of this publication and this thesis. Many structural elements of skin were also not included for the simulation of these skin patches including the wrinkles on the skin surface, more layers within the skin structure and three-dimensional complications like freckles. All patches considered homogenous skin areas.

The complex structure of skin with all its different options for optical configurations poses a challenge. Generating meaningful controlled skin spectra is an open challenge for research and validating model results a challenge of the entire community. Especially the generation of a meaningful representative skin poses a challenge. The existing skin models are also often only verified on caucasian skin.

4.3 *RQ2*: How to use SFA imaging systems for oxygenation level measurements?

Regarding *RQ2* we chose oxygenation level estimations as the particular skin imaging application. In **Paper B** a prototypical multispectral skin imaging device is investigated. The device is based on an RGB imaging sensor and multiple different coloured polarized LED illuminations. This device is used to estimate full spectral curves from the six broad spectral bands. These spectral estimations are utilized to estimate oxygenation levels in the skin. Narrow LED illumination highlight differences caused by changing chromophore concentrations. This allows using relatively broad spectral bands from an RGB camera to measure parameters like oxygenation levels.

A full spectral estimation workflow is introduced to this multi-channel system to allow analysing a full spectrum, as opposed to just a limited number of bands. These systems are usually used with ratios between different spectral bands to estimate chromophore concentrations. Spectral estimation is an alternative way to reconstruct full spectra. Previously simulated Monte Carlo simulations can then be used to solve for chromophore concentrations. In **Paper B** the chromophore concentration is based on solving an equation system with the spectral reconstructions and simulated Monte Carlo spectra to estimate chromophore concentrations. A spectral imager, which acquires all different spectral bands in the same instance has great potential for the medical sector.

Spectral filter array cameras have the potential to acquire multiple spectral bands in the same instance and provide spectral imaging in real-time. These images can have an adequate spectral resolution while maintaining a spatial 2D image of the

scene.

Oxygenation levels of skin can be a useful health metric for measuring skin flap transplantation acceptance, burn wound severity, anesthesia effectiveness, and other diagnostic applications. For these types of measurements in particular spatial differences are a subject of study. Currently, oxygenation is often measured as a point measurement and systematic parameter e.g. pulse oximeter for your fingertip. The ability to visualize spatial differences in the same time instance has clinical value. Different areas can be oxygenated differently and it can be important to monitor these differences. Efficacy of anesthesia can affect the oxygenation in particular regions for instance.

Different spectral imaging techniques have been applied to creating oxygenation or chromophore maps from skin reflectance measurements. Most of these techniques sample the spectral signal in the time domain. For instance, liquid crystal filter, filter wheel or line-scanning spectral imaging systems all have a small time delay between measuring different spectral bands or at different locations. In highly dynamic processes in human tissue, these time differences can negatively influence the measurements.

Another aspect are movements of the patient or volunteer, which can introduce artifacts to the measurement. Both of these emphasize the need for measuring in real-time and with as little as possible time delay between spectral bands and spatial locations. Three-channel systems have also been applied to the estimation of oxygen levels, but lack spectral accuracy to provide accurate and absolute measurements as shown in **Paper A**. These systems also lack the spectral versatility to be applied for multiple different spectral bands of interest.

In **Paper C** a framework is developed to establish spectral filter array cameras to estimate oxygenation levels. SFA cameras and in particular some commercially available models have unique spectral sensitivity properties that need to be accounted for. The selected filter bands were not intended for clinical and is, therefore, not optimal. The proposed framework in **Paper C** solves the spatial rearrangement, applies the spectral correction and estimates relative oxygenation levels. All methods were chosen with low computational complexity in mind. This maintains the possibility to apply the processing on a live data feed from the camera and allows the development of a **real-time** visualisation in the future.

The **validation** of the framework was performed using 58 healthy volunteers and an upper arm occlusion experiment, where a clinical standard oxygenation measurement tool was directly compared to the oxygenation levels estimated with the proposed framework. Even-though the clinical measurement tool is widely used in

the clinic it is not considered a ground-truth measurement of oxygenation. Ground truth of tissue oxygenation is difficult to measure. Chemical methods require the extraction of blood and that process might already influence the oxygenation state. The measurement with the INVOS system, a point measurement currently used in the clinic also requires a probe in direct contact with the skin tissue. This makes it impossible to measure the same location since it would be partially covering the tissue.

The clinical standard measures absolute oxygenation levels, in its current status the proposed framework only provides relative oxygenation level estimations. Absolute values could be achieved, but would require further calibration among many other improvements of the processing. These kind of calibrations would require a fixed optical setup and decrease the versatility of the setup.

The comparison between measured oxygenation levels and estimated oxygenation levels by the SFA setup was based on physiologically relevant properties of the oxygenation behavior during the upper arm occlusion test. These physiologically important parameters were chosen in dialogue with an anesthesiology department. Correlations between these parameters and operating room complications have been suggested.

Paper D illustrates the **transferability** of the proposed framework and applies it to a different camera model operating in the near-infrared (NIR) spectral region. The NIR region is of special interest for skin imaging, since melanin is increasingly transparent in that wavelength range and the light penetrates deeper into the tissue. This deeper penetration allows to sample deeper tissue levels and could potentially be used to measure more systematic oxygenation measurements. This shows the adaptability of the proposed framework to other camera models. For the experiments in **Paper D** a different and smaller set of volunteers was measured. The wavelength range of the clinical standard and this near-infrared camera are much closer and therefore the sampling depth of the signal is comparable. For this study, different light-sources were compared.

One question that is not answered in **Paper B** is if the spectral estimation increases the accuracy of the oxygenation level estimates. Comparing estimated oxygenation levels from spectral reconstructions and directly from the channel signals using the ratio-of-channels approach could have provided some insides into this question. It would also be good to quantify the impact the spectral estimation has for the linear system approach. The additional information on the general shape about the spectrum might increase the accuracy of oxygenation estimations if compared to previously simulated Monte Carlo spectra. The quantification of the results in this publication is only based on relative qualitative studies and shows potential for the

system but is not an extensive verification of the system.

Depending on the application it can be argued that there is no clinical need for introducing a relatively expensive camera to the measurement of oxygenation. It is, however, beneficial to have a spatial resolution to oxygenation level measurements, which allows studying differences in oxygenation over a large area. A direct comparison between the two cameras could have been very insightful. Comparing the different sampling depth of the two wavelengths regime and their oxygenation qualities could have been considered. All methods within the framework were chosen based on computational simplicity for future real-time applications, which was not achieved within this dissertation. The lack of absolute oxygenation levels is a limitation of the proposed framework. While the agreement between general oxygenation level shapes during the occlusion experiment was shown the correlation between the obtained parameters was moderate.

Another limitation is the use of basic oxygenation estimation methods. The methods used are based on single channels in opposition to using the full spectrum measured by the camera. A more sophisticated estimation method based on inverse Monte Carlo calculations could improve oxygenation estimations and utilize the full spectrum. Comparing the oxygenation estimation performance using the whole spectrum vs chosen single wavelengths could be studied in the future.

In conclusion, it can be argued that spectral filter array cameras hold great potential for the medical field and skin imaging in particular. The studies proposed in this research can be considered a step towards implementing this new imaging modality into the clinic. Different approaches to improve the results have been proposed and straightforward processing procedures established.

4.4 RQ3: How to select the correct spectral filter array camera and how to guide development?

RQ3 poses the question about selection criteria and guidance for future development. The development of SFA cameras and the potential for the medical sector require methods to select adequate cameras and guide their design. **Paper E** proposes a framework to select SFA cameras based on specific applications and can guide development. With limited space on the sensor and a, therefore, limited number of channels, SFA cameras need to balance a trade-off between spectral resolution and covering the entire spectrum of sensitivity. Very narrow spectral filters increase the spectral resolution but require a high number of bands to cover the full spectral range. Broader spectral filters, on the other hand, require fewer filters but decrease spectral resolution. One method to account for different spectral sensitivities is the method of spectral reconstruction which is studied in **Paper E**.

This method allows us to take the unique spectral sensitivity curves of each of the cameras into account and mathematically reconstruct full spectral measurements from a limited number of bands. For SFA cameras this can be a useful technique, especially if the spectral bands of interest for particular applications are unknown. Or if like in the case of oxygenation level estimations the spectral sensitivities are not optimal for clinical application. These spectral reconstruction methods require training reflectances and **Paper E** explores the impact of a generated specialized training set. This training set is based on Monte Carlo simulations of a wide range of different possible skin reflectances based on changing the concentrations of chromophores and evolution of the methods used in **Paper A**.

The proposed framework allows comparing SFA cameras based on publicly available databases and known spectral sensitivities of the cameras. It does not require other measurements. **Paper E** tests this framework in the context of measuring skin oxygenation levels and compares different commercially available SFA models. To further explore the impact of the trade-off between broad and narrow spectral sensitivities and to investigate the impact of ideal Gaussian spectral shapes, Gaussian versions of each SFA camera and an RGB sensor are included in the comparison. All models are compared regarding three different metrics. The first two metrics are considering the spectral reconstruction quality of each of the considered sensors. Both root mean square error (RMSE) and ΔE_{00} [117] colour differences are calculated for the reconstructed spectra using all considered sensors and test sets of reflectance measurements. The final metric is based on estimating the oxygenation level both in the test spectrum and the reconstructed spectrum and comparing the results.

Interactions between specific spectral sensitivities, training data and application-specific bands of interest need to be studied camera dependent. The design of an optimal sensor is not straightforward and all these aspects need to be considered. The framework proposed in **Paper E** allows changing the parameters and study the impact of each of them without the need for physical measurements. This allows us to optimise for specific applications and to study spectral filter array configurations in a theoretical environment.

For **Paper E** oxygenation level estimation was the application for comparison. Different techniques have been proposed to estimate oxygenation levels based on the spectral reflectance of skin tissue. Some of these methods are single-channel methods, based on differences in the absorption characteristics of different chromophores. Other techniques are based on the entire spectral reflectance spectrum of skin. This makes oxygenation level estimation a good application to test the capability of spectral filter array cameras. Estimating full spectral reflectance from the limited number of bands makes it possible to use full spectral based estimation

techniques.

The performance of the spectral estimations is affected by the choice of **training reflectances** used for the spectral reconstruction. In **Paper E** a training dataset is proposed that is based on simulated skin spectra. The simulations are based on Monte Carlo simulations with different chromophore concentrations. This specialized reflectance spectrum increased the reconstruction of spectral reflectances and can be used for generating a controlled dataset for data-driven training algorithms. To check the validity of the proposed simulated dataset, a principal component analysis is included in **Paper E**.

Paper E does not include measurements on patients. These are necessary to verify the usability of any particular SFA camera in a medical context. It does, however, propose a novel way to compare and optimize SFA's without the need of additional extensive measurements.

Not considering noise is a simplification present in the current implementation of the framework. SFA cameras, in particular, are prone to noise due to the trade-off between spectral sensitivity and covering the spectral range. The framework is implemented in a way that noise could be considered in the future.

The framework provides the non existing means to test any creation of spectral filter array sensors. Testing an SFA sensor with spectral sensitivity peaks overlapping with the different hemoglobin absorption peaks could have been considered. Comparing this specialized oxygenation SFA camera with other cameras would have been a good and possible addition. Another approach is to optimize the spectral reconstruction to estimate only the exact bands of interest. The effect of the full spectral reconstruction should be further quantified regarding oxygenation level estimations. This is particularly interesting for more complex methods of estimating the oxygenation levels. In this implementation, only a channel approach utilizing only three or six bands were studied. A quantitative comparison between applying the spectral reconstruction and using a more complex oxygenation level estimation could be included.

It could also be interesting to compare the performance of oxygenation level estimations at the hemoglobin absorption peaks vs the sensitivity peaks of each of the cameras. The implemented Gaussian sensor creation allows to even formulate an optimization to find the optimal spectral sensitivities for oxygenation estimation.

The outcome: it can be concluded that the framework provides a novel previously non existing way to study SFA cameras and find optimal filter sensitivities for a given applications. The complex interaction of broad vs narrow filters, number of bands vs bands of interest can be optimized with this proposed framework.

Generated specialised skin reflectances, as a dataset for reconstructing spectra is also studied and shows reconstruction improvements.

4.5 *RQ4*: Can SFA cameras actually be used in the clinic?

RQ4 raises the question about how useful SFA cameras are in a clinical setup. **Paper F** is a collaborative work with the anesthesiology department of Vrije Universiteit amsterdam medical center that starts to address this question. The methods of estimating the oxygenation levels are described in detail in **Paper C** and the data analyzed for these two papers are identical.

Clinically it has recently been shown that recovery behavior from the upper arm occlusion experiments can be indicators for complications in the operating room. This Paper focuses on interpreting the obtained oxygenation curves regarding these parameters. As opposed to **Paper C** additional clinically relevant parameters are obtained from the oxygenation curves. At the same time, these parameters are obtained from a clinically accepted and standard oxygenation level measurement device and both are compared.

The correlation is too low to suggest an immediate application in the clinic. For the operating room, absolute oxygenation values would be more beneficial and future development should aim for estimating absolute oxygenation levels. The paper also discusses several other reasons for the low correlations including the difference in sampling depth, normalisation procedures in the data analysis and measurement frequency differences.

During the processing of the data, normalization was applied to the absolute oxygenation level results from the clinical standard and the estimations from SFA. It can be argued that this normalization affects the results positively with regards to the comparability of the two curves. But this normalization also emphasizes small differences in the sampling frequency. A small offset of a peak of the resaturation effects the slope drastically. This raises the question if the slope is the best parameter for comparison. The process of normalisation is, however, necessary since the two systems measure on different scales. All volunteer data including outliers was included and provides a good estimate about the accuracy obtained with the proposed setup.

In summary: the results obtained clearly show the relative changes, but the comparison with the INVOS system needs to be reconsidered. It has been shown that SFA cameras provide a unique and interesting tool to study oxygenation spatially resolved. The acquisition speed can also be beneficial for physicians and the potential for further development is great.

4.6 Summary of the main limitations

For each of the posed research questions significant progress has been made in this dissertations and through the publications. This section provides a brief summary of the main limitations considering each of the different research questions. Regarding *RQ1* the main limitation is a missing quantitative comparison with different types of models. These include both different models published in the computer graphics domain as well as models published in the biomedical optics domain.

The main limitation for *RQ2* is the missing ground truth of tissue oxygenation data. Furthermore, the final evaluation framework (from paper **Paper E**) for SFA cameras does not include real world measurements on volunteers and using real cameras. For a final evaluation and verification for the applicability in the medical domain this is mandatory.

The main omission regarding *RQ3* is the lack of a final optimization of the proposed framework. In order to recommend and design an optimal camera for skin oxygenation measurements the framework would have to be optimized with considering parameters such as sensor sensitivity, number of bands and training data as free parameters and provide an optimal camera as a result.

The biggest limitation regarding *RQ3* is the low correlation, which does not suggest an immediate application in the clinic. Many strategies, in order, to improve these correlations including: more complex oxygenation estimations methods, different accuracy metrics and differences in sampling depth have been proposed to overcome this limitation.

Chapter 5

Conclusion and perspectives

5.1 Conclusion

In this dissertation, we aimed to advance and validate the potential of spectral filter array cameras for medical diagnosis and skin imaging. Spectral imaging allows us to acquire scenes with more than three colour channels and to measure physiological changes visible in specific (narrow) bands in the spectrum. Spectral filter array cameras are a novel spectral imaging modality with great potential for the medical field. SFA imaging allows acquiring spectral images with no time-delay between different bands and in real-time. The unique hardware requires specialized processing of the available bands.

This research proposes a framework to process the data from this special type of SFA camera. Interpreting the acquired spectral information for medically relevant parameters can be enhanced by simulations of the optical interactions of skin. Monte Carlo methods have been used to improve the interpretation of measured skin reflectances and to reconstruct reflectances accurately.

The proposed framework is tested in the context of oxygenation level estimations of volunteers and compared to a clinical standard measurement. Oxygenation level of skin is a relevant clinical parameter and benefits from spatial acquisition. The proposed framework is applied to three different imaging systems covering the visual and near-infrared spectrum of light.

Finally, another framework is proposed to help to select and develop suitable SFAs for skin imaging and oxygenation level estimation. This framework is used to compare commercially available SFA cameras and study the influence of computer-generated training data based on Monte Carlo skin simulations. It does not require

additional measurements and is only based on publicly available databases.

This dissertation develops the applicability of SFA cameras further and establishes basic processing pipelines to use this novel technology in the medical field. Adequate agreement for a proof of concept study has been found between the clinical golden standard oxygenation device and different spectral cameras. SFA imaging improved the accuracy of oxygenation level estimations and produced good agreement of oxygenation progression curves during an upper arm occlusion experiment. A clinical study of the proposed technique showed a moderate correlation between oxygenation level estimations and oxygenation level measurements in a clinical context. An abstract computer-based framework has been used to compare commercially available SFA models for oxygenation estimation. The positive impact of a generated specialized skin reflectance database for reflectance reconstructions has been shown.

SFA cameras are currently not optimally designed for medical applications with the filter selection as shown in this thesis. However, using the suggested framework, depending on the application, the optimal filter selection can be selected for newly developed SFA cameras. Design recommendations can be inferred from the proposed framework and it can aid the development of future application-specific SFA imaging systems in the medical and other fields.

5.2 Perspectives

The proposed framework for oxygenation level estimation is designed with low computational complexity in mind and based on straightforward methods. At the current implementation, the method does not provide absolute oxygenation levels. With further calibration and more sophisticated methods, absolute oxygenation levels could be obtained. Data-driven learning algorithms could be trained with the proposed and simulated skin reflectance database and improve estimations from measured data. Optimization techniques could be also applied to the comparison framework to generate an optimal sensor for predefined constraints.

The demand for the development of imaging sensor technology of the last decade is likely to continue. This demand is driven by the innovation pressure within the consumer market for miniature sensors in the smartphone industry as one example. It might lead to wider adoption of multi-channel spectral filter array-based systems. Already now many sensor manufacturers offer the small scale production of sensors with custom sensitivity bands specialized for particular applications.

In the scenario, that sensor innovation and miniaturization continue, the costs of SFA cameras will decrease drastically. The need for tools to guide and optimize the spectral filters will increase and in turn, increase the relevance of this work.

Specialized systems for particular applications are already a reality and the demand for these custom imaging sensors is likely to increase. In case these sensors find commercial success in one of possible applications it could decrease the prices drastically. With drastically reduced prices the range of applications increases further and wider adoption of customized sensors becomes more likely.

Bibliography

- [1] Ximea. *Hyperspectral Cameras*. <https://www.ximea.com>. [accessed 02. december 2018]. Dec. 2018.
- [2] SILIOS. *Multispectral-Imaging*. <https://www.silios.com>. [accessed 02. december 2018]. Dec. 2018.
- [3] B. S. Gerstman. *Biological and Medical Physics, Biomedical Engineering*. Berlin, Germany: Springer.
- [4] G. J. Tortora and B. H. Derrickson. *Principles of anatomy and physiology*. John Wiley & Sons, 2008.
- [5] J. R. Bauer, J.-B. Thomas, J. Y. Hardeberg and R. M. Verdaasdonk. “An Evaluation Framework for Spectral Filter Array Cameras to Optimize Skin Diagnosis”. In: *Sensors* 19.21 (2019). ISSN: 1424-8220. DOI: [10.3390/s19214805](https://doi.org/10.3390/s19214805).
- [6] L. Fodor, M. Elman and Y. Ullmann. *Aesthetic applications of intense pulsed light*. Berlin, Germany: Springer Science & Business Media, 2010.
- [7] M. J. C. van Gemert, S. L. Jacques, H. J. C. M. Sterenborg and W. M. Star. “Skin optics”. In: *IEEE Transactions on Biomedical Engineering* 36.12 (1989), pp. 1146–1154.
- [8] M. Ferguson-Pell and S. Hagsisawa. “An empirical technique to compensate for melanin when monitoring skin microcirculation using reflectance spectrophotometry”. In: *Medical Engineering & Physics* 17.2 (1995), pp. 104–110.
- [9] A. K. Jain and S. Z. Li. *Encyclopedia of Biometrics*. Vol. 1. Springer Science & Business Media, 2009. ISBN: 978-0-387-73002-8.

- [10] W. F. Lever. *Histopathology of the Skin*. Ed. by D. E. Elder. 10th. Alphen aan den Rijn, The Netherlands: Wolters Kluwer N.V., 1949.
- [11] E. Claridge, S. Cotton, P. Hall and M. Moncrieff. “From colour to tissue histology: physics-based interpretation of images of pigmented skin lesions”. In: *Medical Image Analysis 7.4* (2003), pp. 489–502.
- [12] R. R. Anderson and J. A. Parrish. “The optics of human skin”. In: *Journal of Investigative Dermatology 77.1* (1981), pp. 13–19.
- [13] G. V. G. Baranoski and T. F. Chen. “Optical Properties of Skin Surface”. In: *Measuring the Skin*. Ed. by P. Humbert, H. Maibach, F. Fanian and P. Agache. Berlin, Germany: Springer International Publishing, 2016, pp. 1–14. ISBN: 978-3-319-26594-0.
- [14] T. Lister, P. A. Wright and P. H. Chappell. “Optical properties of human skin”. In: *Journal of Biomedical Optics 17.9* (2012), pp. 1 - 15 –15.
- [15] L. L. Randeberg. “Diagnostic applications of diffuse reflectance spectroscopy”. PhD thesis. Norwegian University of Science and Technology, 2005, pp. 315–403. ISBN: 82-471-7077-9.
- [16] S. L. Jacques and S. A. Prahl. *A collaboration of Oregon Health & Science University, Portland State University, and the Oregon Institute of Technology. Optical Spectra*. <https://omlc.org/spectra/>. [accessed 02. december 2018].
- [17] L. Kocsis, P. Herman and A. Eke. “The modified Beer–Lambert law revisited”. In: *Physics in Medicine & Biology 51.5* (2006), N91.
- [18] K. P. Nielsen, L. Zhao, J. J. Stamnes, K. Stamnes and J. Moan. “The optics of human skin: Aspects important for human health”. In: *Solar Radiation and Human Health, Norwegian Academy of Science and Letters, Oslo* (2008), pp. 34–46.
- [19] B. Kusse Sukuta. “Spectral imaging and analysis of human skin”. MA thesis. University of Estern Finland, 2010.
- [20] B. S. Sorg, B. J. Moeller, O. Donovan, Y. Cao and M. W. Dewhirst. “Hyperspectral imaging of hemoglobin saturation in tumor microvasculature and tumor hypoxia development”. In: *Journal of Biomedical Optics 10.4* (2005), pp. 044004–044011.
- [21] C. C. Cooksey, D. W. Allen and B. K. Tsai. “Reference Data Set of Human Skin Reflectance”. In: *Journal of Research of the National Institute of Standards and Technology 122* (2017), pp. 1–5.
- [22] T. B. Fitzpatrick. “The validity and practicality of sun-reactive skin types: I through VI”. In: *Archives of Dermatology 124.6* (1988), pp. 869–871.

-
- [23] L. L. Randeberg, A. Winnem, S. Blindheim, O. Haugen and L. Svaasand. “Optical classification of bruises”. In: *Proc.SPIE Lasers in Surgery* (San Jose, CA, United States). Vol. 5312. July 2004, pp. 54–64.
- [24] J. A. Delgado Atencio, S. L. Jacques and S. V. Montiel. *Monte Carlo Modeling of Light Propagation in Neonatal Skin*. InTech, Feb. 2011. ISBN: 978-953-307-427-6.
- [25] I. S. Saidi, S. L. Jacques and F. K. Tittel. “Mie and Rayleigh modeling of visible-light scattering in neonatal skin.” In: *Applied Optics* 34.31 (Nov. 1995), pp. 7410–7418.
- [26] P. Kubelka and F. Munk. “An article on optics of paint layers”. In: *Z. Tech. Phys* 12.593-601 (1931).
- [27] T. Spott and L. O. Svaasand. “Collimated light sources in the diffusion approximation”. In: *Applied Optics* 39.34 (2000), pp. 6453–6465.
- [28] L. L. Randeberg, E. L. P. Larsen and L. O. Svaasand. “Hyperspectral imaging of blood perfusion and chromophore distribution in skin”. In: *Proc.SPIE Photonic Therapeutics and Diagnostics V* (San Jose, CA, United States). Vol. 7161. Feb. 2009, p. 12.
- [29] H. Nakai, Y. Manabe and S. Inokuchi. “Simulation and analysis of spectral distributions of human skin”. In: *Pattern Recognition, 1998. Proceedings. Fourteenth International Conference on Pattern Recognition (CVPR)*. IEEE, 1998, 1065–1067 vol.2. ISBN: 0-8186-8512-3.
- [30] A. Krishnaswamy and G. V. Baranoski. “A Biophysically-Based Spectral Model of Light Interaction with Human Skin”. In: *Computer Graphics Forum* 23.3 (2004), pp. 331–340. DOI: [10.1111/j.1467-8659.2004.00764.x](https://doi.org/10.1111/j.1467-8659.2004.00764.x).
- [31] C. Donner, T. Weyrich, E. d’Eon, R. Ramamoorthi and S. Rusinkiewicz. “A Layered, Heterogeneous Reflectance Model for Acquiring And Rendering Human Skin”. In: *ACM Trans. on Graphics (Proc. SIGGRAPH Asia 2008)* 27.5 (2008), 10:1–10:12. DOI: [10.1145/1457515.1409093](https://doi.org/10.1145/1457515.1409093).
- [32] J. Jimenez, T. Scully, N. Barbosa, C. Donner, X. Alvarez, T. Vieira, P. Matts, V. Orvalho, D. Gutierrez and T. Weyrich. “A practical appearance model for dynamic facial color”. In: *ACM Transactions on Graphics (Proc. SIGGRAPH Asia)* 29.6 (2010), 141:1–141:10.
- [33] E. Angelopoulo, R. Molana and K. Daniilidis. “Multispectral skin color modeling”. In: *Proceedings of the 2001 IEEE Computer Society Conference on Computer Vision and Pattern Recognition. CVPR 2001*. Vol. 2. Dec. 2001, pp. II–II.

- [34] T. F. Chen, G. V. G. Baranoski, B. W. Kimmel and E. Miranda. “Hyper-spectral Modeling of Skin Appearance”. In: *ACM Trans. Graph.* 34.3 (May 2015), 31:1–31:14. ISSN: 0730-0301. DOI: [10.1145/2701416](https://doi.org/10.1145/2701416).
- [35] C. Donner and H. W. Jensen. “A spectral BSSRDF for shading human skin”. In: *EGSR '06: Proceedings of the 17th Eurographics conference on Rendering Techniques*. University of California, San Diego. Eurographics Association, June 2006.
- [36] C. S. Donner. “Towards Realistic Image Synthesis of Scattering Materials”. PhD thesis. University of California at San Diego, Jan. 2006.
- [37] E. Alerstam, T. Svensson and S. Andersson-Engels. “Parallel computing with graphics processing units for high-speed Monte Carlo simulation of photon migration”. In: *Journal of Biomedical Optics* 13.6 (2008), pp. 1–3. DOI: [10.1117/1.3041496](https://doi.org/10.1117/1.3041496).
- [38] Q. Fang and D. A. Boas. “Monte Carlo Simulation of Photon Migration in 3D Turbid Media Accelerated by Graphics Processing Units”. In: *Optics Express* 17.22 (2009), pp. 20178–20190.
- [39] L. H. Wang, S. L. Jacques and L. Q. Zheng. “MCML - Monte-Carlo Modeling of Light Transport in Multilayered Tissues”. In: *Computer Methods and Programs in Biomedicine* 47.2 (July 1995), pp. 131–146.
- [40] S. L. Jacques and L. Wang. “Monte Carlo Modeling of Light Transport in Tissues”. In: *Optical-Thermal Response of Laser-Irradiated Tissue*. Boston, MA: Springer US, 1995, pp. 73–100. ISBN: 978-1-4757-6094-1.
- [41] Y. Liu, S. L. Jacques, M. Azimipour, J. D. Rogers, R. Pashaie and K. W. Eliceiri. “OptogenSIM: a 3D Monte Carlo simulation platform for light delivery design in optogenetics”. In: *Biomedical Optics Express* 6.12 (2015), pp. 4859–12.
- [42] S. L. Jacques. “Coupling 3D Monte Carlo light transport in optically heterogeneous tissues to photoacoustic signal generation”. In: *Biochemical Pharmacology* 2.4 (Dec. 2014), pp. 137–142.
- [43] D. Gareau, S. Jacques and J. Krueger. “Monte Carlo modeling of pigmented lesions”. In: *Proc. SPIE Photonic Therapeutics and Diagnostics X*. SPIE, Mar. 2014, pp. 89260V–7.
- [44] M. Milanič. “Three-dimensional Monte Carlo model of pulsed-laser treatment of cutaneous vascular lesions”. In: 16.12 (Dec. 2011), pp. 128002–128013.

- [45] P. Naglič, L. Vidovič, M. Milanič, L. L. Randeberg and B. Majaron. “Combining the diffusion approximation and Monte Carlo modeling in analysis of diffuse reflectance spectra from human skin”. In: *Proc. SPIE Photonic Therapeutics and Diagnostics X*. Vol. 8926. Mar. 2014, p. 13.
- [46] V. C. Paquit, F. Mériaudeau, J. R. Price and K. W. Tobin. “Simulation of skin reflectance images using 3D tissue modeling and multispectral Monte Carlo light propagation.” In: *Conference proceedings : IEEE Engineering in Medicine and Biology Society*. 2008 (2008), pp. 447–450. ISSN: 1094-687X.
- [47] L. L. Randeberg, I. Baarstad, T. Løke, P. Kaspersen and L. O. Svaasand. “Hyperspectral imaging of bruised skin”. In: *Proc. SPIE Photonic Therapeutics and Diagnostics II*. Vol. 6078. SPIE, Feb. 2006.
- [48] S. L. Jacques. “Quick analysis of optical spectra to quantify epidermal melanin and papillary dermal blood content of skin”. In: *Journal of Biophotonics* 8.4 (Dec. 2014), pp. 309–316.
- [49] S. Yamamoto, I. Fujiwara, M. Yamauchi, N. Tsumura and K. Ogawa-Ochiai. “Optical path-length matrix method for estimating skin spectrum”. In: *Optical Review* 19.6 (2012), pp. 361–365.
- [50] J. Y. Hardeberg. “Acquisition and Reproduction of Color Images: Colorimetric and Multispectral Approaches.” PhD Thesis. Paris, France: Ecole Nationale Supérieure des Télécommunications, 1999.
- [51] P.-J. Lapray, X. Wang, J.-B. Thomas and P. Gouton. “Multispectral filter arrays: recent advances and practical implementation.” In: *Sensors* 14.11 (2014), pp. 21626–21659.
- [52] N. A. Hagen and M. W. Kudenov. “Review of snapshot spectral imaging technologies”. In: *Optical Engineering* 52 (2013), pp. 52 - 52 –23.
- [53] W. Liang, M. Bockrath, D. Bozovic, J. H. Hafner, M. Tinkham and H. Park. “Fabry-Perot interference in a nanotube electron waveguide”. In: *Nature* 411.6838 (2001), p. 665.
- [54] S. Chen and Q. Liu. “Modified Wiener estimation of diffuse reflectance spectra from RGB values by the synthesis of new colors for tissue measurements”. In: 17.3 (2012), p. 030501.
- [55] I. Nishidate, T. Maeda, K. Niizeki and Y. Aizu. “Estimation of Melanin and Hemoglobin Using Spectral Reflectance Images Reconstructed from a Digital RGB Image by the Wiener Estimation Method”. In: *Sensors* 13.6 (June 2013), pp. 7902–7915.

- [56] N. Shimano and M. Hironaga. “Recovery of spectral reflectances of imaged objects by the use of features of spectral reflectances”. In: *J. Opt. Soc. Am. A* 27.2 (Feb. 2010), pp. 251–258.
- [57] P. Stigell, K. Miyata and M. Hauta-Kasari. “Wiener estimation method in estimating of spectral reflectance from RGB images”. In: *Pattern Recognition and Image Analysis* 17.2 (June 2007), pp. 233–242.
- [58] J.-H. Yoo, W.-J. Kyung, H.-G. Ha and Y.-H. Ha. “Estimation of reflectance based on properties of selective spectrum with adaptive Wiener estimation”. In: *IS&T/SPIE Electronic Imaging*. Ed. by R. Eschbach, G. G. Marcu and A. Rizzi. SPIE, Feb. 2013, p. 86520D.
- [59] F. H. Imai and R. S. Berns. “Spectral estimation using trichromatic digital cameras”. In: *Proceedings of the International Symposium on Multispectral Imaging and Color Reproduction for Digital Archives*. Vol. 42. Chiba University Chiba, Japan. 1999, pp. 1–8.
- [60] N. Shimano, K. Terai and M. Hironaga. “Recovery of spectral reflectances of objects being imaged by multispectral cameras”. In: *Journal of the Optical Society of America A* 24.10 (2007), p. 3211.
- [61] V. Heikkinen, R. Lenz, T. Jetsu, J. Parkkinen, M. Hauta-Kasari and T. Jääskeläinen. “Evaluation and unification of some methods for estimating reflectance spectra from RGB images”. In: *J. Opt. Soc. Am. A* 25.10 (Oct. 2008), pp. 2444–2458. DOI: [10.1364/JOSAA.25.002444](https://doi.org/10.1364/JOSAA.25.002444).
- [62] S. L. Jacques. “Optical properties of biological tissues: a review”. In: *Physics in Medicine and Biology* 58.11 (2013), R37.
- [63] D. Cuccia. “Quantitative, Wide-field Characterization of Tissue Optical Properties and Chromophores with Spatial Frequency Domain Imaging (SFDI)”. In: *CLEO: Applications and Technology*. Washington, D.C.: OSA, 2011. ISBN: 978-1-55752-910-7.
- [64] B. D’Alessandro and A. P. Dhawan. “Transillumination imaging for blood oxygen saturation estimation of skin lesions.” In: *IEEE transactions on bio-medical engineering* 59.9 (Sept. 2012), pp. 2660–2667.
- [65] R. M. P. Doornbos, R. Lang, M. C. Aalders, F. W. Cross and H. J. C. M. Sterenborg. “The determination of in vivo human tissue optical properties and absolute chromophore concentrations using spatially resolved steady-state diffuse reflectance spectroscopy”. In: *Physics in Medicine and Biology* 44.4 (Jan. 1999), pp. 967–981.
- [66] M. Ehler. “Principal component model of multispectral data for near real-time skin chromophore mapping”. In: 15.4 (Aug. 2010), p. 046007.

- [67] I. V. Kumpanenko, A. V. Roshchin, N. A. Ivanova, A. V. Bloshenko, N. A. Shalynina and T. N. Korneeva. “Colorimetry: Choice of colorimetric parameters for chromophore concentration measurements”. In: *Russian Journal of General Chemistry* 84.11 (Dec. 2014), pp. 2295–2304.
- [68] I. Kuzmina, M. Lacis, J. Spigulis, A. Berzina and L. Valeine. “Study of smartphone suitability for mapping of skin chromophores”. In: *Journal of Biomedical Optics* 20.9 (Sept. 2015), pp. 090503–090505.
- [69] Z. Liu. “Skin image illumination modeling and chromophore identification for melanoma diagnosis”. In: (May 2016), pp. 1–16.
- [70] N. MacKinnon, F. Vasefi, E. Gussakovsky, G. Bearman, R. Chave and D. L. Farkas. “In vivo skin chromophore mapping using a multimode imaging dermoscope (SkinSpec)”. In: *SPIE BiOS* 8587 (Feb. 2013), p. 13.
- [71] I. V. Meglinski and S. J. Matcher. “Computer simulation of the skin reflectance spectra.” In: *Computer Methods and Programs in Biomedicine* 70.2 (Feb. 2003), pp. 179–186.
- [72] I. Nishidate, K. Sasaoka, T. Yuasa, K. Niizeki, T. Maeda and Y. Aizu. “Visualizing of skin chromophore concentrations by use of RGB images”. In: *Optics Letters* 33.19 (2008), p. 2263.
- [73] J. Spigulis, I. Oshina, A. Berzina and A. Bykov. “Smartphone snapshot mapping of skin chromophores under triple-wavelength laser illumination”. In: *Journal of Biomedical Optics* 22(9).091508 (2017).
- [74] P. Välisuo, I. Kaartinen, V. Tuchin and J. Alander. “New closed-form approximation for skin chromophore mapping”. In: *Journal of Biomedical Optics* 16.4 (2011), pp. 046012–046012–10.
- [75] I. Fredriksson. “Inverse Monte Carlo method in a multilayered tissue model for diffuse reflectance spectroscopy”. In: *Journal of Biomedical Optics* 17.4 (Apr. 2012), pp. 047004–13.
- [76] R. Jolivot, Y. Benezeth and F. Marzani. “Skin Parameter Map Retrieval from a Dedicated Multispectral Imaging System Applied to Dermatology / Cosmetology”. In: *International Journal of Biomedical Imaging* 2013.3 (2013), pp. 1–15.
- [77] N. Tsumura, M. Kawabuchi, H. Haneishi and Y. Miyake. “Mapping Pigmentation in Human Skin by Multi-Visible-Spectral Imaging by Inverse Optical Scattering Technique.” In: *Color Imaging Conference* (2000), pp. 81–84.

- [78] D. Jakovels, U. Rubins and J. Spigulis. “RGB imaging system for mapping and monitoring of hemoglobin distribution in skin”. In: *SPIE Optical Engineering+ Applications*. Ed. by S. S. Shen and P. E. Lewis. International Society for Optics and Photonics. International Society for Optics and Photonics, Sept. 2011, 81580R–81580R–6.
- [79] J. Spigulis, D. Jakovels and U. Rubins. “Multi-spectral skin imaging by a consumer photo-camera”. In: *Proc. SPIE Multimodal Biomedical Imaging V* (San Francisco, CA, United States). Vol. 7557. SPIE, Feb. 2010, p. 9.
- [80] J. Spigulis, U. Rubins, E. Kviesis-Kipge and O. Rubenis. “SkImager: a concept device for in-vivoskin assessment by multimodal imaging”. In: *Proceedings of the Estonian Academy of Sciences* 63.3 (2014), pp. 301–308.
- [81] D. Nakao, N. Tsumura and Y. Miyake. “Realtime multispectral image processing for mapping pigmentation in human skin”. In: *in Proc. Ninth IS&T/SID Color Imaging Conference, IS&T*. Scottsdale, AZ, USA. IS&T, Nov. 1995, pp. 80–84.
- [82] A. Rajabi-Estarabadi, J. M. Bittar, C. Zheng, V. Nascimento, I. Camacho, L. G. Feun, M. Nasiriavanaki, M. Kunz and K. Nouri. “Optical coherence tomography imaging of melanoma skin cancer”. In: *Lasers in Medical Science* 34.2 (Mar. 2019), pp. 411–420. ISSN: 1435-604X. DOI: [10.1007/s10103-018-2696-1](https://doi.org/10.1007/s10103-018-2696-1).
- [83] L. Themstrup and G. Jemec. “Chapter 6 - Optical Coherence Tomography for Skin Cancer and Actinic Keratosis”. In: *Imaging in Dermatology*. Ed. by M. R. Hamblin, P. Avci and G. K. Gupta. Boston, USA: Academic Press, 2016, pp. 59–67. ISBN: 978-0-12-802838-4. DOI: [10.1016/B978-0-12-802838-4.00006-6](https://doi.org/10.1016/B978-0-12-802838-4.00006-6).
- [84] X. Attendu, M. H. Bourget, M. P. de Sivry-Houle and C. Boudoux. “Coregistered optical coherence tomography and frequency-encoded multispectral imaging for spectrally sparse color imaging”. In: *Journal of Biomedical Optics* 25.3 (2019), pp. 1–12. DOI: [10.1117/1.JBO.25.3.032008](https://doi.org/10.1117/1.JBO.25.3.032008).
- [85] V. Ahlgrimm-Siess, M. Laimer, H. S. Rabinovitz, M. Oliviero, R. Hofmann-Wellenhof, A. A. Marghoob and A. Scope. “Confocal Microscopy in Skin Cancer”. In: *Current dermatology reports* 7.2 (2018), pp. 105–118. DOI: [10.1007/s13671-018-0218-9](https://doi.org/10.1007/s13671-018-0218-9).
- [86] G. Salerni, C. Carrera, L. Lovatto, R. M. Martí-Laborda, G. Isern, J. Palou, L. Alós, S. Puig and J. Malvehy. “Characterization of 1152 lesions excised over 10 years using total-body photography and digital dermatoscopy in the surveillance of patients at high risk for melanoma”. In: *Journal of the*

- American Academy of Dermatology* 67.5 (2012), pp. 836–845. ISSN: 0190-9622. DOI: [10.1016/j.jaad.2012.01.028](https://doi.org/10.1016/j.jaad.2012.01.028).
- [87] G. Zonios, J. Bykowski and N. Kollias. “Skin melanin, hemoglobin, and light scattering properties can be quantitatively assessed in vivo using diffuse reflectance spectroscopy.” In: *The Journal of investigative dermatology* 117.6 (Dec. 2001), pp. 1452–1457.
- [88] B. J. Tromberg. “Biophotonics and the Future of Personal Health Care”. In: *Frontiers in Optics*. Washington, D.C.: OSA, 2015, FM4A.3. ISBN: 978-1-943580-03-3.
- [89] Q. Li, X. He, Y. Wang, H. Liu, D. Xu and F. Guo. “Review of spectral imaging technology in biomedical engineering: achievements and challenges”. In: *Journal of Biomedical Optics* 18.10 (Oct. 2013), p. 100901.
- [90] I. Diebele, I. Kuzmina, A. Lihachev, J. Kapostinsh, A. Derjabo, L. Valeine and J. Spigulis. “Clinical evaluation of melanomas and common nevi by spectral imaging.” In: *Biomedical Optics Express* 3.3 (Mar. 2012), pp. 467–472.
- [91] A. Kumar, A. P. Dhawan, P. Relue and P. K. Chaudhuri. “Multi-spectral optical imaging of skin to diagnose malignant melanoma”. In: *Conf Proc: Engineering in Medicine and Biology, 1999*. IEEE, 1999, 1098 vol.2. ISBN: 0-7803-5674-8.
- [92] I. Kuzmina, I. Diebele, D. Jakovels, J. Spigulis, L. Valeine, J. Kapostinsh and A. Berzina. “Towards noncontact skin melanoma selection by multispectral imaging analysis”. In: *Journal of Biomedical Optics* 16.6 (2011), pp. 060502–060502–3.
- [93] R. de Roode, H. J. Noordmans, A. Rem, S. Couwenberg and R. Verdaasdonk. “Evaluation of laser treatment response of vascular skin disorders in relation to skin properties using multi-spectral imaging”. In: *Proc.SPIE Photonic Therapeutics and Diagnostics IV*. Vol. 6842. 68420B. Feb. 2008, p. 9.
- [94] “Calibration and segmentation of skin areas in hyperspectral imaging for the needs of dermatology”. In: (Sept. 2014), pp. 1–19.
- [95] C. Balas, G. Themelis, A. Papadakis and E. Vasgiouraki. “A novel hyperspectral imaging system: application on in-vivo detection and grading of cervical precancers and of pigmented skin lesions”. In: 2001.
- [96] M. Milanič, A. Bjorgan, M. Larsson, P. Marraccini, T. Strömberg and L. L. Randeberg. “Hyperspectral imaging for detection of cholesterol in human skin”. In: *SPIE BiOS* 9332 (Mar. 2015), p. 12.

- [97] S. V. Patwardhan. “Multi-spectral light interaction modeling and imaging of skin lesions”. PhD thesis. New Jersey Institute of Technology, Oct. 2003, pp. 1–124.
- [98] E. R. Anderson, J. S. You, D. J. Cuccia, B. J. Tromberg and A. J. Durkin. “Spatial-Frequency-Domain Imaging for quality assessment of apples”. In: *2006 Conference on Lasers and Electro-Optics and 2006 Quantum Electronics and Laser Science Conference*. IEEE, 2006, pp. 1–2. ISBN: 978-1-55752-813-1.
- [99] D. J. Cuccia. “Validation and Clinical Deployment of a Spatial Frequency Domain Imaging (SFDI) System for Wide-field, Quantitative Subsurface Analysis of Tissue Health”. In: *Imaging and Applied Optics Technical Papers*. 2012.
- [100] D. J. Cuccia. “Spatial Frequency Domain Imaging (SFDI): a technology overview and validation of an LED-based clinic-friendly device”. In: *Emerging Digital Micromirror Device Based Systems and Applications IV*. Ed. by M. R. Douglass and P. I. Oden. 2012.
- [101] D. Cuccia. “Design and Validation of a Spatial Frequency Domain Imaging (SFDI) System for Biomedical Research Applications”. In: *Frontiers in Optics*. Washington, D.C.: OSA, 2015, FM2C.1. ISBN: 978-1-943580-03-3.
- [102] D. Cuccia. “Validation of Spatial Frequency Domain Imaging (SFDI) for Biomedical Research Applications”. In: *Applied Industrial Optics: Spectroscopy, Imaging and Metrology*. Washington, D.C.: OSA, 2015, AIT2C.2. ISBN: 978-1-943580-00-2.
- [103] M. Ghijssen, A. J. Durkin, S. Gioux and B. J. Tromberg. “Real-time simultaneous single snapshot of optical properties and blood flow using coherent spatial frequency domain imaging (cSFDI)”. In: *Biomedical Optics Express* 7.3 (2016), pp. 870–813.
- [104] J. Pichette, A. Laurence, L. Angulo, F. Lesage, A. Bouthillier, D. K. Nguyen and F. Leblond. “Intraoperative video-rate hemodynamic response assessment in human cortex using snapshot hyperspectral optical imaging”. In: *Neurophotonics* 3.4 (2016), pp. 1–9. DOI: [10.1117/1.NPh.3.4.045003](https://doi.org/10.1117/1.NPh.3.4.045003).
- [105] R. B. Saager, M. L. Baldado, R. A. Rowland, K. M. Kelly and A. J. Durkin. “Method using in vivo quantitative spectroscopy to guide design and optimization of low-cost, compact clinical imaging devices: emulation and evaluation of multispectral imaging systems”. In: *Journal of Biomedical Optics* 23 (2018), pp. 23 - 23 –12.

- [106] J. Gutiérrez-Gutiérrez, A. Pardo, E. Real, J. López-Higuera and O. M. Conde. “Custom Scanning Hyperspectral Imaging System for Biomedical Applications: Modeling, Benchmarking, and Specifications”. In: *Sensors* 19.7 (Apr. 2019), p. 1692.
- [107] R. B. Saager, M. L. Baldado, R. A. Rowland, K. M. Kelly and A. J. Durkin. “Method using *in vivo* quantitative spectroscopy to guide design and optimization of low-cost, compact clinical imaging devices: emulation and evaluation of multispectral imaging systems”. In: *Journal of Biomedical Optics* 23.4 (2018), pp. 1–12.
- [108] J. Huang. “Multispectral imaging of skin oxygenation”. PhD thesis. The Ohio State University, 2013.
- [109] C. Bernet, O. Desebbe, S. Bordon, C. Lacroix, P. Rosamel, F. Farhat, J.-J. Lehot and M. Cannesson. “The impact of induction of general anesthesia and a vascular occlusion test on tissue oxygen saturation derived parameters in high-risk surgical patients”. In: *Journal of Clinical Monitoring and Computing* 25.4 (Sept. 2011), p. 237. ISSN: 1573-2614.
- [110] E. Futier, S. Christophe, E. Robin, A. Petit, B. Pereira, J. Desbordes, J.-E. Bazin and B. Vallet. “Use of near-infrared spectroscopy during a vascular occlusion test to assess the microcirculatory response during fluid challenge”. In: *Critical Care* 15.5 (2011), R214.
- [111] D. Jakovels and J. Spigulis. “RGB imaging device for mapping and monitoring of hemoglobin distribution in skin”. In: *Lithuanian Journal of Physics* 52.1 (2012), pp. 50–54.
- [112] C. Mayeur, S. Campard, C. Richard and J.-L. Teboul. “Comparison of four different vascular occlusion tests for assessing reactive hyperemia using near-infrared spectroscopy”. In: *Critical care medicine* 39.4 (2011), pp. 695–701.
- [113] P. M. McNamara, J. O’Doherty, M.-L. O’Connell, B. W. Fitzgerald, C. D. Anderson, G. E. Nilsson, R. Toll and M. J. Leahy. “Tissue viability (TiVi) imaging: temporal effects of local occlusion studies in the volar forearm”. In: *Journal of Biophotonics* 3.1-2 (Aug. 2009), pp. 66–74.
- [114] R. M. Halder, H. N. Pham, J. Y. Breadon and B. A. Johnson. “Micropigmentation for the Treatment of Vitiligo”. In: *The Journal of Dermatologic Surgery and Oncology* 15.10 (1989), pp. 1092–1098. DOI: [10.1111/j.1524-4725.1989.tb03129.x](https://doi.org/10.1111/j.1524-4725.1989.tb03129.x).
- [115] M. D. Njoo and W. Westerhof. “Vitiligo”. In: *American Journal of Clinical Dermatology* 2.3 (June 2001), pp. 167–181. ISSN: 1179-1888. DOI: [10.2165/00128071-200102030-00006](https://doi.org/10.2165/00128071-200102030-00006).

- [116] W. F. Cheong, S. A. Prahl and A. J. Welch. “A review of the optical properties of biological tissues”. In: *IEEE Journal of Quantum Electronics* 26.12 (Dec. 1990), pp. 2166–2185. ISSN: 1558-1713. DOI: [10.1109/3.64354](https://doi.org/10.1109/3.64354).
- [117] Publication, CIE. “CIE 15: Technical Report: Colorimetry, 3rd edition”. In: *Vienna, Austria: CIE Central Bureau* 3 (2004).

Part II

Original Papers

Skin color simulation - review and analysis of available Monte Carlo-based photon transport simulation models

Paper A

This chapter is a reprint of the publication:

Jacob R. Bauer; Marius Pedersen; Jon Y. Hardeberg; and Rudolf M. Verdaasdonk; “Skin color simulation - review and analysis of available Monte Carlo-based photon transport simulation models“ *CIC25, 25th Color and Imaging Conference: Color Science and Engineering Systems, Technologies, and Applications*, Lillehammer, Norway, 2017.

Skin color simulation - review and analysis of available Monte Carlo-based photon transport simulation models

Jacob R. Bauer¹, Marius Pedersen¹, Jon Y. Hardeberg¹, Rudolf Verdaasdonk²;

¹ NTNU Department of Computer Science, The Norwegian Colour and Visual Computing Laboratory, Gjøvik, Norway

² VU University Medical Center Dept. of Physics & Medical Technology, Amsterdam, Netherlands

Abstract

Optical assessment is a useful tool for non-invasive skin assessment avoiding scarring, time delayed diagnosis, hurting, and inconvenience for patient and practitioner. This has led to wide adaptation of digital imaging and other optical technologies in dermatology. Many of these optical technologies lack quantifiability, therefore, the reproduction, comparison or absolute meaning of measurements or images is an open challenge. Monte Carlo simulation for multi-layered turbid media provides an accurate tool for simulating the optical path of photons traversing in the skin and the diffuse spectral reflectance of skin. With this tool at hand the missing link between health metrics and measurable optical phenomena can be provided and it can help to establish optical assessment and digital images as a standard for health monitoring of skin. A number of publicly available simulation codes and several different approaches have been proposed. In this work we give an overview of three Monte Carlo simulation tools and compare the different approaches. Furthermore, we will use Monte Carlo Simulations to generate different spectra based on varying optical properties and use these spectra to generate colour patches to analyse the impact of different optical properties on the resulting RGB colour patches.

Introduction

Useful health information with a minimal impact for the patient can be achieved through optical techniques. Common optical techniques for skin assessment are diffuse reflectance spectroscopy [1–3] and standard RGB sensors [4–7]. Quantifiability of these medical skin imaging or optical health assessment technologies is an open challenge. Several approaches to obtain more reliable and quantifiable results are based on photon simulation in tissue [8–15]. Next to the bio medical field optical skin simulation has been applied in the computer graphics community in order to generate realistic looking skin. The complexity of the models used has been gradually increasing incorporating and taking into account more physiological properties. Nevertheless the impact of research in the computer graphics community did not have a big effect on the bio medical sector [16]. Many of the techniques are based on diffusion theory [17].

Also some proposed techniques for the simulation of tissue light interaction in the bio medical field are based on diffusion theory [3, 15] or and many on Monte Carlo sampling [8, 12, 18]. Diffusion theory is only applicable under the assumption that the scattering dominates over absorption [3] and is limited for thin layers. It is computationally efficient and can provide results in near real time [19].

Monte Carlo simulation on the other hand is considered to provide accurate [9] results of tissue light interactions unrelated to the thickness of the layers. It is a sampling technique allowing an accurate description of light transport over a wide range of length scales. This can be performed in absence of a complete analytic model due to statistical sampling. Each photon is hereby simulated with an energy level and moved through the predefined medium interacting with it based on optical parameters and statistical sampling. The photon energy decomposition and its directionality are preserved. Simulation provides insights into complex light tissue interactions including photon path length traveled, depth sensed, spectral response and others. It allows investigation of the influence of optical properties which can be difficult or impossible to control. Publicly available implementations of Monte Carlo simulation have been used in recent years [8, 12]. Wang *et al.* [12] proposed a versatile publicly available C implementation in 1995, which has found great attention in the scientific community and resulted in many studies [8–10, 13]. New implementations of Monte Carlo simulation have emerged and are making use of the graphics processing unit (GPU) in modern computers. One example of such a code is the GPU based MCX code by Fang *et al.* [8]. Fang's implementation is based on the same general principles but is designed to be executable on modern GPUs which allows the calculation of multiple photons at the same time speeding up the simulation process significantly.

In this study we compare different implementations of Monte Carlo simulation for skin. Namely the MCML (Monte Carlo for multi-layered media) by Wang *et al.* [12], MCXYZ (3D Monte Carlo) for heterogeneous tissue code published by Jacques *et al.* [20] and the MCX Monte Carlo extreme implementations including MMC (mesh based Monte Carlo) by Fang *et al.* [8] We will compare the simulation results and give insights on how to use the different Monte Carlo simulation codes for simulating diffuse spectral reflectance of skin. These simulated spectra will be used to generate color and the influence of different parameters onto the final color patches will be compared. They can give information about the relationship between skin color and health relevant chromophore concentrations and the impact of underlying pathologies or structures onto the skin color. Furthermore, the generated images can illustrate the impact of different light sources used for skin imaging and its influence on the final color image.

Background Skin optical properties

In the following section we discuss general skin optical properties based on the book by Wang *et al.* to give an overview of the

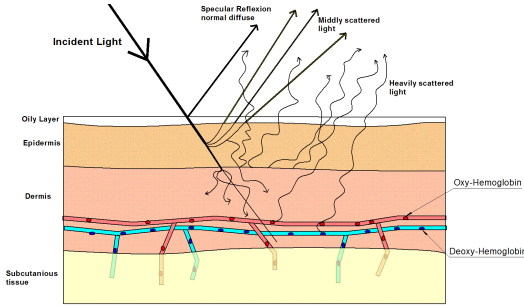


Figure 1. General skin structure and simplified interaction of skin and radiation. Figure reproduced from Bauer [22].

relevant parameters for optical skin simulation [21]. The interaction of light and tissue is mainly based on scattering and to a significantly smaller degree on absorption. The absorption is especially weak in the 400-1350nm spectral region and the mean free path between photon scattering events is on the order of 0.1mm compared to the mean absorption path length in the order of 10-100nm. In order to simulate skin we have to define optical properties and formulate a general model describing the skin structure. As a simplification skin can be described as a three layer model with three main layers defining different areas of optical properties. These layers are usually the epidermis, dermis and the subcutaneous tissue from the outside to the inside of the skin. Figure 1 shows the simplified light tissue interaction we use for the definition of our input tissue structure for simulation. Absorption plays a significant smaller role compared to scattering events for light simulation. The absorption can be described as:

$$I_0/I = -\mu_a dx, \quad (1)$$

where x denotes the distance traveled of the light, I_0 denotes the incoming light and I the outgoing light in a set up where light is incident to a medium and the resulting light on the other side is measured. The equation describes the proportionality percentage of the light absorbed in the interval $(x, x+dx)$ to the product of μ_a and dx . This is usually formulated in the well known Beer Lambert law as:

$$I(x) = I_0 e^{-\mu_a x}. \quad (2)$$

Specific components in the skin the so called chromophores can be considered the main absorbers in skin and are of interest for skin and general health assessment. Figure 2 shows the absorption coefficients of the most common chromophores in biological tissue per wavelength. These absorption curves can then be used to define the total absorption of the different skin layers with varying concentrations of the different chromophores. The optical properties are mainly governed by scattering in the tissue. To describe the scattering properties we define the scattering coefficient μ_s as the probability of photon scattering in a medium per unit path length [21]. This leads to Beer's law describing the probability of a photon propagating distance x without a scattering event,

$$T(x) = e^{-\mu_s x}. \quad (3)$$

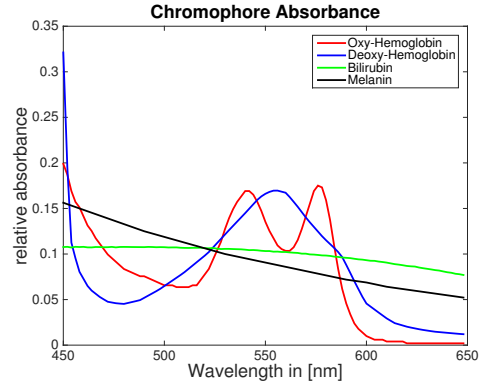


Figure 2. Optical absorption spectrum of common chromophores in human skin data from Jacques et al. [23]

$T(x)$ is hereby the ballistic transmittance and μ_s the reduced scattering coefficient. The scattering is strongest for biological structures with a size which matches the optical wavelength of the photon, therefore the scattering is wavelength dependent. Another important property for optical skin simulation is the so called anisotropy factor g . This factor is defined as the $\cos(\Theta)$ with values from -1 to 1. Θ describes the angle of the scattering direction and $g = 0$ corresponds to isotropic scattering and 1 dominantly forward scattering and correspondingly -1 dominantly backward scattering. In biological tissue the anisotropy factor is usually 0.9 so mainly forward scattering [21].

The last important quantity for Monte Carlo simulation is the fluence rate F . Fluence rate F measured in W/cm^2 is commonly the output of Monte Carlo simulation tools. It refers to the irradiance which is incident from all angles onto a small region of space [23]. This is used for turbid media where light is scattered towards the target from all directions. It describes the total irradiance impinging onto a target region from all directions. The fluence rate F is the power absorbed by that region, $P_{absorbed}$, divided by its cross sectional area, A (total area of the light cross section):

$$F = P_{absorbed}/A. \quad (4)$$

In the case of a small region the fluence rate is independent on the size of the region and depends on the primary plus secondary irradiance impinging onto that region.

Skin simulation

The simulation requires the definition of skin optical properties, specific structures and the user choices of simulation parameters. Simulation parameters include: number of photons, volume (input structure), properties (optical properties of the structure usually μ_s, μ_a, n, g), $t_{start}, t_{step}, t_{end}$ or the duration of the simulation, source position, source direction, type of source. In the cases discussed in this paper the input structure is a 2D structure a 3D cube or mesh grid. Each layer, voxel or triangle respectively is associated to optical properties defined as an input variable for the simulation. The absorption μ_a is calculated as a combina-

tion of several parameters including the blood concentration with oxygenated hemoglobin and deoxygenated hemoglobin, melanin concentration, and water concentration. It is then calculated with the following formula:

$$\mu_a = B * (S * \mu_a(\lambda)_{oxy} + (1 - S) * \mu_a(\lambda)_{deoxy}) + W * \mu_a(\lambda)_{wat} + M * \mu_a(\lambda)_{mel} \quad (5)$$

In which B denotes the total blood concentration S denotes an oxygenation saturation and W and M correspond to the melanin and water concentrations. Depending if the voxel belongs to the dermis or the epidermis these values vary. In healthy skin we would not expect the majority of melanosomes in the epidermis and only a small amount of oxy- and deoxyhemoglobin in the epidermis [24]. Equally we would expect a small concentration of melanin in the dermis and a higher concentration of blood including oxy- and deoxy-hemoglobin in the dermis. Additionally areas with for example increased melanin concentration could be defined and correspond for example to a mole in the epidermis.

The next parameter which has to be defined is the μ_s reduced scattering coefficient. Jacques [25] proposed a formula which has been used extensively in the domain of skin simulation to calculate the scattering coefficient wavelength dependent.

$$\mu'_s(\lambda) = a' (f_{ray} (\frac{\lambda}{500nm})^{-4} + (1 - f_{ray}) (\frac{\lambda}{500nm})^{-b_{mie}}) \quad (6)$$

To obtain a dimensionless equation dependent on the wavelength it is normalised and divided by the reference wavelength at 500nm. The factor a' is the $\mu_s(500nm)$ scattering coefficient at 500nm. Wavelength dependence is then described separately for its Rayleigh scattering contribution and its mie scattering contribution. All the different simulation algorithms examined in this paper require the definition of these structures priori to run time.

Monte Carlo simulation of photon transport follows this simulation pattern or concept. Each photon has an initial amount of energy and is propagated in a direction. In the beginning this direction is defined by the user input parameters for the x_{focus}, y_{focus} and z_{focus} . Each photon is then moved a specific step forward in case the photon crossed a boundary it is either reflected or transmitted in the case it did not cross a boundary it will be absorbed or scattered. The absorption properties of the medium define the amount of energy absorbed by the corresponding voxel. Scattering properties and Monte Carlo sampling define the new direction of the photon. As the last step of one iteration the photon depending on the energy left and a random roulette is either terminated or it will go through the whole cycle again. This whole process is continued until the last photon died which terminates the algorithm.

MCML Monte Carlo for multi layered media (MCML) is a Monte Carlo simulation code which has been publicly available since 1995 and was released by Wang *et al.* [12] [23]. It has been used by many research groups in the past years some examples are it was utilised to generate lookup tables providing the link between diffuse spectral reflectance and chromophore concentrations in phantoms by Hennesy *et al.* [26], to obtain look up tables for a multiple regression approach to obtain melanin and hemoglobin concentration by Nishidate *et al.* [13], it has been extended to consider 3D structures in skin by Paquitt *et al.* [27] and

Naglic *et al.* combined MCML with diffusion theory to get health information from diffuse spectral reflectance [10]. The model on which MCML is based on considers multilayered skin as infinite wide layers parallel to each other. Light is introduced to this structure perpendicular to these layers. MCML works in a cylindrical space with a radial coordinate system assuming an indefinite expansion if the optical properties provided to the model. It is build to simulate the photon transport through these media and considers photons as particles therefore polarisation and wave properties are neglected.

Table 1 shows the input properties for the MCML code. The optical properties of the layers μ_s, μ_a, n, g can then be calculated from given blood, melanin and oxygen saturation values according to the formulas discussed in section .

MCXYZ Monte Carlo XYZ indicating the dimensionality of the model (MCXYZ) is a C code provided by Jacques *et al.* [23] it is designed to work with 3D cubes which are composed of 3D voxels. It is provided including two Matlab scripts allowing the preparation of the input file and the viewing of simulation results. In order to use the code several parameters have to be defined with some variations compared to general Monte Carlo parameters. Most of them are inherit to the architecture of the tissue definition. Defining the optical properties can be considered as the definition of a palette of tissue types each tissue type gets an integer identifier 1-19 and its optical properties (μ_s, μ_a, g). These can then be used to define the 3D structure which contains a 3D cube with the corresponding tissue type identifier. The Matlab file maketissue.m can be used to define different tissues by creating shapes inside the defined cube. MCXYZ can then be used to simulate the light tissue interaction with the input structure.

MCX Another Monte Carlo simulation tool we will consider is the Monte Carlo extreme (MCX) implementation being the most recent implementation by Fang *et al.* [8] it is completely parallelised and optimised to run on a GPU. Parallelisation and GPU processing can speed up the Monte Carlo simulation significantly, since each photon can be treated individually and many photons can be processed simultaneously. This speeds up the simulation time by a factor of 300 or more, depending on the computing power of the GPU used [8]. Due to the different implementation MCX also requires some additional input variables compared to the unparallelised mcml and MCX described in section . The MCX code follows a similar concept to the MCXYZ code based on a cubic voxel grid, where each element has optical properties assigned to it. General functionality is close to MCXYZ but it provides a lot more flexibility for the user to define the input lightsource. Additionally it runs significantly faster to the unparallelised MCXYZ code. This comes of course with the necessity of a CUDA capable graphics card to use this implementation.

MMC Fang also proposed MMC a mesh based Monte Carlo simulation code. This code is not parallelised (at the time of writing of this paper) for a GPU but it is the principles are the same to the MCX code. The main difference between MMC and MCX is the input structure definition since, it is based on a mesh definition of the input structure. So to define the tissue structure it requires nodes for a tetrahedral mesh grid and an element ar-

Table 1: Monte Carlo methods predefined variables

General Monte Carlo	MCML	MCXYZ	MCX
number of photons	input file	determined by simulation time	defined as input
volume (input structure)	just layers considered infinitely wide	3D voxel integers (1-19)	3D voxel integers
optical properties(μ_s, μ_a, n, g)	input file	list defining tissue 1-19	list defining tissue
simulation time	determined by number of photons	total simulation time defined	$t_{start}, t_{end}, t_{step}$
source position	on top of the tissue	x,y, z, coordinates	x,y, z, coordinates
source direction	perpendicular to tissue in z(depth)	$x_{focus}, y_{focus}, z_{focus}$	$x_{focus}, y_{focus}, z_{focus}$
type of source	infinitely narrow beam	uniform, gaussian, isotropic pt	14 different types
wavelength	defined in input file	wavelength for simulation	wavelength for simulation
cuda parameters	none	none	$n_{blocksize}, n_{threads}, seed, max_{gate}$
detector definition	none	none	define locations of detectors

ray. This allows an even more efficient definition of very thin layers and can result in significant computational efficiency improvements. Furthermore a mesh grid input definition allows for different and more complex structures opposed to the voxel definition of MCXYZ.

Experiments

We have simulated a 3 layer skin structure using the MCML (Monte Carlo for multilayered media). As a proof of concept we chose the implementation and optical properties published by Atencio *et al.* [24]. Atencio *et al.* have used MCML to generate spectra for different concentrations of bilirubin in the dermis region of the skin. We defined the optical properties of the skin and ran the simulations and plotted the resulting spectra with varying bilirubin concentrations in the epidermal layer. Figure 3 shows the results obtained by simulating the different amounts of bilirubin in the dermis region of skin.

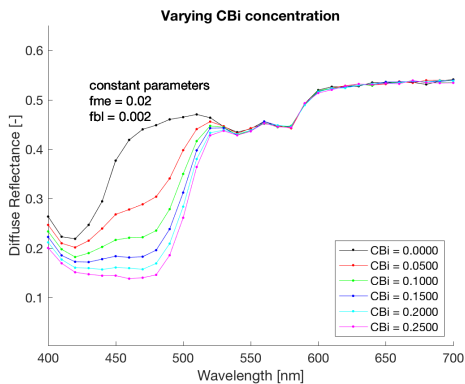


Figure 3. Different concentrations of bilirubin in the skin simulated spectra using MCML and the configuration proposed by Atencio *et al.* [24]

We then used these simulated spectra for the generation of colour patches based on Monte Carlo simulations. As a first step we simulated a simple 3 layer model using the mcml implementation discussed in section and using publicly available Matlab code. The model and the code used for the simulation is publicly available by Atencio *et al.* and discussed in detail in [24]. It is based on a 3 layer model with a thin epidermal layer a hypodermis and a bone layer, this model assumes the measurement

on the skull of neonatal babies. The optical parameters mainly the concentrations of different chromophores in the skin for the simulation were varied between the different runs but the structure itself remained unchanged. In order to simulate with different chromophore concentration we had to adjust the publicly available simulation code by Atencio *et al.*, while still keeping the general structure. Three experiments were performed, while changing different chromophores Melanin, Bilirubin and the total blood concentration (haemoglobin). Correspondingly we kept the other chromophore concentrations constant in this experiment. The mcml code was then used to generate diffuse spectral reflectance curves with known chromophore concentrations. In or-

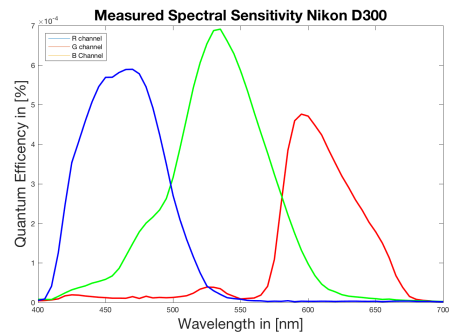


Figure 4. Measured spectral sensitivities of a Nikon D300

der to simulate colour patches we assumed the mcml resulting spectra, the camera sensitivity curves of a Nikon D300, and in this proof of concept study we used a white LED as the primary lightsource. The sensitivities of the camera were measured prior to this experiment and can be seen in Figure 4.

In figure 5 we plotted different resulting colour patches B1-B6 the numbers under the images indicate the different total blood concentration. We can clearly see the trend of increasing redness depending on the total blood concentration in the model. This agrees well with the expectations for increased blood concentration in the tissue. Due to the optical properties of haemoglobin we would expect a more reddish appearance of the skin. In the next set of simulations, shown in figure 6, we varied the bilirubin. Bilirubin is another chromophore which occurs naturally as a decomposition product of haemoglobin. So commonly we would see higher bilirubin after bruising the skin.

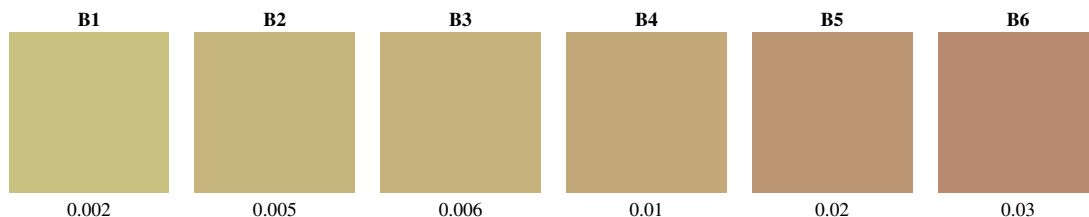


Figure 5. Colour patches based on Monte Carlo simulations with varying blood concentration as an input variable

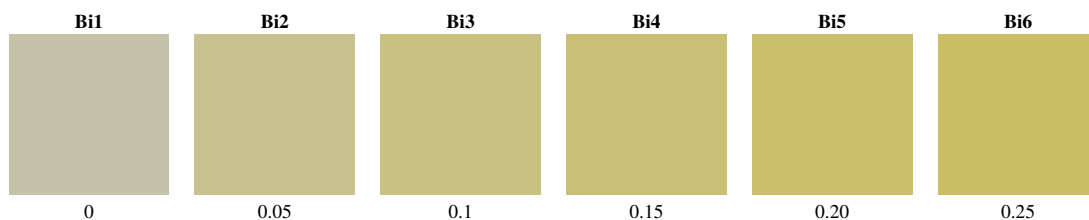


Figure 6. Colour patches based on Monte Carlo simulations with varying bilirubin concentration as an input variable

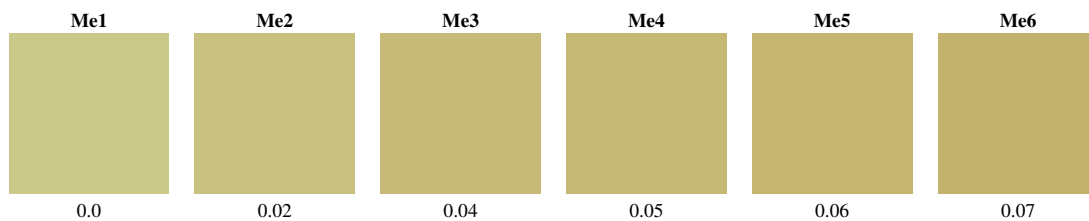


Figure 7. Colour patches based on Monte Carlo simulations with varying melanin concentration as an input variable

The results shown in figure 6 also agree well with expectations. A higher bilirubin results in a more yellowish appearing skin. Bilirubin in newborns can be a deadly disorder if not treated accordingly. The detection of bilirubin as soon and as non-invasive as possible is therefore of great importance. We can observe the increasing yellowness in our simulation results very well. In the next experiment we increased the melanin concentration in the epidermal region. Also these results shown in figure 7 agree well with expectations. Melanins with its high absorbance colours the skin in a brown or darker shade. We can observe this colouring in the simulated melanin colour patches.

Conclusion

MCML assumes a homogenous tissue it provides good results for small skin volumes or for simulating probe measurements. In the case of spatial skin imaging we are especially interested in the inhomogeneous aspects therefore MCML is less suitable. Nevertheless the MCML simulations and the generated skin patches show the expected behaviour.

This paper gives an overview of publicly available Monte Carlo simulation codes and outlines some of their capabilities and limitations. The given codes have been described and differences have been pointed out. Additionally we performed a basic quan-

titative comparison of the methods by running the different codes with similar input parameters and we are reporting the results. MCX (Monte Carlo extreme) stands out from the implementations discussed since it has the most advanced light source definition, a flexible 3D structure to define the input tissue and has run time and computational efficiency advantages over the other implementations. For very thin layers (like skin) we recommend the MMC implementation, since the runtime should be further decreased by the efficient representation of the input structure in the form of tetrahedral. It comes even more apparent if the author provides a parallelised version of the MMC code. Furthermore we performed an experiment in order to evaluate the usefulness of MonteCarlo simulated spectra for visualising different chromophore concentration levels. As a proof of concept this approach shows good results. All the different chromophores simulated for this study show good agreement with expectations. This could be useful in educational purposes for dermatologists in order to aid to give them a better understanding how depth or general concentration of these chromophores influences the resulting colours imaged by for example a digital three channel sensor. Furthermore, the mechanisms of colour image formation and chromophore concentrations can be further studied.

Acknowledgements

This research has been supported by the Research Council of Norway through project no. 247689 IQ-MED: Image Quality enhancement in MEDical diagnosis, monitoring and treatment.

Author Biography

Jacob Renzo Bauer received his Bachelor in Mediatechnology and Photoengineering from the University of Applied Science Cologne (2013) and his Master of Science in Color in Informatics and Mediatechnology (2015) from the European Erasmus Mundus Consortium University of Eastern Finland, Universidad de Granada and UJM Universitee Jean Monnet. Since January 2016 he is enrolled in a PhD program at the Norwegian University of Science and Technology in Gjøvik. His work is focused on imaging science, spectral science and medical applications of spectral imaging techniques.

References

- [1] R Rox Anderson and John A Parrish. The optics of human skin. *Journal of investigative dermatology*, 77(1):13–19, 1981.
- [2] Bing Yu, Justin Y Lo, Thomas F Kuech, Gregory M Palmer, Janelle E Bender, and Nirmala Ramanujam. Cost-effective diffuse reflectance spectroscopy device for quantifying tissue absorption and scattering in vivo. *Journal of Biomedical Optics*, 13(6):060505–3, 2008.
- [3] Lise Lyngsnes Randeberg. *Diagnostic applications of diffuse reflectance spectroscopy*. PhD thesis, NTNU, 2005.
- [4] Dainis Jakovels, Ilona Kuzmina, Anna Berzina, Lauma Valeine, and Janis Spigulis. Noncontact monitoring of vascular lesion phototherapy efficiency by RGB multispectral imaging. *Journal of Biomedical Optics*, 18(12):126019–126019, December 2013.
- [5] Dainis Jakovels and Janis Spigulis. RGB imaging device for mapping and monitoring of hemoglobin distribution in skin. *Lithuanian Journal of Physics*, 52(1):50–54, 2012.
- [6] Izumi Nishidate, Takaaki Maeda, Kyuichi Niizeki, and Yoshihisa Aizu. Estimation of Melanin and Hemoglobin Using Spectral Reflectance Images Reconstructed from a Digital RGB Image by the Wiener Estimation Method. *Sensors*, 13(6):7902–7915, June 2013.
- [7] Izumi Nishidate, Kiyohiro Sasaoka, Testuya Yuasa, Kyuichi Niizeki, Takaaki Maeda, and Yoshihisa Aizu. Visualizing of skin chromophore concentrations by use of RGB images. *Optics Letters*, 33(19):2263, 2008.
- [8] Qianqian Fang and David A Boas. Monte Carlo Simulation of Photon Migration in 3D Turbid Media Accelerated by Graphics Processing Units. *Optics Express*, 17(22):20178–20190, 2009.
- [9] Steven L Jacques and Lihong Wang. Monte Carlo Modeling of Light Transport in Tissues. In *Optical-Thermal Response of Laser-Irradiated Tissue*, pages 73–100. Springer US, Boston, MA, 1995.
- [10] Peter Naglič, Luka Vidovič, Matija Milanič, Lise L. Randeberg, and Boris Majaron. Combining the diffusion approximation and Monte Carlo modeling in analysis of diffuse reflectance spectra from human skin. In *Proc. SPIE*, volume 8926, pages 89260U–89260U–13, 2014.
- [11] G Zonios, J Bykowski, and N Kollias. Skin melanin, hemoglobin, and light scattering properties can be quantitatively assessed in vivo using diffuse reflectance spectroscopy. *The Journal of investigative dermatology*, 117(6):1452–1457, December 2001.
- [12] Lihong H Wang, Steven L Jacques, and L Q Zheng. MCML - Monte-Carlo Modeling of Light Transport in Multilayered Tissues. *Computer Methods and Programs in Biomedicine*, 47(2):131–146, July 1995.
- [13] Izumi Nishidate, Yoshihisa Aizu, and Hiromichi Mishina. Estimation of melanin and hemoglobin in skin tissue using multiple regression analysis aided by Monte Carlo simulation. *Journal of Biomedical Optics*, 9(4):700, 2004.
- [14] Caigang Zhu and Quan Liu. Review of monte carlo modeling of light transport in tissues. *Journal of Biomedical Optics*, 18(5):050902–050902, 2013.
- [15] Thorsten Spott and Lars O Svaasand. Collimated light sources in the diffusion approximation. *Applied Optics*, 39(34):6453–6465, 2000.
- [16] Gladimir V.G. Baranoski and Aravind Krishnaswamy. Ch. 5 - simulations in health and life sciences. In *Light Skin Interactions*, pages 81 – 97. Morgan Kaufmann, Boston, 2010.
- [17] Gladimir V.G. Baranoski and Aravind Krishnaswamy. Ch. 8 - diffusion approximation approach. In *Light Skin Interactions*, pages 129 – 140. Morgan Kaufmann, Boston, 2010.
- [18] S. V. Patwardhan, A. P. Dhawan, and P. A. Relue. Monte carlo simulation of light-tissue interaction: three-dimensional simulation for trans-illumination-based imaging of skin lesions. *IEEE Transactions on Biomedical Engineering*, 52(7):1227–1236, July 2005.
- [19] Asgeir Bjorgan, Matija Milanič, and Lise Lyngsnes Randeberg. Estimation of skin optical parameters for real-time hyperspectral imaging applications. *Journal of Biomedical Optics*, 19(6):066003–066003, June 2014.
- [20] Steven L Jacques. Coupling 3D Monte Carlo light transport in optically heterogeneous tissues to photoacoustic signal generation. *Biochemical Pharmacology*, 2(4):137–142, December 2014.
- [21] Lihong V. Wang and Hsin-I Wu. *Biomedical Optics: Principles and Imaging*, chapter Appendix A: Definitions of Optical Properties, pages 343–346. John Wiley Sons, Inc., 2009.
- [22] Jacob Renzo Bauer. Spectral Reflectance Estimation with an Optical Non-Contact Device for Skin Assessment. Master’s thesis, University of Eastern Finland, Joensuu, July 2015.
- [23] Steven L Jacques and Scott A Prahl. A collaboration of Oregon Health & Science University, Portland State University, and the Oregon Institute of Technology. Optical Spectra, 2015.
- [24] Jose A Delgado Atencio, Steven L Jacques, and S Vázquez Montiel. *Monte Carlo Modeling of Light Propagation in Neonatal Skin*. InTech, February 2011.
- [25] Steven L Jacques. Corrigendum: Optical properties of biological tissues: a review. *Physics in Medicine and Biology*, 58(14):5007–5008, June 2013.
- [26] Ricky Hennessy, Sam L Lim, Mia K Markey, and James W Tunnell. Monte Carlo lookup table-based inverse model for extracting optical properties from tissue-simulating phantoms using diffuse reflectance spectroscopy. *Journal of Biomedical Optics*, 18(3):037003–5, March 2013.
- [27] Vincent C Paquit, Jeffery R Price, Fabrice Mériaudeau, and Kenneth W Tobin. Improving light propagation Monte Carlo simulations with accurate 3D modeling of skin tissue. In *2008 15th IEEE International Conference on Image Processing*, pages 2976–2979. IEEE, 2008.

Optical skin assessment based on spectral reflectance estimation and Monte Carlo simulation

Paper B

This chapter is a reprint of the publication:

Jacob R. Bauer; Jon Y. Hardeberg; and Rudolf M. Verdaasdonk; “Optical skin assessment based on spectral reflectance estimation and Monte Carlo simulation,” *Proceedings of SPIE Volume 10057, Multimodal Biomedical Imaging XII*; 1005703 (2017) <https://doi.org/10.1117/12.2252097> Event: BIOS, 2017, San Francisco, California, United States.

PROCEEDINGS OF SPIE

[SPIDigitalLibrary.org/conference-proceedings-of-spie](https://spiedigitallibrary.org/conference-proceedings-of-spie)

Optical skin assessment based on spectral reflectance estimation and Monte Carlo simulation

Jacob R. Bauer, Jon Y. Hardeberg, Rudolf Verdaasdonk

Jacob R. Bauer, Jon Y. Hardeberg, Rudolf Verdaasdonk, "Optical skin assessment based on spectral reflectance estimation and Monte Carlo simulation," Proc. SPIE 10057, Multimodal Biomedical Imaging XII, 1005703 (15 February 2017); doi: 10.1117/12.2252097

SPIE.

Event: SPIE BiOS, 2017, San Francisco, California, United States

Optical skin assessment based on spectral reflectance estimation and Monte Carlo simulation

Jacob R. Bauer^a, Jon Y. Hardeberg^a, and Rudolf Verdaasdonk^b

^aNTNU, Gjøvik, Norway, The Norwegian Colour and Visual Computing Laboratory

^bVU University Medical Center, Amsterdam, Netherlands, Dept. of Physics & Medical Technology

ABSTRACT

Optical non-contact measurements in general, and chromophore concentration estimation in particular, have been identified to be useful tools for skin assessment. Spectral estimation using a low cost hand held device has not been studied adequately as a basis for skin assessment. Spectral measurements on the one hand, which require bulky, expensive and complex devices and direct channel approaches on the other hand, which operate with simple optical devices have been considered and applied for skin assessment. In this study, we analyse the capabilities of spectral estimation for skin assessment in form of chromophore concentration estimation using a prototypical low cost optical non-contact device. A spectral estimation workflow is implemented and combined with pre-simulated Monte Carlo spectra to use estimated spectra based on conventional image sensors for chromophore concentrations estimation and obtain health metrics. To evaluate the proposed approach, we performed a series of occlusion experiments and examined the capabilities of the proposed process. Additionally, the method has been applied to more general skin assessment tasks. The proposed process provides a more general representation in form of a spectral image cube which can be used for more advanced analysis and the comparisons show good agreement with expectations and conventional skin assessment methods. Utilising spectral estimation in conjunction with Monte Carlo simulation could lead to low cost, easy to use, hand held and multifunctional optical skin assessment with the possibility to improve skin assessment and the diagnosis of diseases.

Keywords: spectral estimation, skin assessment, chromophore concentration, occlusion measurement, optical, non-contact

1. INTRODUCTION

Skin assessment is usually performed by visual examination by a physician. The diagnosis depends on the subjective judgement of the physician and the skin samples have to be extracted for further investigation of the health status. Optical measurements, on the other hand, could provide objective non-invasive examination. Hence these techniques could avoid scarring and pain for the patient during the diagnoses. Skin colorants like melanin, oxygenated hemoglobin and deoxygenated hemoglobin called chromophores and their concentrations can provide useful information about the health status of skin. This research addresses chromophore concentration estimation and mapping with a prior proposed skin assessment device based on spectral estimation in combination with Monte Carlo simulation.

The *SkImager* proposed by Spigulis et al.¹ is a low cost non-contact optical measurement device for skin assessment. It has been proposed designed and tested prior to this study, but will be a tool of investigation for this research. Jakovels et al.² used a similar technology for monitoring of vascular lesion phototherapy efficiency.

In this research we shall develop and investigate the capabilities of the *SkImager* for spectral estimation of skin reflectances. The estimates shall be used for skin assessment in general and skin chromophore estimation in particular, furthermore the process shall be extended with priori Monte Carlo simulated diffuse reflectance spectra.

Further author information: (Send correspondence to J.R.Bauer)

J.R.Bauer: E-mail: jacob.bauer@ntnu.no, Telephone: 0049 173 421 3461

Multimodal Biomedical Imaging XII, edited by Fred S. Azar, Xavier Intes, Proc. of SPIE Vol. 10057, 1005703 · © 2017 SPIE · CCC code: 1605-7422/17/\$18 · doi: 10.1117/12.2252097

Proc. of SPIE Vol. 10057 1005703-1

Processor	Nvidia Tegra 2 T20 a dual-core ARM Cortex-A9 processor (clock frequency 1 GHz)
Sensor	RGB CMOS, 3Mpix (2048 x 1536 pixels), Pixelsize: $3.2\mu\text{m}^2$ (MT9T031)
Storage	Removable SD card
Display	4.3 inch 480 x 272 pixel touchscreen
Dimensions	121 x 205 x 101 mm
Weight	$\sim 440\text{g}$

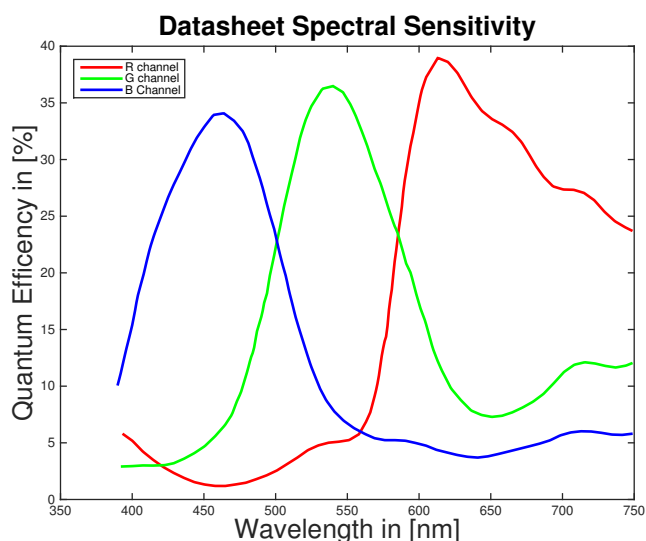
Table 1. Technical Data of the *SkImager* and the Aptina CMOS sensor

2. THEORETICAL BACKGROUND AND THE *SKIMAGER*

The *SkImager* is a previously proposed prototypical compact device for skin assessment. It was developed in the Biophotonics Laboratories in Riga Latvia and is described in detail in a previous publication.¹ A round skin spot illuminated with 5 polarized narrow band LED's can be imaged by a cross oriented polarized CMOS Sensor. The illuminations covers the VIS (visible) and IR (infra red) spectrum with narrow band LED's at 450nm , 540nm , 660nm and 940nm and a white LED. The controls of the *SkImager* are realized in form of a touchscreen on the back of the device. All parts are assembled in a 3D printed housing.

2.1 Spectral Sensitivity

The spectral sensitivity of the sensor is an important factor for the spectral estimation the data sheet sensitivities were taken to evaluate the coverage of spectral sensitivity along the visual spectral band. The spectral sensitivity

Figure 1. Spectral Sensitivity of the sensor in *SkImager* according to data sheet.

given by the manufacturer were used and are presented in Figure 1. These curves are an important factor of a sensor of an imaging system used for spectral estimation.

Both color quality and spectral estimation results are connected to the spectral sensitivity. Another very important spectral feature of an imaging system are the spectral power distributions of the LEDs discussed in the following section.

2.2 Spectral Power Distribution of the LEDs

The Spectral Power Distribution of the Illumination is an important aspect for modeling the reflectance of a sample with known spectral reflectance. To measure the spectral power distribution of the *SkImager* its

illumination was directed towards (0°) a reference white and the reflected light was measured with an *Avantes AvaSpec-ULS2048*. The measurement fibre was directed in a 45° angle towards the reference white to avoid specular reflections of the light source. Following the CIE norm ($0^\circ/45^\circ$) discussed in³



Figure 2. Measurement setup to measure the spectral power distribution of the LEDs in the *SkImager* with a $0^\circ/45^\circ$ measurement setup according to the CIE³

The *Avantes AvaSpec-ULS2048* with a spectral range of 350nm to 1100nm and a spectral resolution of 0.5nm was used. To account for the dark current and ambience light during the measurement a black measurement was taken and subtracted from the measurements. All measurements were repeated three times and averaged to decrease effects of random noise. Figure 3 shows the measured spectral power distributions of the illumination

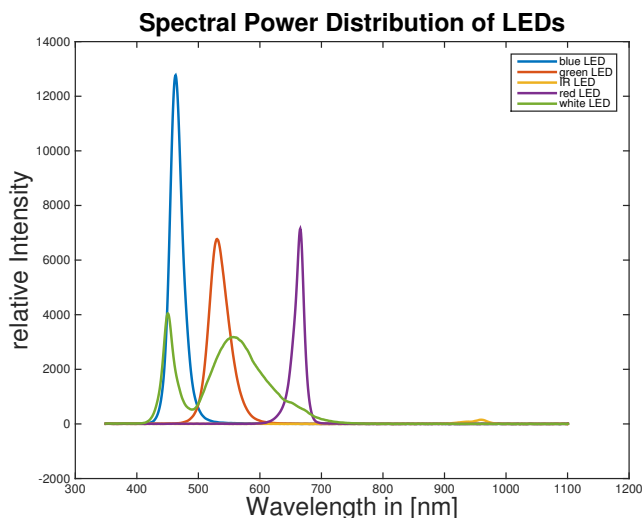


Figure 3. Relative measurement of the LED spectral power distribution measured as described in Section 2.2 and

in a relative measurement scale of the device. Figure 4 on the other hand shows a normalized spectrum ranging from 0 to 1.

To obtain the normalized spectra each value of all curves was divided by the curves maximum value. We can clearly see that the relative power of the IR LED was considerably lower than the other LEDs. The Blue LED provides by far the highest output.

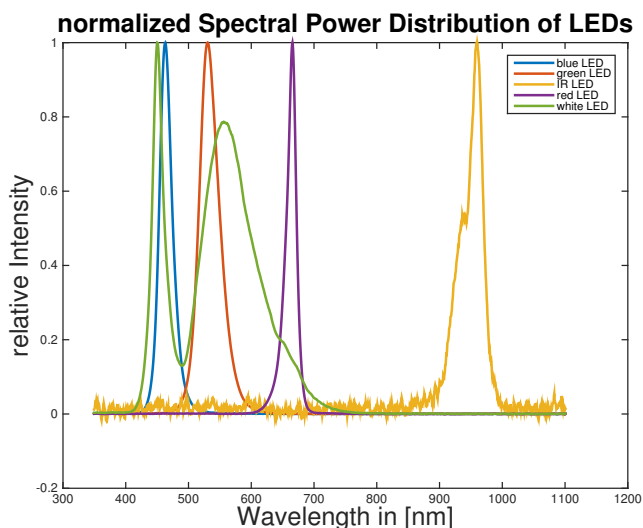


Figure 4. normalized LED spectral power distributions normalized by dividing with the highest value of each curve

2.3 Effective Spectral Sensitivity

In order to compute the effective spectral sensitivity per channel of the *SkImager* we multiplied the spectral power distribution of the LEDs and the spectral sensitivity of the sensor. The Figure 5 shows the effective sensitivity

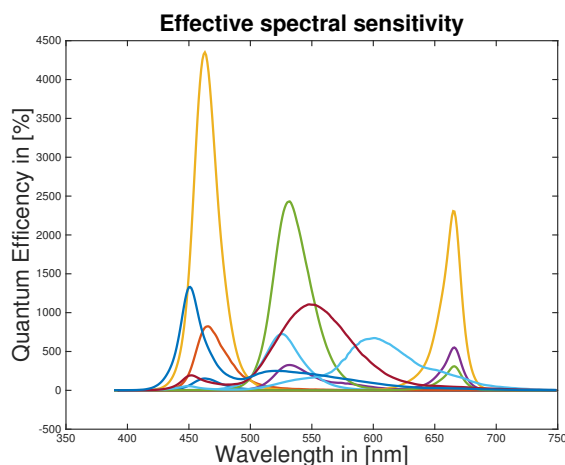


Figure 5. Effective spectral sensitivity computed by multiplication of SPD of the LEDs and spectral sensitivity of the Sensor

per channel in the visual range of the spectrum from (400 to 700nm) and shows that it is not evenly distributed over the spectral range. Infrared region of the spectrum was left out in this study also due to the fact that the manufactures didn't provide the spectral sensitivity of the sensor in this region. For spectral measurements or spectral estimation it is desirable to have an uniform spectral sensitivity over the whole range of the spectrum.

Both benefit from a spectrally uniform illumination with enough signal along the whole spectral band of interest. Especially, the signal is weak around 500nm were none of the illuminations provides an adequate output of energy.

3. METHODS

3.1 Monte Carlo Simulation

Prior to the spectral estimation we performed a series of Monte Carlo simulations using MCML by Wang et al.⁴ For the configuration of the MCML simulation we followed the published code by Atencio et al.,⁵ defining a 3 layer model. With an epidermis, dermis and subcutaneous tissue layer. In total we simulated four different sets of diffuse skin spectra changing the concentration of the dominant chromophore. One set of simulations with dominant oxyhemoglobin and different concentrations, one with different overall concentrations of blood with a constant oxygenation level, one set with dominant but varying bilirubin concentration and one set with dominant but varying melanin concentration.

In the case of oxyhemoglobin we changed the oxygen saturation of the blood from 0.20 - 0.70 in 0.10 steps, while keeping blood volume fraction constant (0.02 mg/L), melanin concentration constant(0.02 mg/dl) and a low level of bilirubin (0.1g/L) constant through the simulations. For the simulation with different volume

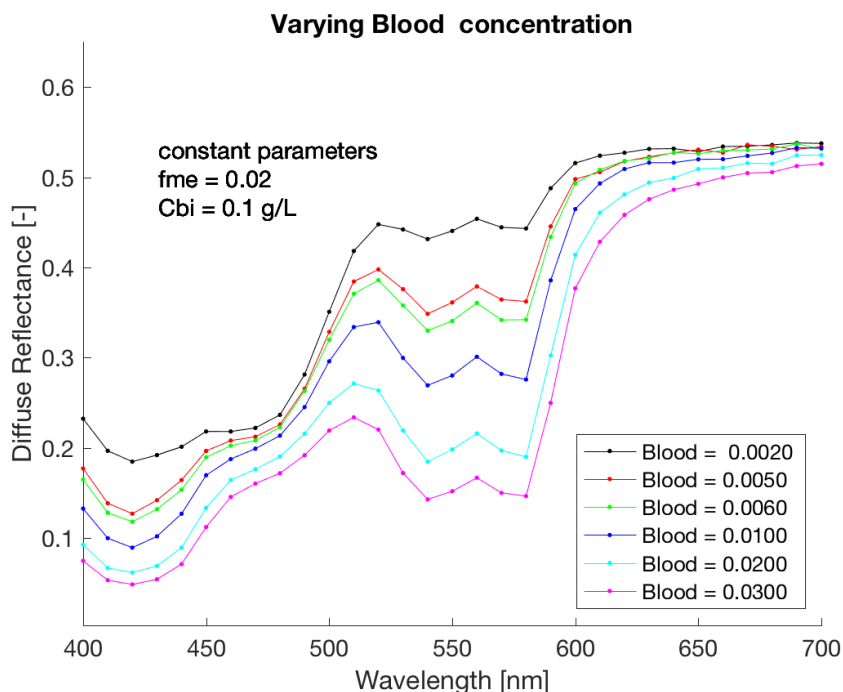


Figure 6. example of simulated spectra in this case with varying total blood concentration and constant bilirubin, oxygen saturation, and melanin based on plots MCML simulation code and theory proposed by Atencio et al.⁵

fractions of blood we kept the bilirubin concentration (0.1 g/L), melanin concentration (0.02) and the oxygen saturation (0.70) as constant, while varying the blood volume fraction to 0.002, 0.005, 0.006, 0.01, 0.02, 0.03. The plot for different blood concentrations can be seen in Figure 6.

Furthermore one set with changing the total bilirubin concentration (0 0.05 0.1 0.15 0.20 0.25) while keeping melanin (0.02), blood volume (0.02) fraction and oxygen saturation (0.70) constant was simulated. And similarly one set with varying melanin concentration keeping blood, oxygenation and bilirubin constant.

3.2 Linear Least Square Fitting in Lower Dimensional Space

The spectral estimation we choose is a linear least square fitting in a lower dimensional space also known as the *Imai Berns Method*.⁶ Lower dimensional reflectance factors are obtained by performing dimensionality reduction on a set of training reflectances. The method requires a prior taken training set with corresponding training reflectances. Principal component Analysis (PCA) is then performed on the training data set to obtain the linear base and the training set coefficients. This method is according to the authors⁶ more robust to noisy channels as a result of the optimization in a lower dimensional space. We then obtain a full spectral image cube with an estimated spectrum for each pixel in the image.

3.3 Chromophore estimation

The estimated spectra were used to estimate chromophore concentrations per pixel which can then be visualised using chromophore heat maps. An overview of the flow chart of the proposed method can be seen in

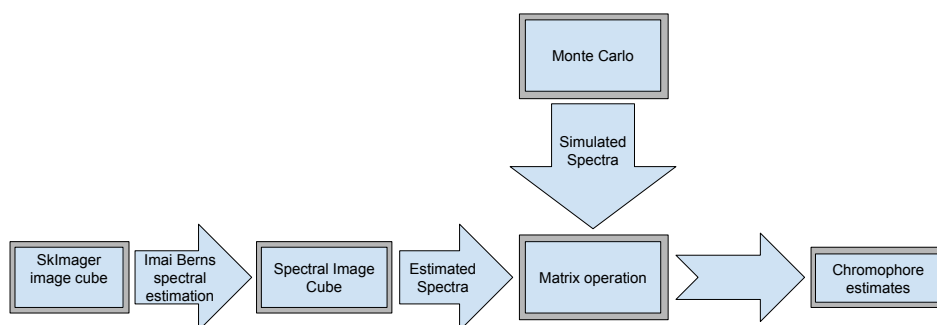


Figure 7. Flowchart of the proposed method, spectral estimations based on Imai Berns⁶ method are used in conjunction with Monte Carlo simulations to obtain chromophore estimates

Figure 7. The estimated spectra are used in conjunction with the simulated spectra to estimate chromophore concentrations. For the further investigation usually an average of a pixel mask was used to account for noise. A main consideration for the estimation of the chromophore concentration was computationally efficiency and robustness. Following the limitations of the *SkImager* hardware and to ensure a work flow with instantaneous results. All the development of algorithms was performed in *Matlab*. Considering computational efficiency in *Matlab* matrix operations are well suited. A simple matrix model was formulated to estimate the chromophore concentrations based on the Monte Carlo simulations with a dominant chromophore,

$$\tilde{C}C_{sxn} = C_{pxs} * \tilde{A}_{nxs}^T \quad (1)$$

where CC is the concentration of each chromophore per pixel, C is a matrix with the different Monte Carlo simulated spectra with p different dominant chromophores and \tilde{A}_{hxs} , \tilde{A}_{hxs} is the estimated absorption spectrum for each pixel (h) resulting from the *SkImager*.

3.4 Occlusion Measurement

In order to verify the performance of the proposed method. We performed the occlusion test often used to study diffusion of tissue.⁷⁻¹⁰ The occlusion test requires consecutive measurements of the hand of a patient who's arm is clamped with an inflatable cuff. Inflating the cuff blocks the incoming flow of blood and simultaneously stops the flow of blood out of the hand. The occlusion test is a well known study with a known outcome and therefore a suitable proof of concept measurement to verify the performance of the proposed algorithm. The concentration

of oxygenated Hemoglobin in the hand should fall exponentially during the occlusion (starting from the point of cuff inflation).⁷⁻¹⁰ Deoxygenated hemoglobin increases exponentially during the occlusion.⁸⁻¹⁰

In total 12 volunteers (4 female and 8 male) all caucasian skin type with 2 of the male subjects with darker skin and an age distribution from age 22–34 years were measured in a time frame of 5 minutes. The measurement setup was chosen to minimize the effects of specular reflection for the spectrophotometer measurement and to minimize the time between the two measurements. A white LED was used to take the spectral measurements as a result of the limited space for the measurement setup. The measurement geometry was $0^\circ/45^\circ$ with the

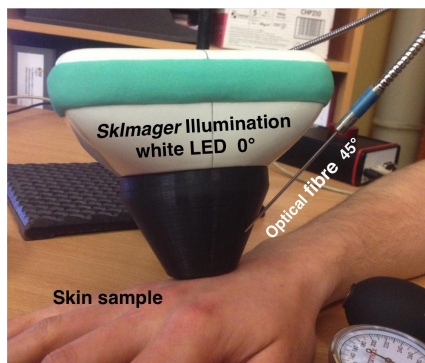


Figure 8. Measurement setup to measure the skin training set with ground truth reflectance measurement using *Avantes Avaspec* and the corresponding *SkImager* responses of the LEDs *SkImager* white LED illumination with a $0^\circ/45^\circ$ measurement Setup according to the CIE³

light source normal to the sample and the detector in a 45° angle to avoid specular reflections according to the CIE³ the setup can be seen in Figure 8. Using a white LED for the spectral measurements is not optimal but it was unavoidable for the limited space for the measurement setup. We can also consider the white LED as sufficiently uniform in the spectral band of interest (450 – 650nm). Considering the temporal arrangement of the measurement a single measurement with both devices took about 15 seconds where the *SkImager* imaging took 6 – 10 seconds and the spectrophotometer measurement about 5 seconds.

4. RESULTS AND DISCUSSION

In the following paragraph we discuss results of the proposed method applied to occlusion measurements. The chromophore estimation described in Section 3.3 based on prior estimated spectra calculated with the colorchecker training using 6 channels and the *Imai Berns* method as discussed in Section 3.2 and Monte Carlo simulated skin spectra. Figure 9 shows the results for all subjects. All subjects chromophore concentration images were averaged and then combined into one average subject. Average estimate concentrations were then plotted over time. The curve shows the exponential decay of oxygenated hemoglobin saturation during the 2 minute period of occlusion. We can clearly see a good agreement of the general expected shapes or physiological behaviour which has been discussed in the literature.⁷⁻¹⁰ The measurements were normed to have zero concentration for the first measurement by subtracting the average concentration of the first five measurements. Therefore, the plot shows relative changes over time compared to the base line measured prior to occlusion. Also the expected oxygen overshoot can be seen in the plots obtained through spectral estimation combined with monte carlo simulation.

5. CONCLUSION

In this research we analyzed an existing optical non-contact skin assessment device called *SkImager* and proposed a spectral estimation workflow for chromophore estimation.

A spectral estimation workflow has been implemented for the *SkImager*. The estimated spectral image cube were used to estimate chromophore concentrations. The main objective was hereby a computationally efficient implementation usable for the *SkImager* and with the possibility to operate in real time.

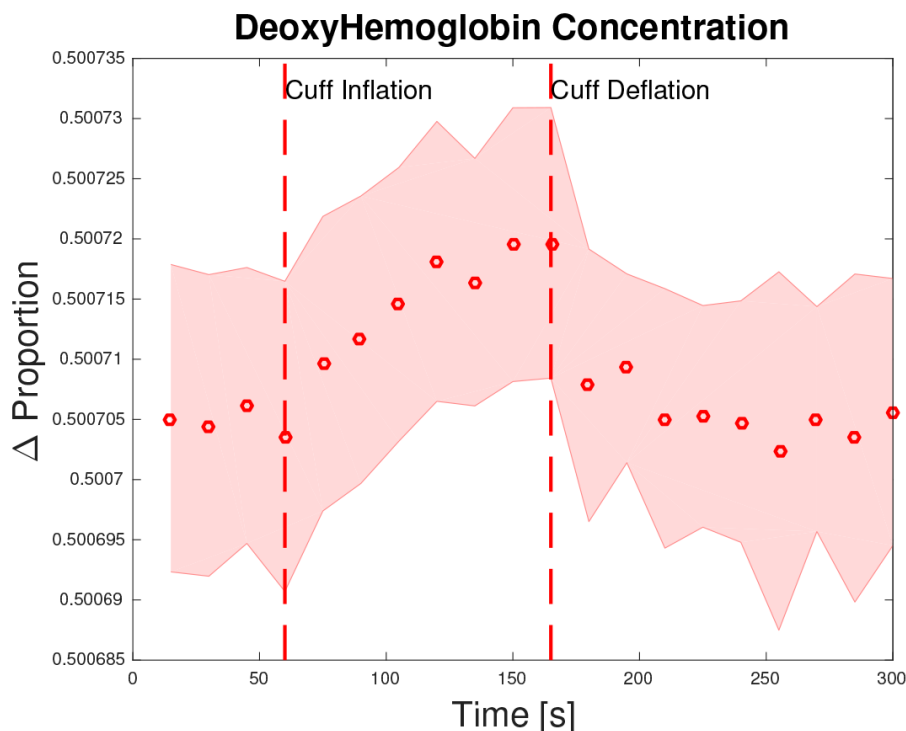


Figure 9. Average deoxygenated hemoglobin concentration of all patients averaged. Expected exponential increase during occlusion

Occlusion experiments were used to verify, chromophore concentration estimation in a realistic experiment. The results indicate that the proposed spectral estimation workflow combined with Monte Carlo simulation provides promising results and leads to expected oxygenation results for the occlusion measurement. Additionally the more general spectral image cubes provides full spectra and could be utilized for more complex analysis of the skin in the future.

Acknowledgment

Part of this work was supported by national funding from the University of Eastern Finland and by the Latvian National Research Program SOPHIS under grant agreement Nr.10-4/VPP-4/11 and the Rhones Alpes scholarship Xplora. Some of the work was conducted in the Biophotonics Laboratory division of the University of Latvia in Riga. I hereby acknowledge everybody at the Biophotonics Laboratory involved in this work and especially Prof. Janis Spigulis and the prior work on the *SkImager*.

REFERENCES

- [1] Spigulis, J., Rubins, U., Kviessis-Kipge, E., and Rubenis, O., "SkImager: a concept device for in-vivo skin assessment by multimodal imaging," *Proceedings of the Estonian Academy of Sciences* **63**(3), 213–220 (2014).

- [2] Jakovels, D., Kuzmina, I., Berzina, A., Valeine, L., and Spigulis, J., “Noncontact monitoring of vascular lesion phototherapy efficiency by RGB multispectral imaging,” *Journal of Biomedical Optics* **18**(12), 126019 (2013).
- [3] Pub, C., “CIE 15: Technical Report: Colorimetry, 3rd edition,” *Vienna, Austria: CIE Central Bureau* **3** (2004).
- [4] Wang, L. H., Jacques, S. L., and Zheng, L. Q., “MCML - Monte-Carlo Modeling of Light Transport in Multilayered Tissues,” *Computer Methods and Programs in Biomedicine* **47**, 131–146 (July 1995).
- [5] Delgado Atencio, J. A., Jacques, S. L., and Montiel, S. V., [*Monte Carlo Modeling of Light Propagation in Neonatal Skin*], InTech (Feb. 2011).
- [6] Imai, F. H. and Berns, R. S., “Spectral estimation using trichromatic digital cameras,” in [*Proceedings of the International Symposium on Multispectral Imaging and Color Reproduction for Digital Archives*], **42** (1999).
- [7] McNamara, P. M., O’Doherty, J., O’Connell, M.-L., Fitzgerald, B. W., Anderson, C. D., Nilsson, G. E., Toll, R., and Leahy, M. J., “Tissue viability (TiVi) imaging: temporal effects of local occlusion studies in the volar forearm,” *Journal of Biophotonics* **3**(1-2), 66–74 (2010).
- [8] Nishidate, I., Maeda, T., Niizeki, K., and Aizu, Y., “Estimation of melanin and hemoglobin using spectral reflectance images reconstructed from a digital rgb image by the wiener estimation method,” *Sensors* **13**(6), 7902–7915 (2013).
- [9] Nishidate, I., Sasaoka, K., Yuasa, T., Niizeki, K., Maeda, T., and Aizu, Y., “Visualizing of skin chromophore concentrations by use of rgb images,” *Optics Letters* **33**(19), 2263–2265 (2008).
- [10] Jakovels, D., Rubins, U., and Spigulis, J., “RGB imaging system for mapping and monitoring of hemoglobin distribution in skin,” in [*SPIE Optical Engineering+ Applications*], Shen, S. S. and Lewis, P. E., eds., 81580R–81580R–6, International Society for Optics and Photonics, International Society for Optics and Photonics (Sept. 2011).

A spectral filter array camera for clinical monitoring and diagnosis: proof of concept for skin oxygenation imaging

Paper C



This chapter is a reprint of the publication:

Jacob R. Bauer; Arnoud A. Bruins; Jon Y. Hardeberg; Rudolf M. Verdaasdonk; “A Spectral Filter Array Camera for Clinical Monitoring and Diagnosis: Proof of Concept for Skin Oxygenation Imaging” *Journal of Imaging* 2019, 5(8), 66.



Article

A Spectral Filter Array Camera for Clinical Monitoring and Diagnosis: Proof of Concept for Skin Oxygenation Imaging

Jacob Renzo Bauer ^{1,*} , Arnoud A. Bruins ² and Jon Yngve Hardeberg ¹ 
and Rudolf M. Verdaasdonk ³

¹ The Norwegian Colour and Visual Computing Laboratory, Norwegian University of Science and Technology (NTNU), 2815 Gjøvik, Norway

² Department of Anesthesiology, VU University Medical Center, 1081 HV Amsterdam, The Netherlands

³ Biomedical Photonics and Imaging Group, Faculty of Science and Technology, University of Twente, 7522 NB Enschede, The Netherlands

* Correspondence: jacob.bauer@ntnu.no

Received: 12 April 2019; Accepted: 20 July 2019; Published: 26 July 2019



Abstract: The emerging technology of spectral filter array (SFA) cameras has great potential for clinical applications, due to its unique capability for real time spectral imaging, at a reasonable cost. This makes such cameras particularly suitable for quantification of dynamic processes such as skin oxygenation. Skin oxygenation measurements are useful for burn wound healing assessment and as an indicator of patient complications in the operating room. Due to their unique design, in which all pixels of the image sensor are equipped with different optical filters, SFA cameras require specific image processing steps to obtain meaningful high quality spectral image data. These steps include spatial rearrangement, SFA interpolations and spectral correction. In this paper the feasibility of a commercially available SFA camera for clinical applications is tested. A suitable general image processing pipeline is proposed. As a ‘proof of concept’ a complete system for spatial dynamic skin oxygenation measurements is developed and evaluated. In a study including 58 volunteers, oxygenation changes during upper arm occlusion were measured with the proposed SFA system and compared with a validated clinical device for localized oxygenation measurements. The comparison of the clinical standard measurements and SFA results show a good correlation for the relative oxygenation changes. This proposed processing pipeline for SFA cameras shows to be effective for relative oxygenation change imaging. It can be implemented in real time and developed further for absolute spatial oxygenation measurements.

Keywords: spectral filter array; multi-spectral imaging; skin; bio-medical optics; occlusion measurement; reflectance spectroscopy; oxygenation; Xispec

1. Introduction

Visual inspection of skin can provide physicians with diagnostic information about the patient. Inflammations, nutrition delivery, oxygenation, blood perfusion and other health indicators can affect the skin tone. In the Operating Room (OR) this information and especially the oxygen delivery is used by anesthesiologists as an early indicator. After light is reflected from the skin, it contains information of physiologic processes within the skin. Cameras can be more sensitive and capable to transfer this information into qualitative or even quantitative data. Analysing the relative changes in color or spectral reflectance over time allows monitoring of physiological processes.

Wieringa et al. [1] demonstrated the feasibility of using RGB cameras for oxygenation measurements analysing the ratio between the individual R, G and B color bands. Van Gastel et al. [2]

extended RGB sensors with high temporal resolution for a camera based pulse oximetry system including a motion artifact resistant method. However, RGB camera sensors have a low spectral resolution with only three wide spectral bands, therefore the applications of monitoring vital functions is limited.

Multispectral imaging, on the other hand, is a technique to measure different narrow spectral bands. This allows a more accurate acquisition of the color or spectral changes in the reflectance of objects spatially. Spectral imaging has been applied in different areas and for different pathologies in the medical field. Some examples are the determination of bruise age [3,4], pigment mapping [5,6], melanoma screening [7] and burn wound analysis [8,9]. These imaging techniques are usually based on a temporal decomposition of the spectral bands with, that is, liquid crystal tuneable filters, filter wheels [10] or monochrome cameras with changing illumination. These techniques acquire different spectral bands at different time instances, therefore they are less suitable for quantifications of dynamic processes like oxygenation of skin. Nevertheless these techniques have been successfully applied to provide a spatially resolved measure of oxygenation [11–13].

Due to recent technological progress in interference filter design, a new multispectral imaging modality acquiring all spectral bands at the same instance has been developed. These spectral filter array (SFA) cameras combine the speed of commonly used RGB imaging systems with spatial and spectral images of the scene. A filter mosaic with multiple specifically selected spectral [14] transmission bands on top of an imaging sensor is the basis for this technology. The filters can for instance be based on Fabry-Pérot interference filters [15], which pass only specific wavelength bands at a given subpixel [16]. The bands can be chosen to provide a good spectral sampling of the scene in real time [17].

Additionally to the adaptation of these sensors in academia [18–24] some commercially available products have been developed by PIXELTEQ [25], SILIOS Technologies [26] and IMEC [27]. Acquisition speed, ease of use and versatile spectral range makes SFA cameras interesting for the medical sector, especially for the quantification of dynamic processes [28]. Filter wheel cameras or LCTF cameras on the one hand sample the spectral bands temporally SFA cameras, on the other hand sample the spectral information spatially. These spatially arranged filter sensitivities often come with a cost regarding the spectral sensitivities. Unlike the temporal spectral imaging systems, which have very narrowband filter sensitivities, some commercially available SFA imagers have double lobes in the spectral sensitivities. This unique architecture makes specific processing steps, like spatial decomposition, spectral calibration and the careful choice of optimal exposure necessary [15,20,24,29,30]. These can cause practical hurdles for clinical implementations of SFA imaging systems.

Oxygenation of tissue is a dynamic process and spatial oxygenation measurements in real time are of clinical value [31]. Temporal and spatial color changes can be used to provide indication of the micro-circulation of skin and oxygen distribution to tissue. The oxygenation of skin varies over its surface area as shown in previous studies [32] and therefore, spatial analysis is advantageous.

In this study the processing steps needed to make an SFA camera setup suitable for medical applications are developed and tested. A transferable basic processing pipeline for SFA cameras in the context of skin imaging is proposed. The focus is to maintain the full spectral range, ease of use of the imaging setup and the acquisition speed provided by this new technology. The proposed processing maintains the temporal, spectral and spatial attributes of SFA imaging systems, while solving technical hurdles introduced with this technology. A proof of concept on dynamic oxygenation distributions in volunteers using the spectra obtained with the SFA camera is conducted. The results are compared to a clinically validated device (gold standard) for oxygenation measurements and show relatively good sensitivity for oxygenation measurements.

2. Theoretical Background

Key aspects to consider for the acquisition of multispectral images are presented in Figure 1. Most important aspects include the unique power distribution of the light source, the camera

parameters for acquisition, pre-processing steps and finally the processing of the sensor data or the spectral image cube. The spectral image cube is the final output of most spectral imagers and each slice of the cube is an image sensed with a particular wavelength. A pixel in the plane of the spectral image cube represents the spectrum in that particular location. Table 1 shows advantages and disadvantages of different spectral imaging approaches [20].

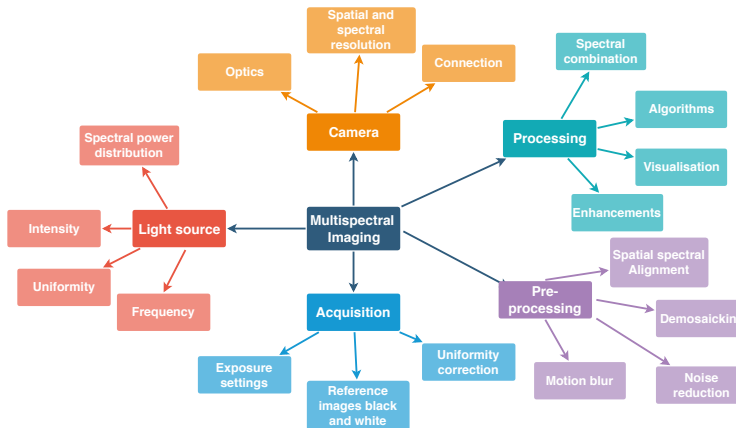


Figure 1. Overview of key aspects for generic spectral image acquisition including the camera, light source, acquisition, pre-processing steps and processing steps for the spectral image. For SFA imaging temporal aspects are of special importance: the flicker frequency of the light source and the connection speed to the camera. All of the items shown in this diagram have to be addressed for successful spectral image acquisition and meaningful data processing.

Table 1. Overview of spectral imaging techniques including RGB [33], filter wheel cameras (FW), liquid crystal tunable filter (LCTF) cameras, spectroscopy [34] (Spec), spatial frequency domain imaging (SFDI) [31,35–37], multispectral illumination (MI) [1,38], SFA spectral filter array [39].

Property	RGB	FW	LCTF	Spec	SFDI	MI	SFA
spatial acquisition	2D	2D	2D	point	2D	2D	2D
spectral bands	3	8–10	100	$x > 100$	$x > 100$	~ 20	8–16
spectral acquisition	snapshot	sequential	sequential	snapshot	sequential	sequential	snapshot
frame rate	~ 150 fps	~ 60 fps	$\sim 1 \div 0.05$ s	~ 1 fps	~ 60 fps	$\sim 1 \div 0.05$ s	~ 30 fps
cost	low	medium	medium	low	medium	medium	medium
Processing complexity	low	low	medium	low	medium	medium	medium
effort of use	low	medium	medium	low	medium	medium	low

SFA implementations provide a good tradeoff between true simultaneous snapshot capture of all wavelength, higher number of spectral bands, medium costs, ease of use and acquisition speed in terms of frames per seconds (fps).

Several processing steps are needed to obtain the spectral cube from an SFA image, while maintaining all of the benefits mentioned.

2.1. Light Skin Interactions

Skin color contains physiologically relevant information and optical or visual inspection of skin is a commonly used method in the medical practice. The perceived color of skin is the resultant of a complex combination of absorption and scattering events during the path of light traveling through the skin. A longer path length increases the probability of absorption events and the path length itself depends predominately on scattering properties of the tissue [40]. Besides absorbers or chromophores which are spatially and temporally invariant, other chromophores can change

dynamically influenced by physiological processes resulting in slight variations in the color of skin [41]. Melanin, hemoglobin [42] (p. 11) and its derivatives are the most common chromophores in the skin. The perceived color of skin depends on the distribution, concentration and depth of these chromophores. Figure 2 shows a simplified 3-layer model of light-interaction in the various layers of skin. Various layers, like epidermis, dermis and subcutaneous tissue, have different properties regarding scattering and absorption parameters.

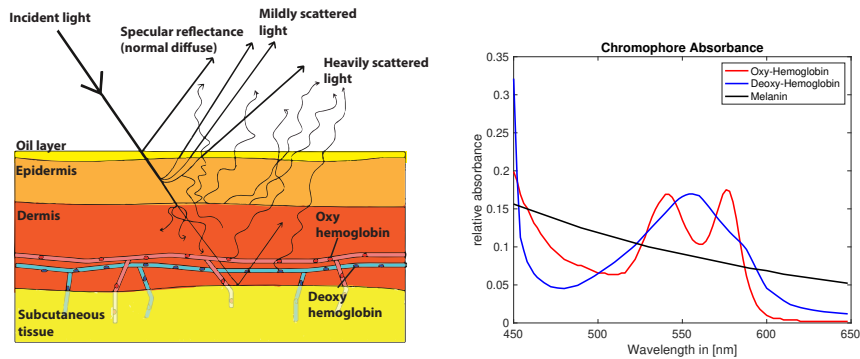


Figure 2. Skin light interaction simplified model (left) [43]. Absorption of common chromophores in the visual range of the light spectrum (right) (data compiled from [44], Figure recreated from [43]).

Melanin is expected to occur mainly in the epidermis, whereas hemoglobin is predominately found in the dermis layer. The lowest layer subcutaneous tissue optically functions as a reflector of the light that reaches these depths. The spectral absorption of hemoglobin, which is a dominant chromophore in red blood cells, depends on the oxygen levels bound to the hemoglobin molecule [45] (Figure 2). The color of skin is affected by the slight differences in absorption in oxy and deoxygenated hemoglobin and could potentially be measured with optical techniques in non contact.

2.2. Characteristics of SFA Cameras

Digital color cameras utilize color filter arrays in broad red, green and blue ranges of the spectrum, commonly referred to as RGB. A 2×2 pixel array mosaic covers a large megapixel sensor containing small red, green and blue filters. Through image processing and demosaicking algorithms a full color image is reconstructed. In case of spectral filter array (SFA) sensors this method is scaled up to larger pixel arrays [15,29] with narrow band filters covering specific spectral bands in the visible (400–650 nm) or the near infrared (650–900 nm range). An example of this is illustrated in Figure 3 showing the peak wavelength and filter mosaic of the commercially available camera used in this study (IMEC [27], XIMEA [46]).

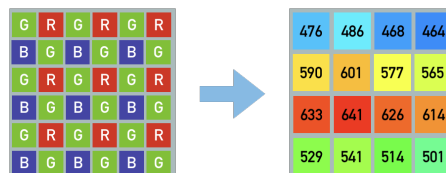


Figure 3. Illustration of common Bayer pattern RGB mosaic and spectral filter array with 16 different peak wavelengths [nm] equally distributed over the whole sensor. The indicated spectral sensitivity peaks show the sensor implementation available for this study.

In principle these spectrally sensitive filters can be arranged specifically and various different patterns have been proposed. Demosaicking algorithms allow the reconstruction of a full spectral image cube [15,29,30].

SFA spectral imaging unlike conventional spectral imaging allows to simultaneously acquire all wavelengths at the same time in a snapshot fashion at typical video rates (20–50 fps) [16]. These spectral images enable discrimination of physiological markers in high speed, which have potential for medical diagnostics. However, the selected wavelengths of the SFA filters can be sub-optimal for wavelength of interest in medical diagnostics. Also the filtering might ‘leak’ an additional secondary wavelength, complicating the analysis.

Fabry-Pérot filters have two highly reflective coatings on the surfaces of a substrate. The distance between these reflective surfaces is ‘the cavity’. Depending on the thickness of this cavity the transmission through the coatings changes and only a specific wavelength passes to the sensor. SFA filter technology introduces crosstalk of adjacent channels, second order responses and spectral leaking [20,24].

Spectral leaking describes the limitation of reflective surfaces that are only defined in an active spectral region. It can be accounted for by limiting the active range using a band-pass filter mounted on the spectral filter array.

Crosstalk describes the influence of one pixels signal onto a neighboring pixels signal. This especially effects SFA sensors, due to their high spatial variation of filter sensitivities.

Second order harmonics are an inherent hardware limitation of Fabry-Pérot SFAs, due to the spectral filter design. The thickness of the cavity defines the peak wavelength for transmission based on constructive interference of the light trapped in the cavity. But the constructive interference occurs for all light in phase and depends on the wavelength, the angle of light, the thickness of the cavity and the refractive index of the material between the surfaces. Due to the nature of these filters second order peaks also interfere constructively and are therefore transmitted, making the filters sensitive to two wavelength peaks. Some of these additional peaks are filtered out through limiting the active region with a bandpass filter but some of the second order peaks need to be corrected for.

Next to hardware solutions, crosstalk and second order responses can be corrected numerically as a post processing step.

SFA imaging technology requires hardware-aware processing [24,30] both spatially and spectrally to rearrange the pixels of particular spectral sensitivity into an ordered spectral image cube. There are various processing techniques discussed in literature. According to Lapray et al. [20] the filter arrangement should be interconnected with the optimal processing or demosaicking approach in order to obtain the best signal from these kind of sensors. Sadeghipoor et al. [47] propose a spectral demultiplexing of visible and near infrared overlapping spectral information by using spatial and spectral correlation of the channels. This limitation could also be addressed by adding a specific color restoration step into the processing chain as proposed by Park and Kung [48]. These examples of spectral filter array processing discuss different approaches for using SFA data and illustrate the necessity of hardware-aware processing.

2.3. Oxygenation Physiology

Oxygenation as a systematic parameter is measured with so called (pulse) oximetry systems [34,49]. Two modes are used clinically, the transmission mode and the reflectance mode. Both modes measure the detected light, which has been altered due to absorption in the tissue. These absorptions depend on physiological properties of the tissue Pulse oximetry measures tissue oxygen saturation as a systematic parameter in one particular spot Non pulsatile oximeters allow the measurement of location based differences. But both are limited to a small measurement area and do not indicate spatial differences of tissue oxygenation.

The well documented [28,31,33] occlusion test behaves as illustrated in Figure 4. A decrease of oxygen concentration during occlusion can be expected followed by a sharp incline with an overshoot

of oxygen concentration just after the moment of cuff deflation and followed by a slow return to baseline after the overshoot of oxygen concentration.

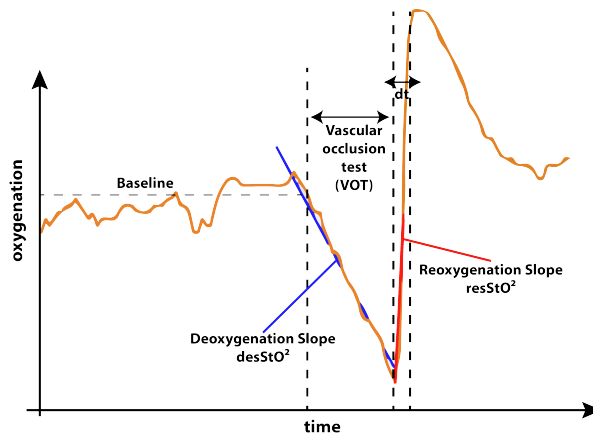


Figure 4. Expected behavior of oxygenation during the occlusion experiment. As described by Futier et al. [50] in the not occluded phase of the experiment a stable baseline with minor fluctuations is expected. As soon as the blood flow is occluded during the vascular occlusion test (VOT), the oxygenation decreases following a deoxygenation slope. As soon as the cuff is released the reoxygenation with an overshoot of oxygenation occurs. The slope providing a way of quantification of the reoxygenation. The time from cuff release to the reoxygenation overshoot peak is quantified as dt . After this the oxygenation curve returns back to baseline.

For physicians, the characteristics of this oxygenation curve can be correlated to the health status of vasculature of the patient. Influences of anesthesia on these key features of the occlusion test were studied by Bernet et al. [51] and they report that anesthesia have an impact compared to a healthy control group. Lipcsey et al. [52] report indications that NIRS measurements of these parameters can provide information about fluid responsiveness of patients and predict surgical complication and reactions to anesthesia. Abelmalak et al. [53] correlate preoperative values for the discussed parameters with serious post operative complications.

3. Methods

3.1. Data Acquisition and Processing

The process to obtain a spectral image cube with conventional spectral imaging systems is obvious. Multiple narrowband spectral captures are performed and concatenated to obtain a spectral image cube. Black and white corrections are included in order to account for the scene illumination and spatial differences of the illumination.

SFA cameras, however, need to be processed spatially and spectrally in order to obtain a spectral image cube. For this study a commercially available SFA camera-based on the IMEC [27] snapshot sensor, the XIMEA *XiSpec SM4x4 VIS* [46] operating in the visual range from 470 nm to 630 nm with 16 channels was used.

The acquisition of images was performed with the “*XiCamtool*” tool version 4.7 by XIMEA [46] with settings for frame rate, exposure time (described in Table 2) and the *raw* (.tiff) file format in sequences. All acquisitions were performed with a constant exposure time (50 ms) chosen to stay within the 66% saturation, where linearity of the sensor is guaranteed by the manufacturer [27]. No further linearization or inverse camera response function was applied and this study does not include a measurement of linearity of the camera. A dark reference $I_{Dn}(x,y)$ image and a white reference $I_{Wn}(x,y)$ image were taken with the same optical setup. For the ‘white’ reference a grey

diffuse reflectance standard (Spectralon SRT-20-100 20%, 10 × 10 inches) was used. The reflectance standard was chosen to be grey rather than white to avoid over saturation for any wavelength compared to the measured skin and in order to stay within the dynamic range of the camera which covers 16 wavelength bands with non-uniform sensitivities.

Table 2. Camera parameters chosen for the acquisition.

Camera Property	Value
Acquisition speed	1 fps
Exposure time	50 ms
Aperture	2.8 f
Lense	Edmund Optics 35 mm C Series VIS-NIR

An illumination corrected image $I_n(x, y)$ can be obtained using this method. Each of the sample images was therefore given by:

$$I_n(x, y) = \frac{I_{Sn}(x, y) - I_{Dn}(x, y)}{I_{Wn}(x, y) - I_{Dn}(x, y)} \tag{1}$$

This process followed the recommendations by McCann [54] for using diffuse reflectance standards to account for the spectral power distribution and inhomogeneities of the illumination. Previous test measurements of a *Gretag MacBeth* color chart have shown that this flat field correction combined with the spectral correction allows adequate reconstructions of spectral reflectances. The acquisition speed of one fps was chosen in order to exceed the acquisition speed of the INVOS system with one frame every three to four seconds, while at the same time ensuring the reliable recording of the data via USB three connection. Disk space for the consecutive measurements was limited. Reducing the amount of data created per measurement was therefore necessary. This relatively slow acquisition speed (for an SFA camera) is fast enough for this type of oxygenation measurements and three times faster then the reference measurements.

The 1088 × 2018 full frame images consisting of 4 × 4 repeated multispectral grids have to be spatially separated into single spectral channels. This is reducing the spatial resolution to 1/4 resulting in 16 spectrally separated 272 × 512 pixel images in .tiff format that can be converted to .ids video sequence files. These processing steps are incorporated in a custom made program called “Multispec” [55,56] not part of the contribution of this research.

3.2. Spectral Correction

The sensitivities of the SFA camera used in this study have significant second order peaks and are overlapping (cross talk) for which a mathematical spectral correction of the data is necessary.

A spectral correction matrix specific for the camera used in this study was supplied by the sensor manufacturer (IMEC [27]). The correction is based on detailed spectral measurements of each specific filter in front of the pixels as shown in Figure 5. These were measured in a monochromator setup by the manufacturer [27] and provided as data together with the camera. They characterize the imperfections of each specific filter.

The spectral correction is intended to minimize the ‘imperfections’ but is not optimized for a specific application. In this research the calibration matrix provided by the manufacturer was used. A calibration matrix can be determined using defined spectral reflectances in form of *Gretag MacBeth* color chart spanning a wide range of different spectral shapes. Essentially this spectral correction is a linear transformation of the cameras imperfect broad sensitivities including second order peaks to idealized virtual narrow band sensitivities. It can be described as a linear transformation and the theory and assumptions were previously described by Connah et al. [57]. Generally the camera response per channel P_i is described with reflectance R (of any object) under illuminant E and channel specific sensitivities Q_i and system specific noise n with the equation:

$$P_i = \int_{\lambda} Q_i(\lambda)E(\lambda)R(\lambda)d\lambda + n \tag{2}$$

The previously described illumination correction allows to simplify the equation. After correction for illumination and assuming continuous functions of wavelength sampled at discrete intervals (i.e., 31 measurements) this can be reformulated in matrix form to:

$$p = Q_e^T r + n \tag{3}$$

The recovered reflectance is described as a spectrum through a given camera response p . Q_e describes the effective sensor sensitivities. Assuming smooth curves, reflectances r can be approximated with the linear combination of a number of basis functions and weighting factors [57],

$$r \approx Bw, \tag{4}$$

where B is the matrix $31 \times m$ with m different basic functions or number of channels. w describes the weights assigned to each of these basic functions in order to approximate r best. Then the response p is:

$$p \approx Q_e^T Bw + n, \tag{5}$$

For given reflectances the weights w and the basis functions B can be determined and the error between the known spectrum and the approximated spectrum minimized. These are calculated as a preprocessing step for known color checker reflectances. This correction is not particularly tuned for skin imaging and can be considered a preprocessing step necessary for this SFA implementation. A pair of known reflectance and its corresponding camera responses are used to minimize the projection from spectral to camera space. The correction matrix similar to the correction matrix provided by the manufacturer [27] is obtained and can be used for correction via a matrix dot product with each measured camera response in order to reconstruct a corrected spectrum. This preprocessing step provides the estimated spectral data and is the final input for the oxygenation estimation.

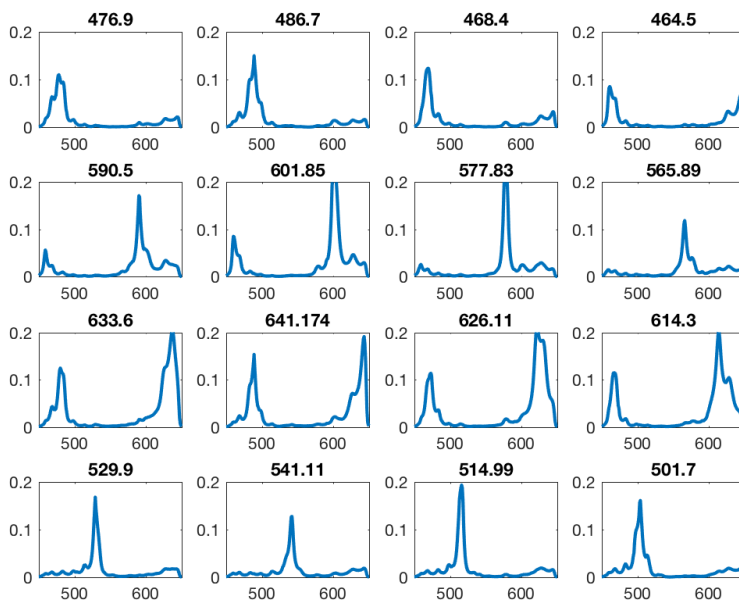


Figure 5. All filter sensitivity multiplied by the bandpass. Many filters show a second order peak inside the sensitive area. Intended peak wavelength shown above of each filter sensitivity curve.

Figure 6 illustrates the effect of this correction, it was applied to one of the filter responses. This illustrates how the spectral correction matrix corrects for the second order peaks and spectral crosstalk.

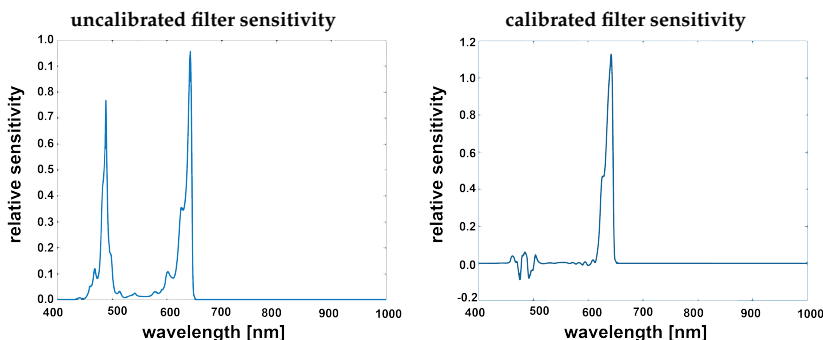


Figure 6. Filter sensitivity given by manufacturer [27] from the calibration file (left) filter band-passed showing clear second order harmonics, corrected filter after applying the spectral correction (right).

The spectral correction transforms from the camera responses to a reflectance image cube and reduces the number of channels from 16 to 10 effective virtual channels, which is similar to the basis functions described by Connah et al. [57]. The correction matrix provided by the manufacturer [27] indicates that the crosstalk in the 600+ nm channels is too severe to use them or reconstruct them numerically. A custom reconstruction matrix could be calculated and estimate results for these bands as described. The resulting spectral image cube with 10 specific bands can then be used for further processing and analysis. This processing step is integrated into the proposed processing chain and an overview is provided in Figure 7. All of these bands can be used depending on the medical application and the specific bands of interest.

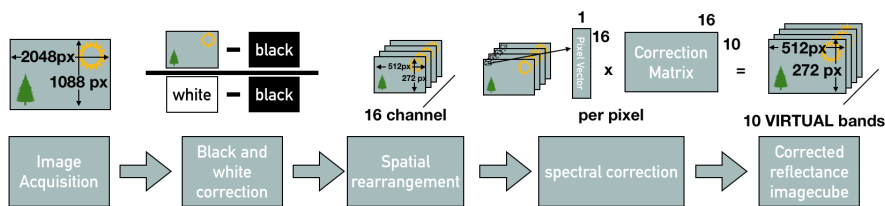


Figure 7. Overview of the processing chain: Image acquisition of the full frame image with the spatial spectral mosaic, full frame black and ‘white’ correction, spatial rearrangement of the channels, spectral correction resulting in the reflectance image cube.

3.3. Oxygenation Estimation from a Multispectral Image Cube

As described above the SFA camera enables spectral images in 10 narrow wavelength bands of the scene after correction. To estimate oxygenation from these spectral images, the previously proposed method called the Δt method [58–60] was applied. This method has been chosen due to low computational complexity and in order to enable real time estimation of oxygenation of the tissue in the future. And furthermore since it is the most commonly used technique for fNIR spectroscopy, used for oximetry systems. This allows to maintain a high degree of comparability between the INVOSTM oximetry reference system and the SFA camera test system.

In its current implementation this method utilises only three key wavelength chosen based on their descriptive nature of the absorption spectrum of oxy and deoxygenated hemoglobin. Other wavelength imaged with the SFA setup are not utilized for the application of oxygen estimation in the current implementation.

The Δt method is based on the modified Beer-Lambert law and considers absorption and scattering as the main reasons for the attenuation of light in tissue. The method assumes that the absorption can be separated in two parts: (1) a time invariable constant absorption due to chromophores present in the skin and (2) a time variant absorption due to changing oxy and deoxygenation in the skin. These depend both on the oxygen concentration and the total blood volume present during measurement. Optical density or absorption can be defined as,

$$OD = -\log_{10}\left(\frac{I}{I_0}\right) = \sum_n \epsilon_n * c_n * d; \tag{6}$$

where OD stands for optical density, I_0 is the emitted light intensity and I is the intensity of the received light, ϵ describes the molar extinction coefficient for n different chromophores, c is the concentration of the chromophore n and d the path length taken by the light. The modified Beer-Lambert law can describe the longer path-length of light through the medium, due to scattering [61] as,

$$\overline{A(\lambda)} = \overline{\epsilon(\lambda)} * \overline{c(t)} * \overline{DPF(\lambda)} * d + \overline{G(\lambda)} + \overline{H(t)}; \tag{7}$$

where $\overline{A(\lambda)}$ is the absorbance, $\overline{\epsilon(\lambda)}$ describes the molar extinction coefficient [$\text{mM}^{-1} \text{cm}^{-1}$], $\overline{c(t)}$ is the concentration of a specific chromophore [mM], $\overline{DPF(\lambda)}$ differential path length factor corrects the geometrical source-detector distance to the mean optical path in the tissue, d the source detector distance [cm] and $\overline{G(\lambda)}$ and $\overline{H(t)}$ are both oxygen independent loss factors accounting for scattering, absorption and geometry losses where $\overline{H(t)}$ is time dependent and $\overline{G(\lambda)}$ is wavelength dependent.

This can be rewritten in matrix form and with three specific wavelengths to:

$$\begin{bmatrix} A(\lambda_1, t) \\ A(\lambda_2, t) \\ A(\lambda_3, t) \end{bmatrix} = \begin{bmatrix} \epsilon_{O_2Hb}(\lambda_1)DPF(\lambda_1) & \epsilon_{HHb}(\lambda_1)DPF(\lambda_1) \\ \epsilon_{O_2Hb}(\lambda_2)DPF(\lambda_2) & \epsilon_{HHb}(\lambda_2)DPF(\lambda_2) \\ \epsilon_{O_2Hb}(\lambda_3)DPF(\lambda_3) & \epsilon_{HHb}(\lambda_3)DPF(\lambda_3) \end{bmatrix} * \begin{bmatrix} c_{O_2Hb}(t) \\ c_{HHb}(t) \end{bmatrix} d + \begin{bmatrix} G(\lambda_1) \\ G(\lambda_2) \\ G(\lambda_3) \end{bmatrix} + \begin{bmatrix} H(t) \\ H(t) \\ H(t) \end{bmatrix} \tag{8}$$

The Factor G is accounting for geometry losses and due to the fact that the measurement geometry is kept constant it can be assumed that G stays constant throughout the measurement. The H term can be considered zero or constant in time, since no significant changes in the optical properties of the skin are to be expected in the timespan of this experiment. ϵ_{O_2Hb} and ϵ_{HHb} describe the unique absorbances of the oxygenated hemoglobin and deoxygenated hemoglobin.

The difference in oxygen concentration at a time point (Δt) relative to a stable starting point can be calculated by simplifying the equation to:

$$\Delta_t \bar{c} = \frac{\overline{\epsilon DPF}^{-1} \Delta_t \bar{A}}{d} \tag{9}$$

The equation contains $\overline{DPF(\lambda)}$ values from literature for the specific interrogated tissue. This formula allows to relate changes in light intensity of particular wavelength to changes in oxy, deoxygenated hemoglobin concentrations. The average of the first few frames of the measurement are used to estimate the time invariant contributions to the measured skin reflectance spectrum. Changes of the skin spectrum especially in the areas of highest absorption differences between oxy, deoxygenated hemoglobin are calculated. This oxygen concentration estimation can be applied using three wavelength (515 nm, 565 nm and 601 nm) from the reflectance image cubes previously obtained with the SFA camera and the process is illustrated in Figure 8.

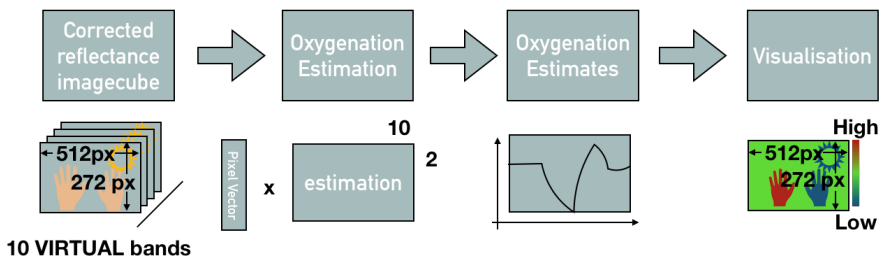


Figure 8. Oxygenation estimation from spectral reflectance cube.

These three wavelengths are specifically chosen, based on the spectral absorption peaks and differences in absorption of oxygenated and deoxygenated hemoglobin. They contain descriptors of the oxygenation with a small difference at 515 nm and large differences at 565 nm and 601 nm in absorption between two oxygenation states of hemoglobin. The small difference point provides a reference (isosbestic point in the visual range), while the points of large difference provide good estimators [28]. Even though the estimation is performed for the entire image only an average of the estimated oxygenation in the marked region of interest as shown in Figure 9 (green circle) was collected. The resulting oxygenation and estimated oxygenation curves from the INVOS and the multispectral system were marked by collaborating physicians for the moment of pressure release in the curves of both measurement devices. Since the SFA based oxygenation estimates are of relative unit of small scale a feature scaling normalization had to be applied to both curves:

$$X' = \frac{X - X_{min}}{X_{max} - X_{min}}; \tag{10}$$

After normalization both curves are in the value range of [0, 1] allowing comparison between the curves. This feature scaling affects the amplitude of the oxygenation signals and favors the comparability between the two curves. Nevertheless this processing step is necessary to compare the shapes and oxygenation behavior measure with both devices. As another processing step the curves are aligned along the time axis using the markers for cuff release as the minimum point of both curves.

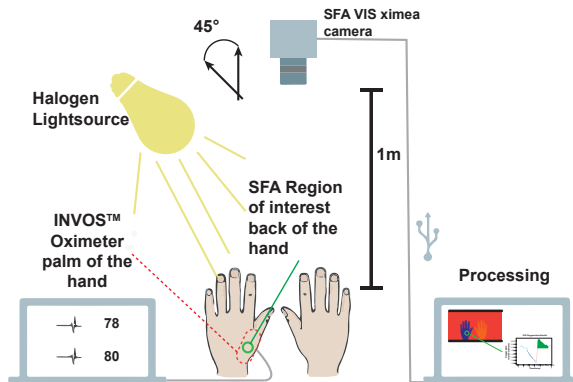


Figure 9. Experimental setup. XIMEA [46] camera 1m above volunteers hands. 45° (following the CIE recommendation [62] and ([45] p. 144)) between halogen lightsource and SFA camera. Parallel measurement at the palm of the hand with the INVOS. SFA measures at the back of the hand with green circle indicating region of interest for averaging. External processing on a computer (adapted from Reference [39]).

The oximeter samples the oxygenation significantly slower, with only one measurement every three to four seconds compared to the SFA setup with 1 frame per second. Therefore, a moving average of three values for the SFA oxygenation estimates was taken in order to resemble the sample rate of the INVOS oximeter better. These steps and the following data analysis and visualization was performed using custom written *python* code.

3.4. Proof of Concept Oxygenation Study

For proof of concept an in vivo study was performed on human volunteers. Both the proposed SFA setup and the clinical reference (gold standard) were used. The well documented upper arm occlusion [28,31,33] test was chosen for comparison. The SFA camera XIMEA™ [46] *XiSpec SM4x4 VIS* was used.

An inflatable cuff was used on one of the arms of a volunteer. The arm is clamped for approximately three minutes decreasing the blood-flow significantly resulting in a decrease of oxygenation by around 60%. The standard oxygenation measurement is performed with a sensor taped on the skin emitting two wavelengths and sensing the ratio of the reflected light. An overview of the experimental setup is provided in Figure 9.

The camera was placed in 1 m distance from the hands of the volunteers. Skin can be considered a rough surface and contains an oily layer. The skin of the hands was illuminated under an angle of 45° in order to minimize the specular reflection from the tissue surface. The camera sensor plane was parallel (0°) to the upper side of the hands. This way a 0/45° experimental setup following the CIE recommendation [62] for color measurements and the practice for white light spectroscopy in the medical field [45] (p. 144) were followed.

The INVOS “Cerebral/Somatic Oximetry Adult Sensor” was positioned on the palm of the hand out of view for the camera. By the region of interest (ROI) for the SFA oxygenation measurement was chosen close to the position of the INVOS sensor.

All 58 volunteers had no reported previous condition or vascular diseases and were in the age group of 18–65 years old. The experiment was approved by the Medical Ethics Committee of the VU University Medical Center (METc-16.315). Written informed consent was obtained from all 58 volunteers prior to participation.

The baseline blood pressure and temperature of the volunteers were measured prior to the experiment. An inflatable cuff was placed around the left upper arm and inflated to 30 mmHg above the previously measured systolic blood pressure. The cuff was kept inflated until the reading of the INVOS™ NIRS system dropped to 40% of baseline oxygen saturation following the protocol described by Meyer et al. [63]. As soon as this value was reached the cuff was immediately deflated and the blood perfusion in the arm and hand were restored.

Both the moment when the occlusion started and the moment when the occlusion was stopped were marked manually for both measuring systems in order to later align the time axis adequately. The aligning and calculation of the parameters was based on numerically determined extreme points of lowest detected oxygen saturation and highest detected saturation and the baseline labelled by physicians involved in the study. The highest detected oxygen saturation was only determined in a window where the curve was considered to return to the baseline, this window was also determined by the physicians. For the SFA measurement a reflective marker was added to the scene and removed at the moment the pressure cuff was released. During the occlusion protocol SFA images were acquired continuously.

4. Results and Discussion

4.1. Spectral Correction and Spatial Down Sampling

An overview of the complete processing chain for SFA imaging is provided in Figure 7 including processing steps for calibration, corrections and analysis. This processing allows to reconstruct the full spectral cube from SFA images. They provide a selection of 10 narrow band wavelength regions that can be used for clinical monitoring and diagnostics.

For validation the *Gretag MacBeth* color chart was imaged with a reference spectral camera (SPECIM IQ) and the SFA imaging setup. Figure 10 shows the resulting reflectances of the color chart before and after spectral correction. This illustrates the improved fit with the reference after correction and emphasizes the usefulness of the spectral reconstruction. After correction ten spectral bands are available, a selection can be used containing the relevant pathological or physiologic information.

The spectral correction could be optimized by including prior knowledge about the expected spectra imaged by the SFA system. A dynamic spectral correction could be implemented to provide a better spectral reconstruction. The careful selection of adequate training data more specialized to the skin application might provide better spectral reconstructions of these skin spectra. This would allow the matrix to emphasize subtle changes of skin reflectance. An optimal set of spectral bands for a given application can be determined and implemented in the correction matrix. For oxygenation measurements, a custom built spectral camera only sensitive in three narrow wavelengths bands could improve the applicability. Optimizing the number and distribution of channels numerically could further improve the results.

The straightforward spatial demosaicking reduces the spatial information significantly. In this research the spatial resolution was not further utilized and was not a priority. For applications that need better spatial resolution more advanced techniques to reconstruct missing spatial information exist. These techniques utilize the spatial redundancy as shown in other studies [15,20,29,30].

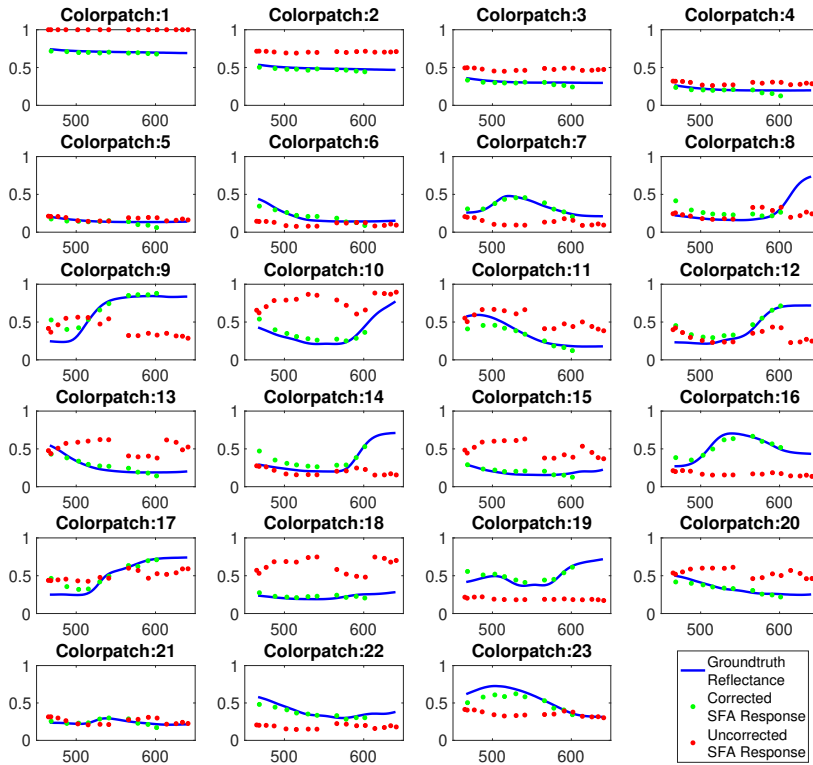


Figure 10. Spectral reflectance of Gretag MacBeth color patches measured by full spectral camera (blue), uncorrected spectral estimates of SFA setup (red), spectral corrected estimates (green).

4.2. Proof of Concept Oxygenation Study

Figure 11 illustrates the color maps at three different stages of the occlusion protocol that are generated using the SFA data collected. Spatial differences along the surface of the hand are visible, blue indicating low oxygenation and red indicating higher oxygenation. The right hand is shown as a reference for validation of the measurement and is not occluded. The clinical reference INVOS 5100C-PA provides a local measurements on the palm of the hand, opposite to the region of interest for the SFA system (indicated with a green circle).

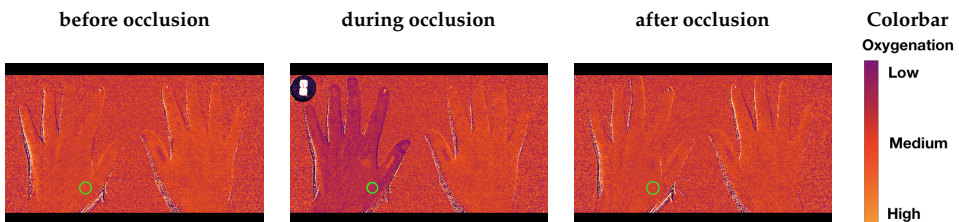


Figure 11. Colormaps of the three different stages of the occlusion before the occlusion (left), during the occlusion shortly before the deflation of the cuff (middle), reperfusion after the cuff is released (right). Green circle indicating the averaged region of interest for oxygenation curves.

In order to compare the shapes of the oxygenation curves root mean square error (RMSE) and goodness of fit coefficients (GFC) were calculated. These compare the general shape of the two

curves and provide a metric for their agreement or similarity according to their shapes. In Figure 12 representative normalized oxygenation curves with lowest root mean square error and best goodness of fit coefficients and the respectively lowest performing examples according to these two metrics.

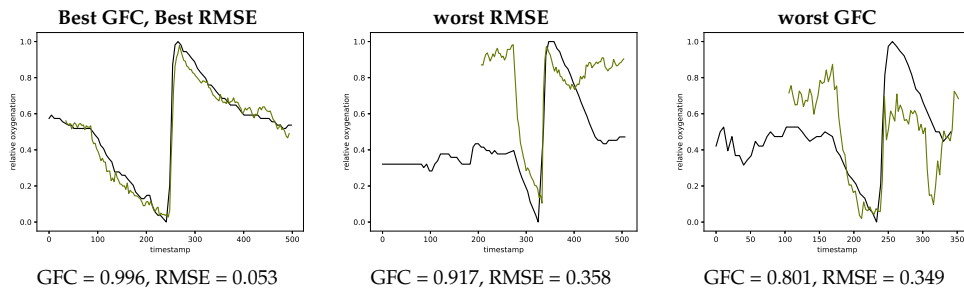


Figure 12. Extreme curves with best GFC and best RMSE (left, #V56-1) worst RMSE (middle, #V07-1) and worst GFC (right, #V39-1) metrics. INVOS measurement in black and SFA estimation in green.

Figure 13 contains three representative plots illustrating the impact of different aspects in the proposed processing pipeline. The top row illustrates the impact of the spectral correction step for two example volunteers. In both cases it can be observed that the agreement between ground truth measurement (black) and estimated oxygenation improves with the spectral correction. For volunteer one (left) RMSE improves by 0.73 and GFC by 0.28 for the second volunteer (right) the changes are GFC = 0.14 and RMSE = 0.59.

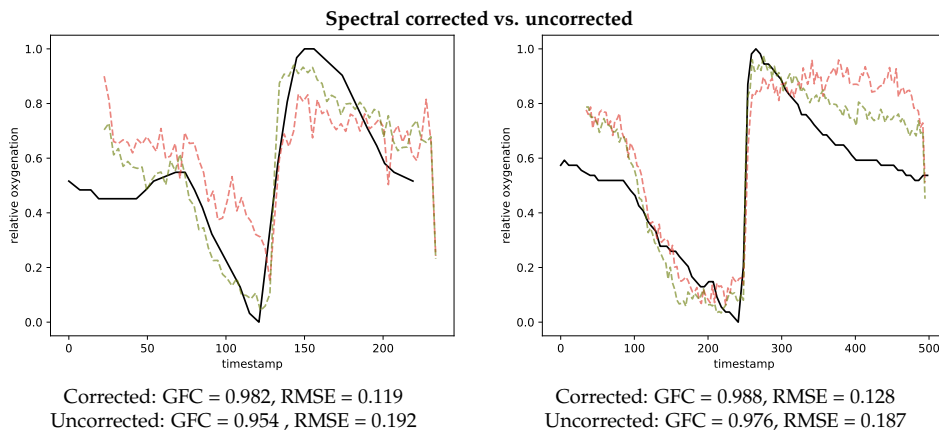


Figure 13. Two representative curves (left, #V03-1) (right, #V56-1) comparing spectral correction (green) and spectral uncorrected (red) oxygenation estimations in comparison to the INVOS measurement (black).

Figure 14 also provides examples showing the difference of using three chosen wavelength (left) compared to all wavelength (right) for estimating the oxygenation curves. The metrics GFC and RMSE both result in a smaller agreement with the gold standard INVOS measurement devices, when using all wavelength.

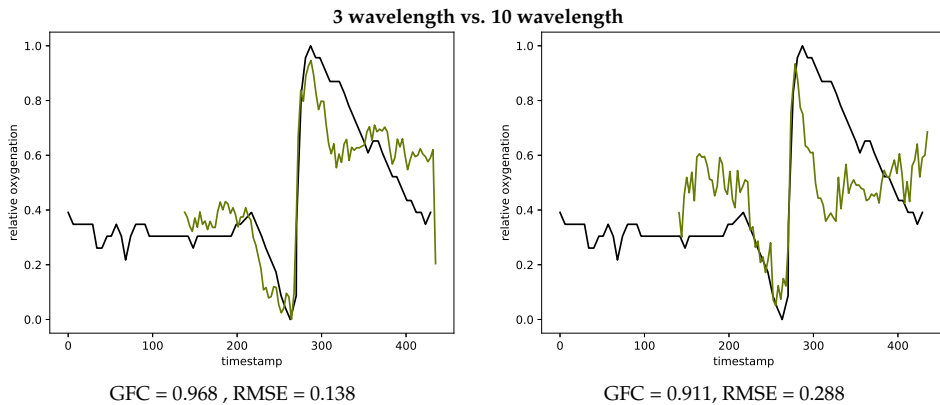


Figure 14. Oxygenation curves calculated with the three chosen wavelength (left, #V27-2) and using all wavelength (right, #V27-2) in comparison with the INVOS measurements

Table 3 presents the statistical data for all measurements on the volunteers.

Considering the GFC and RMSE metrics there is an acceptable agreement with an average GFC of 0.965 and 0.185 for RMSE, the SFA imaging technique shows to be promising for spatial oxygenation measurements.

Table 3. Minimum, maximum, average, standard deviation and 95 percentile values for both root mean square error and goodness of fit coefficient. Small root mean square error corresponds to desired value and close to one corresponds to a desired goodness of fit coefficient value.

	Min	Max	Avg	Med	Std	95%
RMSE	0.053	0.358	0.185	0.173	0.064	0.099
GFC	0.801	0.996	0.965	0.973	0.030	0.912

The de- and re-saturation slopes are parameters of interest for a preoperative or anesthesiological context. These slopes were determined from the saturation curves using linear fitting, the de-saturation slope in blue and re-saturation slope in red, this is illustrated in Figure 15 for both the INVOS system and the SFA setup.

In Figure 16 the calculated de- and re-saturation slopes from the reference system compared to the SFA setup are presented for all measurement showing a sample (Pearson) correlation coefficient of 0.750 for de-saturation and 0.276 for re-saturation.

The significantly lower correlation for the re-saturation slope might be ascribed to the method of analysis. The begin and end point of the steep re-saturation slope were determined numerically as the minimum and maximum in a manually defined area. A small shift in the position of these points results in a larger variation between measurement devices.

The difference in measurement technique between the INVOS system and the proposed SFA system need to be considered. The INVOS provides absolute oxygenation measurements in contrast to the oxygenation related relative estimates from the SFA setup. These estimates are closely related to oxygenation as shown in Figure 15 but may be influenced by other physiological effects in addition. One of these effects could be blood volume, which might not be adequately accounted for. As mentioned in Section 3.3 the SFA oxygenation estimation utilizes the first frames to account for time invariant optical properties in order to estimate oxygenation changes. The total blood volume is a time variant property and could be estimated incorrectly in those first key frames.

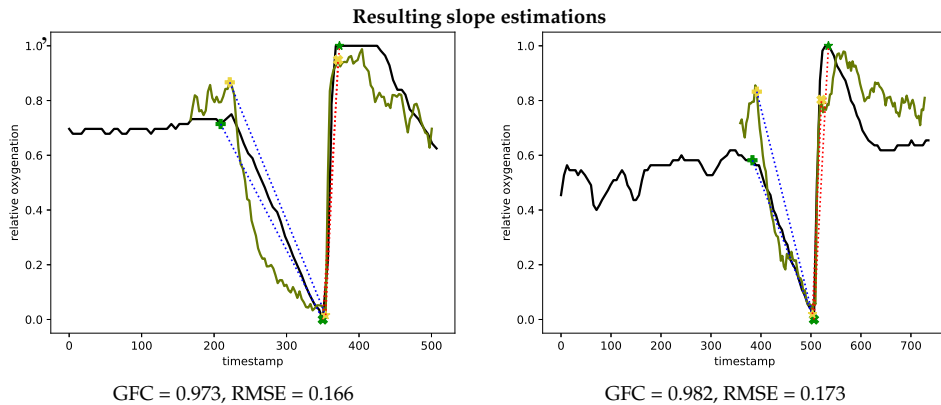


Figure 15. Representative oxygenation curves from the INVOS system (black) and estimates from the spectral filter array system (green). Linear desaturation (blue dots) between baseline (+) and low point of oxygenation (x (SFA) and * (INVOS)). Linear resaturation (red dots) between low point (x (SFA) and * (INVOS)) and high point (x (SFA) and * (INVOS)) of oxygenation. Representative curves with median GFC (left, #V46-2) and median RMSE (right, #V01-1) metrics.

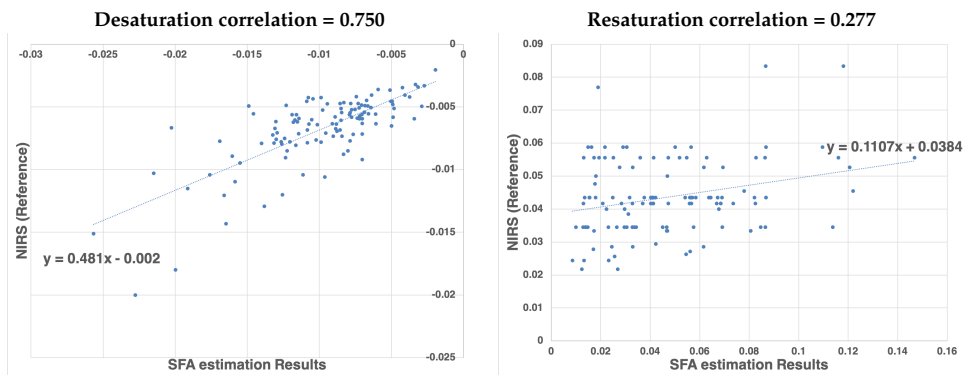


Figure 16. Correlation of de-saturation (left) and re-saturation (right) slope numbers between the proposed SFA setup and the clinical standard NIRS system.

The INVOS and SFA setup use different wavelength regimes, which represents different sampling volumes due to penetration depth depending on wavelength. Therefore, the SFA system measures more superficially compared to the INVOS system. The occlusion certainly blocks the blood distribution to both layers but the response in oxygen consumption might differ. For the upper arm occlusion following the proposed protocol the expected difference mainly affects the amplitude of oxygenation changes. Since the oxygen consumption is different in the two sampled volumes.

The normalization used for this work could positively affect the correlations between the visual range camera and the near infrared INVOS system. The feature scaling reduces the differences in the measured amplitude. The clinical gold standard has been used as a validation that the SFA system senses oxygenation concentration changes. The sample (Pearson) correlation coefficient between the reference measurement and the SFA system can be considered as an indication that the SFA setup measures these changes. Further investigation into the difference of sampling depth has to be carried out.

The oxygenation estimation with the SFA setup is based on three key wavelength. Results could be improved by using the full spectral curve for oxygen estimation and finding a fit to previously simulated spectra. Using all wavelength showed no improvement for the considered method in this

research as shown in Figure 14. An optimization of the band selection could improve the oxygenation estimation results. Bjorgen et al. [64] proposed a method for real time processing following this principle. Vyas et al. [65] combine Kubelka Munk forward modeling with machine learning approaches to estimate the chromophore concentrations from spectral signatures.

With further processing absolute oxygenation values could be determined. This study providing a ‘proof of concept’ is not at the stage to derive absolute oxygenation values. It provides a starting point by combining spectral correction and medically relevant processing of the measured spectra for further investigation.

4.3. Practical Use of SFA in a Clinical Environment

SFA cameras hold the potential to be a practical devices for medical applications given their acquisition speed, spatial and spectral acquisition properties, device size, potential ease of use and application versatility as a non-contact measurement method.

The aim of this study was to propose solutions for the technical limitations of this new kind of spectral imager while maintaining the full spectral, temporal and spatial capabilities. The current clinical gold standard for measuring oxygenation is limited to slow point measurements in direct contact to the patient impeding the applicability for burn-wound assessment, wound healing, neonatal units, local control measurements or even large scale operating room oxygenation monitoring. SFA cameras have the potential to improve upon the clinical gold standard for oxygenation measurements by non contact measurements with a spatial resolution and fast acquisition speed. In order to measure the oxygenation of burn-wounds a near infrared model of the camera might be necessary. Previous work [39] has shown that the proposed method for oxygen estimation can be applied to the near infrared version of the camera.

A step by step processing pipeline including black and white correction, spatial rearrangement and spectral correction and oxygenation estimation has been implemented. It was tested with an in vivo volunteer experiment using an existing commercially available SFA camera. The process can be generalized and used for other SFA cameras if the spectral sensitivities are known. This pipeline has been implemented in consideration of real time processing and requires little optimizations for a real time implementation. The matrix operations for the spectral calibration could be performed on the fly when implemented on a Field-programmable gate array (FPGA) added between the camera and the computer for processing. White and dark correction could be added as a calibration procedure before starting to use the camera. The oxygenation estimation in its simplified version can be implemented for real time application if incorporated into the acquisition program.

In the future less crosstalk between the channels would be desirable. The wavelength range is of importance depending on the application and a combination of both near infrared and visual wavelengths regimes would extent the use cases. Lower prices and wider adoption of SFA technology can be expected and should assist to mature this versatile and new technology for the medical field.

This study also shows the different aspects in which the processing of SFA cameras can be improved including optimal band selection, spectral correction and spatial processing and highlights the impact of specific steps on the final oxygenation estimation results.

4.4. Comparison to Related Work

Some studies [66] including Spigulis and Oshina [67] propose the estimation of absolute oxygenation values from an RGB imaging setup. An area of the skin is illuminated with different monochromatic laser light sources. Using an RGB sensor an image of the scene is acquired and a multi band image cube generated from the differently illuminated areas. This is a low-cost way of obtaining medically relevant narrow band channels but it requires a custom made illumination setup in conjunction with optimally chosen RGB sensor sensitivities.

Saager et al. [68] provide a theoretical framework for evaluation of the capability of different multispectral imaging techniques including spectral filter arrays to quantify chromophores in the

context of burn wound healing. They consider the same *XiSpec* SFA camera implementation on a theoretical level with an existing skin and phantom database. Simulated spectra were generated using the spectral sensitivities of the *XiSpec* SFA camera. Saager and his colleagues conclude that the camera provides reasonable accuracy for most common chromophores. Even-though, to the best of our knowledge the discussed spectral correction see Section 3.2 to account for double peaks was not applied to their theoretical data analysis. This stresses the indication of potential for SFA cameras as quantification tool for oxygenation related health metrics, since it could improve the resulting oxygen estimations.

Ewerløf et al. [28] propose the use of the same SFA camera for oxygenation estimation using an inverse Monte Carlo modeling. A database of Monte Carlo simulated spectra with known optical properties is prepared. The database of spectra is then multiplied by the sensor sensitivities and the illumination. This new database can then be used to estimate optical properties from measurements with the camera, by minimizing the difference between the pre simulated data and the measured camera responses. All channels measured by the camera are used for the estimation. It is not applying the spectral reconstruction and some of the additional channels might be introducing noise, due to their overlapping nature. While this method does not require the proposed spectral calibration, it requires prior Monte Carlo simulations adequately representing the patient population.

5. Conclusions

The feasibility of a commercially available SFA camera for clinical applications is tested. This study proposes a basic processing pipeline to solve shortcomings and challenges of this new spectral imaging technology. The pipeline maintains spectral, spatial and temporal capabilities of a commercially available SFA camera and is directly transferable to other SFA cameras. Technical challenges and indications by numerically correcting for double lobes in the spectral sensitivities have to be managed with care and a hardware based solution is advisable. SFA cameras and their benefits in a medical context have been studied by a proof of concept in vivo voluntary oxygenation experiment including 58 volunteers and 116 measurements. Results obtained have been validated with the clinical standard for oxygen measurements and promising agreement for the shapes of oxygenation curves were shown. The medically relevant parameters for desaturation and resaturation slopes show moderate correlations, which can be improved upon. This moderate correlation can be ascribed to slight differences in measurement frequency, difference in sampling depth and the strong impact of small differences for the calculated slopes. Aspects of the proposed processing need to be further improved including the spectral correction, real time processing, oxygenation estimation and real time visualizations.

Author Contributions: Conceptualization, J.R.B., J.Y.H. and R.M.V.; Data curation, J.R.B. and A.A.B.; Formal analysis, J.R.B.; Funding acquisition, J.Y.H.; Investigation, J.R.B. and A.A.B.; Methodology, J.R.B. and R.M.V.; Resources, R.M.V.; Software, J.R.B.; Supervision, J.Y.H. and R.M.V.; Validation, J.R.B.; Visualization, J.R.B.; Writing original draft, J.R.B.; Writing—review & editing, J.R.B., J.Y.H. and R.M.V.

Funding: This research has been supported by the Research Council of Norway through project No. 247689 “IQ-MED: Image Quality enhancement in MEDical diagnosis, monitoring and treatment”.

Acknowledgments: I hereby acknowledge the assistance by Herke Jan Noordmans from Utrecht Medical Center to implement the workflow into *MultiSpec*. Furthermore, I would like to thank Diedericks Gebbers for his oversight of the experimental data in the clinic.

Conflicts of Interest: The authors declare no conflict of interest.

Abbreviations

The following abbreviations are used in this manuscript:

SFA	Spectral filter array
NIRS	near infrared reflectance spectroscopy
VOT	vascular occlusion test
VIS	visual range
ROI	region of interest
GFC	goodness of fit coefficient
RMSE	root mean square error

References

1. Wieringa, F.P.; Mastik, F.; van der Steen, A.F.W. Contactless Multiple Wavelength Photoplethysmographic Imaging: A First Step Toward “SpO₂ Camera” Technology. *Ann. Biomed. Eng.* **2005**, *33*, 1034–1041. [[CrossRef](#)] [[PubMed](#)]
2. Van Gastel, M.; Stuijk, S.; De Haan, G. New principle for measuring arterial blood oxygenation, enabling motion-robust remote monitoring. *Sci. Rep.* **2016**, *6*, 38609. [[CrossRef](#)] [[PubMed](#)]
3. Randeberg, L.L.; Baarstad, I.; Løke, T.; Kaspersen, P.; Svaasand, L.O. Hyperspectral imaging of bruised skin. In *Photonic Therapeutics and Diagnostics II*; SPIE: Bellingham, WA, USA, 2006; Volume 6078, p. 60780O. [[CrossRef](#)]
4. Randeberg, L.L.; Winnem, A.M.; Blindheim, S.; Haugen, O.A.; Svaasand, L.O. Optical classification of bruises. In *Lasers in Surgery: Advanced Characterization, Therapeutics, and Systems XIV*; SPIE: Bellingham, WA, USA, 2004; Volume 5312. [[CrossRef](#)]
5. Cotton, S.; Claridge, E.; Hall, P. A skin imaging method based on a colour formation model and its application to the diagnosis of pigmented skin lesions. In *Proceedings of the Medical Image Understanding and Analysis*; BMVA: Oxford, UK, 1999; pp. 49–52.
6. Nakao, D.; Tsumura, N.; Miyake, Y. Realtime multispectral image processing for mapping pigmentation in human skin. In *Proceedings of the Ninth IS&T/SID Color Imaging Conference*, IS&T, Scottsdale, AZ, USA, 7–10 November 1995; pp. 80–84.
7. Nagaoka, T.; Nakamura, A.; Kiyohara, Y.; Sota, T. Melanoma screening system using hyperspectral imager attached to imaging fiberscope. In *Proceedings of the 2012 Annual International Conference of the IEEE Engineering in Medicine and Biology Society*, San Diego, CA, USA, 28 August–1 September 2012; Volume 2012, pp. 3728–3731.
8. Sowa, M.G.; Leonardi, L.; Payette, J.R.; Cross, K.M.; Gomez, M.; Fish, J. Classification of burn injuries using near-infrared spectroscopy. *J. Biomed. Opt.* **2006**, *11*, 054002. [[CrossRef](#)] [[PubMed](#)]
9. Thatcher, J.E.; Squiers, J.J.; Kanick, S.C.; King, D.R.; Lu, Y.; Wang, Y.; Mohan, R.; Sellke, E.W.; DiMaio, J.M. Imaging Techniques for Clinical Burn Assessment with a Focus on Multispectral Imaging. *Adv. Wound Care* **2016**, *5*, 360–378. [[CrossRef](#)] [[PubMed](#)]
10. Lu, G.; Fei, B. Medical hyperspectral imaging: A review. *J. Biomed. Opt.* **2014**, *19*, 010901–010924. [[CrossRef](#)] [[PubMed](#)]
11. Huang, J. Multispectral Imaging of Skin Oxygenation. Ph.D. Thesis, The Ohio State University, Columbus, OH, USA, 2013.
12. Sorg, B.S.; Moeller, B.J.; Donovan, O.; Cao, Y.; Dewhirst, M.W. Hyperspectral imaging of hemoglobin saturation in tumor microvasculature and tumor hypoxia development. *J. Biomed. Opt.* **2005**, *10*, 044004–044011. [[CrossRef](#)] [[PubMed](#)]
13. Fawzy, Y.; Zeng, H. Spectral Imaging Technology-A Review on Skin and Endoscopy Applications. *Recent Pat. Med. Imaging* **2014**, *4*, 101–109. [[CrossRef](#)]
14. Wang, X.; Thomas, J.B.; Hardeberg, J.Y.; Gouton, P. A Study on the Impact of Spectral Characteristics of Filters on Multispectral Image Acquisition. In *Proceedings of the 12th Congress of the International Colour Association*, Newcastle, UK, 8–12 July 2013; Volume 4, pp. 1765–1768.
15. Mihoubi, S.; Losson, O.; Mathon, B.; Macaire, L. Multispectral Demosaicing Using Pseudo-Panchromatic Image. *IEEE Trans. Comput. Imaging* **2017**, *3*, 982–995. [[CrossRef](#)]

16. Hagen, N.A.; Kudenov, M.W. Review of snapshot spectral imaging technologies. *Opt. Eng.* **2013**, *52*, 090901. [[CrossRef](#)]
17. Wang, X.; Thomas, J.B.; Hardeberg, J.Y.; Gouton, P. Multispectral imaging: Narrow or wide band filters? *JAIIC J. Int. Colour Assoc.* **2014**, *12*, 44–51.
18. Najiminaini, M.; Vasefi, F.; Kaminska, B.; Carson, J.J.L. Nanohole-array-based device for 2D snapshot multispectral imaging. *Sci. Rep.* **2013**, *3*, 2589. [[CrossRef](#)] [[PubMed](#)]
19. Park, H.; Crozier, K.B. Multispectral imaging with vertical silicon nanowires. *Sci. Rep.* **2013**, *3*, 2460. [[CrossRef](#)] [[PubMed](#)]
20. Lapray, P.J.; Wang, X.; Thomas, J.B.; Gouton, P. Multispectral filter arrays: Recent advances and practical implementation. *Sensors* **2014**, *14*, 21626–21659. [[CrossRef](#)] [[PubMed](#)]
21. Daisuke, K.; Yusuke, M.; Masayuki, T.; Masatoshi, O. Simultaneous capturing of RGB and additional band images using hybrid color filter array. In *Digital Photography X*; SPIE: Bellingham, WA, USA, 2014; Volume 9023, p. 90230V. [[CrossRef](#)]
22. Monno, Y.; Kikuchi, S.; Tanaka, M.; Okutomi, M. A Practical One-Shot Multispectral Imaging System Using a Single Image Sensor. *IEEE Trans. Image Process.* **2015**, *24*, 3048–3059. [[CrossRef](#)] [[PubMed](#)]
23. Geelen, B.; Blanch, C.; Gonzalez, P.; Tack, N.; Lambrechts, A. A tiny VIS-NIR snapshot multispectral camera. In *Advanced Fabrication Technologies for Micro/Nano Optics and Photonics VIII*; SPIE: Bellingham, WA, USA, 2015; Volume 9374, p. 937414. [[CrossRef](#)]
24. Thomas, J.B.; Lapray, P.J.; Gouton, P.; Clerc, C. Spectral Characterization of a Prototype SFA Camera for Joint Visible and NIR Acquisition. *Sensors* **2016**, *16*, 993. [[CrossRef](#)] [[PubMed](#)]
25. PIXELTEQ. Micro-Patterned Optical Filters for Multispectral Imaging. 2018. Available online: <https://www.pixelteq.com/> (accessed on 2 December 2018).
26. SILIOS. Multispectral-Imaging. 2018. Available online: <https://www.silios.com> (accessed on 2 December 2018).
27. IMEC. Hyperspectral-Imaging. 2018. Available online: <https://www.imec-int.com> (accessed on 2 December 2018).
28. Ewerlöf, M.; Larsson, M.; Salerud, E.G. Spatial and temporal skin blood volume and saturation estimation using a multispectral snapshot imaging camera. In *Imaging, Manipulation, and Analysis of Biomolecules, Cells, and Tissues XV*; SPIE: Bellingham, WA, USA, 2017; Volume 10068, p. 1006814. [[CrossRef](#)]
29. Miao, L.; Qi, H.; Ramanath, R.; Snyder, W.E. Binary tree-based generic demosaicking algorithm for multispectral filter arrays. *IEEE Trans. Image Process.* **2006**, *15*, 3550–3558. [[CrossRef](#)] [[PubMed](#)]
30. Lapray, P.J.; Thomas, J.B.; Gouton, P. High Dynamic Range Spectral Imaging Pipeline for Multispectral Filter Array Cameras. *Sensors* **2017**, *17*, 1281. [[CrossRef](#)]
31. Gioux, S.; Mazhar, A.; Lee, B.T.; Lin, S.J.; Tobias, A.M.; Cuccia, D.J.; Stockdale, A.; Oketokoun, R.; Ashitate, Y.; Kelly, E.; et al. First-in-human pilot study of a spatial frequency domain oxygenation imaging system. *J. Biomed. Opt.* **2011**, *16*, 086015. [[CrossRef](#)]
32. Caspary, L.; Thum, J.; Creutzig, A.; Lubbers, D.W.; Alexander, K. Quantitative Reflection Spectrophotometry: Spatial and Temporal Variation of Hb Oxygenation in Human Skin. *Int. J. Microcirc.* **1995**, *15*, 131–136. [[CrossRef](#)]
33. Nishidate, I.; Maeda, T.; Niizeki, K.; Aizu, Y. Estimation of Melanin and Hemoglobin Using Spectral Reflectance Images Reconstructed from a Digital RGB Image by the Wiener Estimation Method. *Sensors* **2013**, *13*, 7902–7915. [[CrossRef](#)]
34. Yoshiya, I.; Shimada, Y.; Tanaka, K. Spectrophotometric monitoring of arterial oxygen saturation in the fingertip. *Med. Biol. Eng. Comput.* **1980**, *18*, 27–32. [[CrossRef](#)] [[PubMed](#)]
35. Cuccia, D. Design and Validation of a Spatial Frequency Domain Imaging (SFDI) System for Biomedical Research Applications. In *Frontiers in Optics*; OSA: Washington, DC, USA, 2015; p. FM2C.1.
36. Cuccia, D. Validation of Spatial Frequency Domain Imaging (SFDI) for Biomedical Research Applications. In *Applied Industrial Optics: Spectroscopy, Imaging and Metrology*; OSA: Washington, DC, USA, 2015; p. AIT2C.2.
37. Ghijssen, M.; Durkin, A.J.; Gioux, S.; Tromberg, B.J. Real-time simultaneous single snapshot of optical properties and blood flow using coherent spatial frequency domain imaging (cSFDI). *Biomed. Opt. Express* **2016**, *7*, 870–813. [[CrossRef](#)] [[PubMed](#)]
38. Spigulis, J.; Rubins, U.; Kviesis-Kipge, E.; Rubenis, O. SkImager: A concept device for in-vivoskin assessment by multimodal imaging. *Proc. Est. Acad. Sci.* **2014**, *63*, 301–308. [[CrossRef](#)]

39. Bauer, J.R.; van Beekum, K.; Klaessens, J.H.G.M.; Noordmans, H.J.; Boer, C.; Hardeberg, J.Y.; Verdaasdonk, R.M. Towards real-time non contact spatial resolved oxygenation monitoring using a multi spectral filter array camera in various light conditions. In *Optical Biopsy XVI: Toward Real-Time Spectroscopic Imaging and Diagnosis*; SPIE: Bellingham, WA, USA, 2018; Volume 10489, p. 1048900. [[CrossRef](#)]
40. van Gemert, M.J.C.; Jacques, S.L.; Sterenborg, H.J.C.M.; Star, W.M. Skin optics. *IEEE Trans. Biomed. Eng.* **1989**, *36*, 1146–1154. [[CrossRef](#)] [[PubMed](#)]
41. Jacques, S.L. Optical properties of biological tissues: A review. *Phys. Med. Biol.* **2013**, *58*, R37. [[CrossRef](#)] [[PubMed](#)]
42. Fodor, L.; Elman, M.; Ullmann, Y. *Aesthetic Applications of Intense Pulsed Light*; Springer Science & Business Media: Berlin, Germany, 2010.
43. Bauer, J.R.; Pedersen, M.; Hardeberg, J.Y.; Verdaasdonk, R. Skin color simulation—Review and analysis of available Monte Carlo-based photon transport simulation models. In Proceedings of the 25th Color and Imaging Conference Final Program and Proceeding, Lillehammer, Norway, 11–15 September 2017; pp. 165–170.
44. Jacques, S.L.; Prahl, S.A. A Collaboration of Oregon Health & Science University, Portland State University, and the Oregon Institute of Technology. Optical Spectra. 2015. Available online: <https://omlc.org/spectra/index.html> (accessed on 24 July 2019).
45. Wang, L.V.; Wu, H. *Biomedical Optics: Principles and Imaging*; John Wiley & Sons: Hoboken, NJ, USA, 2012.
46. Ximea. Hyperspectral Cameras. 2018. Available online: <https://www.ximea.com> (accessed on 2 December 2018).
47. Sadeghipoor, Z.; Thomas, J.B.; Süssstrunk, S. Demultiplexing Visible and Near-Infrared Information in Single-Sensor Multispectral Imaging. In Proceedings of the Color Computational Imaging Conference (CIC 24), San Diego, CA, USA, 7–11 November 2016; pp. 76–81. [[CrossRef](#)]
48. Park, C.; Kang, M. Color Restoration of RGBN Multispectral Filter Array Sensor Images Based on Spectral Decomposition. *Sensors* **2016**, *16*, 719. [[CrossRef](#)] [[PubMed](#)]
49. Jørgensen, J.S.; Schmid, E.R.; König, V.; Faisst, K.; Huch, A.; Huch, R. Limitations of forehead pulse oximetry. *J. Clin. Monit.* **1995**, *11*, 253–256. [[CrossRef](#)]
50. Futier, E.; Christophe, S.; Robin, E.; Petit, A.; Pereira, B.; Desbordes, J.; Bazin, J.E.; Vallet, B. Use of near-infrared spectroscopy during a vascular occlusion test to assess the microcirculatory response during fluid challenge. *Crit. Care* **2011**, *15*, R214. [[CrossRef](#)]
51. Bernet, C.; Desebbe, O.; Bordon, S.; Lacroix, C.; Rosamel, P.; Farhat, F.; Lehot, J.J.; Cannesson, M. The impact of induction of general anesthesia and a vascular occlusion test on tissue oxygen saturation derived parameters in high-risk surgical patients. *J. Clin. Monit. Comput.* **2011**, *25*, 237. [[CrossRef](#)] [[PubMed](#)]
52. Lipcsey, M.; Woinarski, N.C.; Bellomo, R. Near infrared spectroscopy (NIRS) of the thenar eminence in anesthesia and intensive care. *Ann. Intensive Care* **2012**, *2*, 11. [[CrossRef](#)] [[PubMed](#)]
53. Abdelmalak, B.; Cata, J.; Bonilla, A.; You, J.; Kopyeva, T.; Vogel, J.; Campbell, S.; Sessler, D. Intraoperative tissue oxygenation and postoperative outcomes after major non-cardiac surgery: An observational study. *Br. J. Anaesth.* **2012**, *110*, 241–249. [[CrossRef](#)] [[PubMed](#)]
54. McCann, J. Retinex Theory. In *Encyclopedia of Color Science and Technology*; Springer: New York, NY, USA, 2016; pp. 1118–1125. [[CrossRef](#)]
55. de Roode, R.; Noordmans, H.J.; Rem, A.; Couwenberg, S.; Verdaasdonk, R. Evaluation of laser treatment response of vascular skin disorders in relation to skin properties using multi-spectral imaging. In *Photonic Therapeutics and Diagnostics IV*; SPIE: Bellingham, WA, USA, 2008; Volume 6842, p. 68420B. [[CrossRef](#)]
56. Noordmans, H.J.; Woerdeman, P.A.; Willems, P.W.A.; van Rijen, P.C.; Berkelbach van der Sprenkel, J.W. Sound and volumetric workflow feedback during image guided neurosurgery. In *Photonic Therapeutics and Diagnostics IV*; SPIE: Bellingham, WA, USA, 2008; Volume 6842, p. 68422J. [[CrossRef](#)]
57. Connah, D.; Hardeberg, J.Y.; Westland, S. Comparison of linear spectral reconstruction methods for multispectral imaging. In Proceedings of the 2004 International Conference on Image Processing, ICIP'04, Singapore, 24–27 October 2004; Volume 3, pp. 1497–1500.
58. Klaessens, J.H.G.M.; Noordmans, H.J.; de Roode, R.; Verdaasdonk, R.M. Non-invasive skin oxygenation imaging using a multi-spectral camera system: Effectiveness of various concentration algorithms applied on human skin. In *Optical Tomography and Spectroscopy of Tissue VIII*; SPIE: Bellingham, WA, USA, 2009; Volume 7174, p. 717408. [[CrossRef](#)]

59. Klaessens, J.H.G.M.; Landman, M.; de Roode, R.; Noordmans, H.J.; Verdaasdonk, R.M. Thermographic and oxygenation imaging system for non-contact skin measurements to determine the effects of regional block anesthesia. In *Photonic Therapeutics and Diagnostics VI*; SPIE: Bellingham, WA, USA, 2010; Volume 7548, p. 75484S. [[CrossRef](#)]
60. Klaessens, J.H.G.M.; De Roode, R.; Verdaasdonk, R.M.; Noordmans, H.J. Hyperspectral imaging system for imaging O₂Hb and HHb concentration changes in tissue for various clinical applications. In *Advanced Biomedical and Clinical Diagnostic Systems IX*; SPIE: Bellingham, WA, USA, 2011; Volume 7890, p. 78900R. [[CrossRef](#)]
61. Delpy, D.T.; Cope, M.; van der Zee, P.; Arridge, S.; Wray, S.; Wyatt, J. Estimation of optical pathlength through tissue from direct time of flight measurement. *Phys. Med. Biol.* **1988**, *33*, 1433. [[CrossRef](#)] [[PubMed](#)]
62. Pub, C. *CIE 15: Technical Report: Colorimetry*, 3rd ed.; CIE Central Bureau: Vienna, Austria, 2004; Volume 3.
63. Mayeur, C.; Campard, S.; Richard, C.; Teboul, J.L. Comparison of four different vascular occlusion tests for assessing reactive hyperemia using near-infrared spectroscopy. *Crit. Care Med.* **2011**, *39*, 695–701. [[CrossRef](#)] [[PubMed](#)]
64. Bjorgan, A.; Milanič, M.; Randeberg, L.L. Estimation of skin optical parameters for real-time hyperspectral imaging applications. *J. Biomed. Opt.* **2014**, *19*, 066003. [[CrossRef](#)]
65. Vyas, S.; Banerjee, A.; Burlina, P. Estimating physiological skin parameters from hyperspectral signatures. *J. Biomed. Opt.* **2013**, *18*, 057008. [[CrossRef](#)]
66. Spigulis, J.; Elste, L. Single snapshot RGB multispectral imaging at fixed wavelengths: Proof of concept. *Proc. SPIE* **2014**, *8937*, 89370L.
67. Spigulis, J.; Oshina, I. Snapshot RGB mapping of skin melanin and hemoglobin. *J. Biomed. Opt.* **2015**, *20*, 050503. [[CrossRef](#)]
68. Saager, R.B.; Baldado, M.L.; Rowland, R.A.; Kelly, K.M.; Durkin, A.J. Method using in vivo quantitative spectroscopy to guide design and optimization of low-cost, compact clinical imaging devices: Emulation and evaluation of multispectral imaging systems. *J. Biomed. Opt.* **2018**, *23*, 046002. [[CrossRef](#)]



© 2019 by the authors. Licensee MDPI, Basel, Switzerland. This article is an open access article distributed under the terms and conditions of the Creative Commons Attribution (CC BY) license (<http://creativecommons.org/licenses/by/4.0/>).

Towards real-time non contact spatial resolved oxygenation monitoring using a multi spectral filter array camera in various light conditions

Paper D

This chapter is a reprint of the publication:

Jacob. R. Bauer; Karlijn v. Beekum; John H.G.M Klaessens; Herke J. Noordmans; Christa Boer; Jon Y. Hardeberg, and Rudolf M. Verdaasdonk; "Towards real-time non contact spatial resolved oxygenation monitoring using a multi spectral filter array camera in various light conditions" *Proceedings of SPIE Volume 10489, Optical Biopsy XVI: Toward Real-Time Spectroscopic Imaging and Diagnosis; Event: BIOS, 2018, San Francisco, California, United States .*

PROCEEDINGS OF SPIE

SPIDigitalLibrary.org/conference-proceedings-of-spie

Towards real-time non contact spatial resolved oxygenation monitoring using a multi spectral filter array camera in various light conditions

Jacob R. Bauer, Karlijn van Beekum, John Klaessens, Herke Jan Noordmans, Christa Boer, et al.

Jacob R. Bauer, Karlijn van Beekum, John Klaessens, Herke Jan Noordmans, Christa Boer, Jon Y. Hardeberg, Rudolf M. Verdaasdonk, "Towards real-time non contact spatial resolved oxygenation monitoring using a multi spectral filter array camera in various light conditions," Proc. SPIE 10489, Optical Biopsy XVI: Toward Real-Time Spectroscopic Imaging and Diagnosis, 104890O (19 February 2018); doi: 10.1117/12.2288432

SPIE.

Event: SPIE BIOS, 2018, San Francisco, California, United States

Towards real-time non contact spatial resolved oxygenation monitoring using a multi spectral filter array camera in various light conditions

Jacob R. Bauer^a, Karlijn van Beekum^b, John Klaessens^b, Herke Jan Noordmans^c, Christa Boer^b, Jon Y. Hardeberg^a, and Rudolf M. Verdaasdonk^b

^aNorwegian University of Science and Technology, The Norwegian Colour and Visual Computing Laboratory, Gjøvik, Norway

^bVU University Medical Center, Dept. of Physics & Medical Technology, Amsterdam, Netherlands

^cUniversity Medical Center Utrecht, Dept. of Medical Technology and Clinical Physics, Utrecht, Netherlands

ABSTRACT

Non contact spatial resolved oxygenation measurements remain an open challenge in the biomedical field and non contact patient monitoring. Although point measurements are the clinical standard till this day, regional differences in the oxygenation will improve the quality and safety of care. Recent developments in spectral imaging resulted in spectral filter array cameras (SFA). These provide the means to acquire spatial spectral videos in real-time and allow a spatial approach to spectroscopy. In this study, the performance of a 25 channel near infrared SFA camera was studied to obtain spatial oxygenation maps of hands during an occlusion of the left upper arm in 7 healthy volunteers. For comparison a clinical oxygenation monitoring system, INVOS, was used as a reference. In case of the NIRS SFA camera, oxygenation curves were derived from 2-3 wavelength bands with a custom made fast analysis software using a basic algorithm. Dynamic oxygenation changes were determined with the NIR SFA camera and INVOS system at different regional locations of the occluded versus non-occluded hands and showed to be in good agreement. To increase the signal to noise ratio, algorithm and image acquisition were optimised. The measurement were robust to different illumination conditions with NIR light sources. This study shows that imaging of relative oxygenation changes over larger body areas is potentially possible in real time.

Keywords: spectral filter array camera, non- contact monitoring, near infrared, oxygenation, skin assessment, optical diagnosis,

1. INTRODUCTION

Light reflected from skin undergoes interactions within the tissue and the resulting reflected spectrum carries useful information, like chromophore concentrations,¹ blood perfusion² and information about the oxygenation of skin tissue.³ Oxygenation is a useful health metric indicating nutrition supply and homeostasis of tissue. The oxygenation information can be used to indicate cancerous regions,⁴ give insides into wound healing processes of chronic wounds, and can be utilized as a first care measurement indicating the severity of burn-wounds.⁵ Next to visual assessment of the skin, so called diffuse reflectance spectroscopy is utilized in the clinics. These are spectral point measurements and are used for measuring oxygen concentration or the concentration of other chromophores present in superficial skin tissue. Diffuse reflectance spectroscopy is often based on optical fibers and a defined optical setup. Most commonly one fiber is used to deliver the light to the tissue surface and one or more fibers are used to sense the diffuse reflectance from the tissue and measures spectra through a diffraction grating. Through Monte Carlo modeling or diffusion theory chromophore concentrations in the skin

Further author information: (Send correspondence to J.R.Bauer)

J.R.Bauer: E-mail: jacob.bauer@ntnu.no, Telephone: 0049 173 421 3461

Optical Biopsy XVI: Toward Real-Time Spectroscopic Imaging and Diagnosis, edited by Robert R. Alfano, Stavros G. Demos
Proc. of SPIE Vol. 10489, 1048900 · © 2018 SPIE · CCC code: 1605-7422/18/\$18 · doi: 10.1117/12.2288432

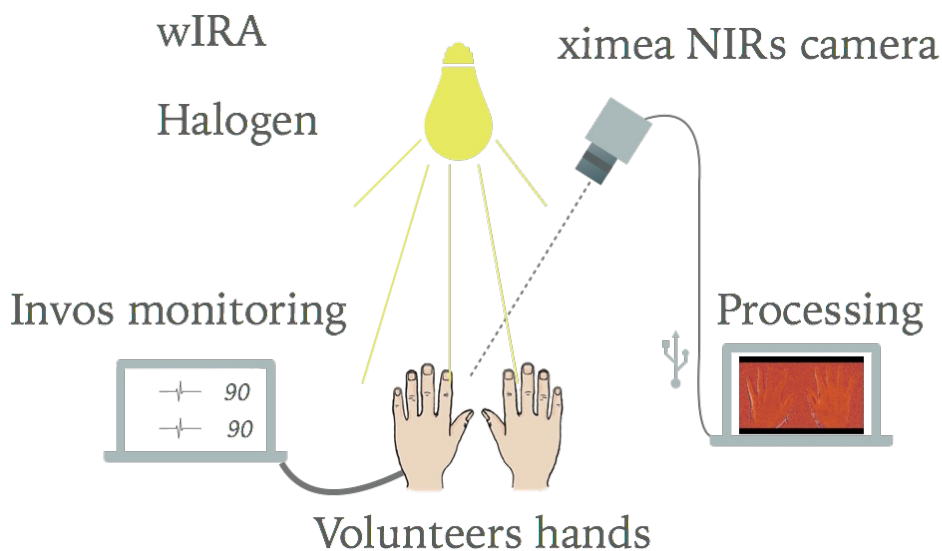


Figure 1. experimental setup, parallel measurement of spectral reflectance with the NIR SFA camera and the clinically approved INVOS system

can be derived. Diffuse reflectance spectroscopy is limited to point measurements and therefore measure the oxygen saturation in a small area. Since the oxygenation or oxygen concentration differs greatly throughout the tissue a spatially resolved measurement could be beneficial. It has been shown that spectral imaging using various different techniques could be applied.⁶⁻⁸ Most commonly spectral imaging techniques, like spectral filter wheels, liquid crystal filter cameras resolve the spectral dimension through time variant sampling. Spectral filter array cameras on the other hand are a new type of spectral imaging devices with the ability to acquire a spectral cube in a single shot within milliseconds preventing motion artifacts due to time difference between spectral channels as with common spectral imaging techniques. Since blood perfusion and oxygen distribution is a dynamic process, information is lost if the spectral sampling is performed over time. In this study, capabilities of a commercially available spectral filter array (SFA) near infrared (NIR) camera manufactured by XIMEA (XiSpec MQ022HG-IM-SM5X5-NIR) with an IMEC sensor as a spatially resolved oxygenation measurement were studied. We hereby focus on the postprocessing steps necessary in order to derive oxygenation readings and compare with a clinical system (INVOS Somanetics 5100 C of Covidien) as local point oxygenation measurement tool.

2. METHODS

As proof of concept measurements were conducted in 11 healthy volunteers. The volunteers placed their hands on the measurement table with a distance of around 1cm between their hands. The experimental setup is shown in Figure 1. The so called upper arm occlusion protocol was used, where pressure was applied to the left upper arm using an inflatable cuff. Through the cuff the blood flow into the left hand was occluded, while the right hand blood circulation is unaltered. The hands of the volunteer were measured continuously both with the multispectral SFA camera and the INVOS spectroscopy device. First a baseline measurement was performed for 2 minutes without applying any pressure. Followed by 3 minutes of measuring the hands with the cuff inflated and occlusion applied for 3 minutes. The pressure applied was around 160mmHg and a marker was added to the imaged scene as soon as the occlusion was applied. After the occlusion phase, another 5 minutes was acquired of the re-perfusion phase. All volunteers were measured twice with 1 day in-between in order to allow inter measurement comparison.

Table 1. Settings for the XIMEA camera for the measurements

	Halogen light source
Filter range	600 875 nm
Aperture	1.65
RAW	16
Exposure	19 ms
Gain	0.00 dB
FPs	1.00
Limit bandwidth	2843 Mbit/s
Manual WB (R : G : B)	1.00 : 1.00 : 1.00

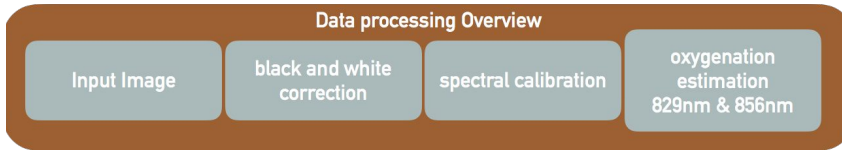


Figure 2. Overview of the dataprocessing for the NIR SFA data

2.1 Multispectral Imaging

The multispectral measurements included in this research are performed using the XIMEA (MQ022HG-IM-SM5X5-NIR camera) and the Xicam (acquisition) tool by XIMEA. In addition, a custom build software program 'Multispec' (developed by Herke Jan Noordmans from the UMC Utrecht, The Netherlands) was used for the data processing of the 25 narrow band snap shot spectral images. The spectral sensitivity is in the NIR range between 600nm-875nm. A 'dark' image was obtained for background noise correction.

In addition, a flat field correction was performed using a uniform grey surface to account for an in-homogenous illumination of the scene and to account for the unique spectral power distribution of the light source.

A grey correction target was used in order to allow for the same exposure time, aperture and frames per second compared to the test measurements of the hand. Therefore the final image was given as:

$$I_n(x, y) = \frac{I_{Sn}(x, y) - I_{Dn}(x, y)}{I_{Wn}(x, y) - I_{Dn}(x, y)} \quad (1)$$

The final image was given by dividing the sample image minus the dark current image divided by the grey sheet image minus the dark image. Due to considerable overlap of the different spectral channels, a spectral correction was necessary and reduced the number of effective channels to 10. The correction is performed via a matrix operation with correction values reported by the camera manufacturer, which are based on the specific spectral sensitivities of the camera. Figure 2 shows the final data processing steps in order to arrive at the oxygenation estimations based on the NIR SFA camera. The selected camera parameters for acquisition can be found in Table 1. A sequence of 1 frame per second during 15 minutes was acquired.

2.1.1 Light source

The Measurements were performed with a halogen light source which spectra is shown in Figure 3. It is a continuous lightsource, which is commercially available. This was important to ensure a save use in the clinic and at the same time guarantee enough light intensity in the near infrared. For the setup in order to avoid specular reflections the lightsource was used in a 45° angle towards the imaging equipment.

2.2 Reference measurements

As references for the oxygenation, the INVOS Semantics 5100 C was used with a contact sensor attached to the palms of both hands. The sensors were attached tightly to the palm of the hand to ensure consistent readings with the INVOS system. Both measurements were performed at the same time and continuous oxygenation measurements were acquired. In contrast to the multispectral measurements, the INVOS system performed a

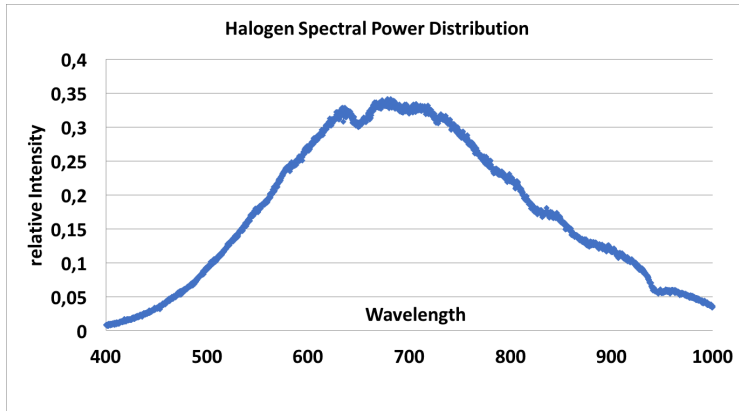


Figure 3. Halogen light source spectral power distribution measurement with Thorlabs

measurement every 5-6 seconds. In order to align both measurements the moment of occlusion was marked in the the INVOS system, simultaneously a marker was added to the imaged scene. This allows to mark the timepoint of occlusion and that of the release of the pressure inflatable cuff up to the reaction times of the researcher conducting the measurements.

2.3 Data analysis for Oxygenation estimation

The SFA camera used in this research provides a spatially resolved measure of 25 different wavelengths reflected from the image scene. This information has to be utilized in order to estimate the oxygenation of the tissue in different regions or spatially resolved per pixel. For this research, oxygenation estimation algorithms were applied, which can potentially be performed in real time. The modified Beer-Lambert method was used which has been previously reported as the Δt method in some publications⁹⁻¹¹ The basis for this method lies in the modified Beer-Lambert and considers absorption and scattering the main reasons for the attenuation of light in skin. This method assumes a change of absorption over time due to the concentration of chromophores present in the skin: in particular, the differences in oxy-, and deoxy- hemoglobin concentration present in the skin. Part of the total absorption of skin is hereby considered to be constant, due to other unchanged chromophores present in the skin. oxy- and deoxy- hemoglobin concentration are considered to change over time during the measurement and are the property of investigation. The Optical density or absorption can be defined as:

$$OD = -\log_{10}\left(\frac{I}{I_0}\right) = \sum_n \varepsilon_n * c_n * d, \quad (2)$$

where OD stands for optical density I_0 is the emitted light intensity, and I is the intensity of the received light, ε describes the molar extinction coefficient for n different chromophores, c describes the concentration of the chromophore n and d describes the path-length for the light. Since scattering increases the path-length of light travelling through the tissue the modified Beer-Lambert law¹² can be used to describe this with:

$$\overline{A(\lambda)} = \overline{\varepsilon(\lambda)} * \overline{c(t)} * \overline{D_{PF}(\lambda)} * d + \overline{G(\lambda)} + \overline{H(t)}, \quad (3)$$

where $\overline{A(\lambda)}$ is the absorbance [-], $\overline{\varepsilon(\lambda)}$ describes the molar extinction coefficient [$mM^{-1}cm^{-1}$], $\overline{c(t)}$ is the concentration of a specific chromophore [mM], $\overline{D_{PF}(\lambda)}$ differential path length factor corrects the geometrical source-detector distance to the mean optical path in the tissue, d the source detector distance [cm], and $\overline{G(\lambda)}$ and $\overline{H(t)}$ are both oxygen independent loss factors accounting for scattering, absorption and geometry losses where $\overline{H(t)}$ is time dependant and $\overline{G(\lambda)}$ is wavelength dependant.

This can be rewritten in matrix form and with i.e. 3 specific wavelength to:

$$\begin{bmatrix} A(\lambda_1, t) \\ A(\lambda_2, t) \\ A(\lambda_3, t) \end{bmatrix} = \begin{bmatrix} \varepsilon_{O_2Hb}(\lambda_1)D_{PF}(\lambda_1) & \varepsilon_{HHb}(\lambda_1)D_{PF}(\lambda_1) \\ \varepsilon_{O_2Hb}(\lambda_2)D_{PF}(\lambda_2) & \varepsilon_{HHb}(\lambda_2)D_{PF}(\lambda_2) \\ \varepsilon_{O_2Hb}(\lambda_3)D_{PF}(\lambda_3) & \varepsilon_{HHb}(\lambda_3)D_{PF}(\lambda_3) \end{bmatrix} * \begin{bmatrix} c_{O_2Hb}(t) \\ c_{HHb}(t) \end{bmatrix} d + \begin{bmatrix} G(\lambda_1) \\ G(\lambda_2) \\ G(\lambda_3) \end{bmatrix} + \begin{bmatrix} H(t) \\ H(t) \\ H(t) \end{bmatrix}$$

Under the assumption that the H term is zero or constant in time and the G term also stays constant during the measurement. Then the differences in concentration in a time interval Δt relative to a stable starting point can be calculated. A known $D_{PF}(\lambda)$ values from literature for the interrogated tissue have been used to simplify the equation to determine the concentration of a chromophore to:

$$\Delta_t \bar{c} = \frac{\bar{\varepsilon} D_{PF}^{-1} \Delta_t \bar{A}}{d} \quad (4)$$

For this setup, the use of two different wavelengths (826 and 859nm) proved to be best for the calculation of the oxy-,deoxy- concentration present in the tissue. It allowed to relate changes in reflected light intensity to changes in oxy and deoxy hemoglobin concentration. Consequently, this technique was used to estimate oxygen concentration from our spectral image cubes. This was done in specifically chosen regions of interest which will be described further in the next section.

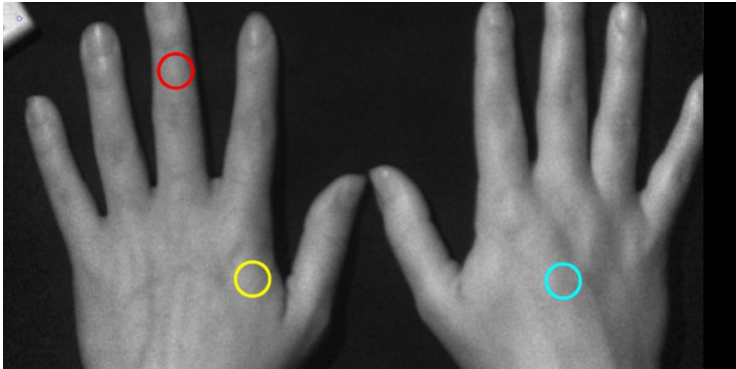


Figure 4. Circles indicate areas of interrogation an average was taken from these pixel areas and the average oxygenation of these areas was plotted over time

3. RESULTS

From the images, a region of interest was defined for the estimation of oxygenation in the hands. Figure 4 illustrates these different regions of interest. An average oxygenation concentration was calculated for each region. These areas have been chosen as close to the measurement location of the INVOS system, far away from the measurement location of the INVOS system and it has also been reported that the finger tips show stronger desaturations and lastly one of the regions of interest in the hand without any occlusion was chosen in order to verify the oxygenation behaviour in the unaltered hand.

Figure 5 shows a representative result of one volunteer of estimated oxygen concentration using the halogen light source. In grey is the relative reflected intensity of our marker plotted, which was included into the scene to indicate the occlusion and cuff release. Oxygenation is represented by the blue line and deoxygenation with the orange line. Both follow the expected curves and show good agreement with previously reported occlusion behaviour.¹³

Figure 6 shows that the agreement between INVOS system and estimated oxygenations from the NIR system are close during deoxygenation, reperfusion and "back to baseline". This measurement was chosen as representative for the entire dataset of 11 healthy volunteers. Among all measurements the same trend when compared to

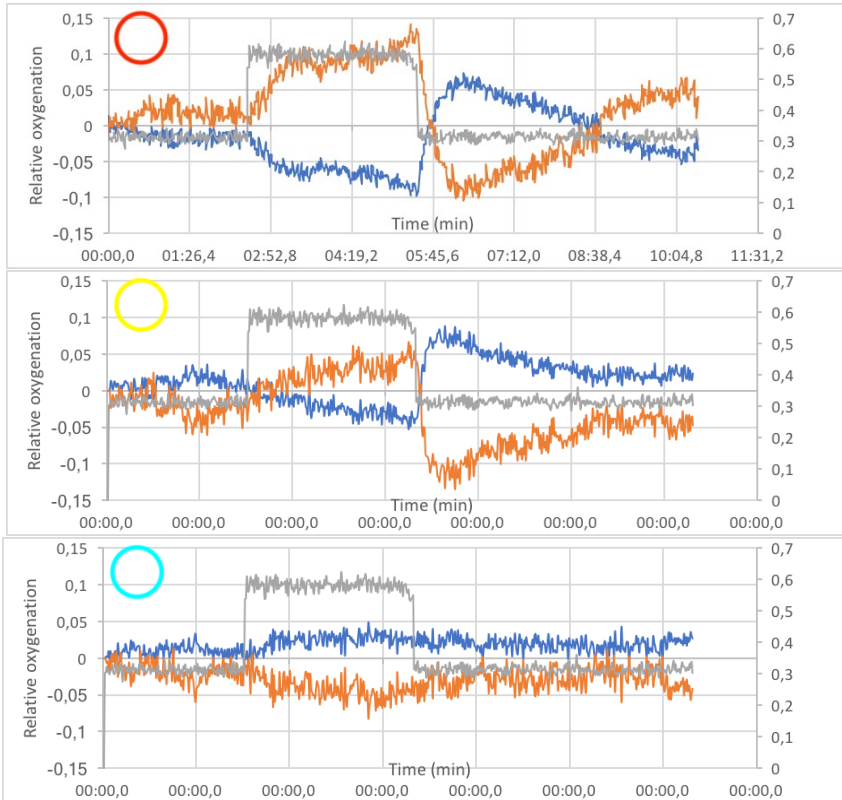


Figure 5. The first graph is a plot of the average estimated oxygen concentration from the finger marked with the red circle in Figure 4. Secondly is the averaged estimated oxygen concentration from the yellow circle back side of the palm and closest to the INVOS measurements. Third plot indicates the reference measurement on the un-occluded hand average area is the cyan circle.

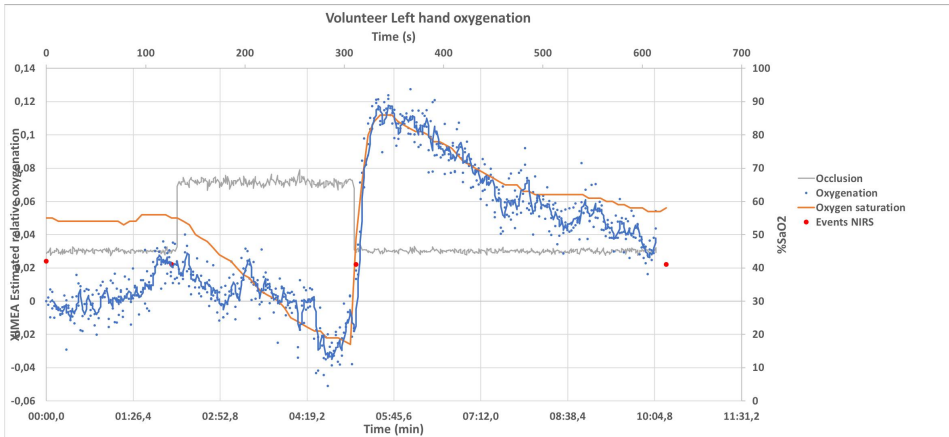


Figure 6. Plot of INVOS oxygenation results (orange solid line) compared to NIR SFA imaging system results (blue line). The results from the NIR SFA imaging system are plotted with a moving average of 4 values represented by the solid line.

the INVOS system was observed with some measurement showing better agreement between the two measurement system than others. A second lightsource was also tested and showed the same trends, but in some patient that second halogen lamp interfered with the ground truth measurements of the INVOS system and therefore is not reported here. In the next section the obtained results and limitations will be discussed.

4. DISCUSSION

The goal of this study was to show the potential of the NIR SFA camera as a real time spatial oxygenation measurement tool. Results obtained are promising in regards to the expected oxygenation behaviour in healthy volunteers. In order to apply these techniques in a less controlled clinical setup with unwell patients the method of measurement has to be further improved.

Even though the relative oxygenation curve during the occlusion followed the trends as measured with our reference, the estimation does not provide absolute measurements. Therefore, the curves were aligned regarding the maximum oxygenation present in both signals, since the value range of the oxygen estimations is an arbitrary scale and only shows dynamic and relative changes over time. The oxygenation estimation should be calibrated in order to provide full absolute oxygenation values in a spatially resolved manner. Agreement between these two curves, especially in the regions of "reperfusion" and "back to baseline" is of clinical importance, since they contain information about the arterial health of a patient. The alignment of the curves is arbitrary and could have also be done at the baseline level in the beginning of the measurement. But especially the regions at the start of occlusion and during occlusion and after occlusion are important for clinical use of this data. The general trends especially in these areas can be considered similar. Figure 7 shows the areas which are especially interesting for clinical readings of these occlusion measurements. This indicates that both measurement systems sensed a similar underlying change in oxygenation of the blood present over time. Another factor which has to be taken into account for differences measured between the INVOS system and the NIR SFA camera system is the location of measurement. The increased amount of melanin on the back of the hand can negatively influence the measurements. Due to the fact that we were measuring with the NIR SFA camera the higher absorption of superficial melanin should be minimal. The underlying vessel structures on the other hand can also influence the measurement results. Different locations have shown to be perfused differently, which makes the direct comparison challenging. In the future a direct comparison between the NIR SFA camera and the VIS SFA camera (also distributed by XIMEA) could be done in order to further investigate the difference of sensing superficial oxygenation and deeper blood delivery.

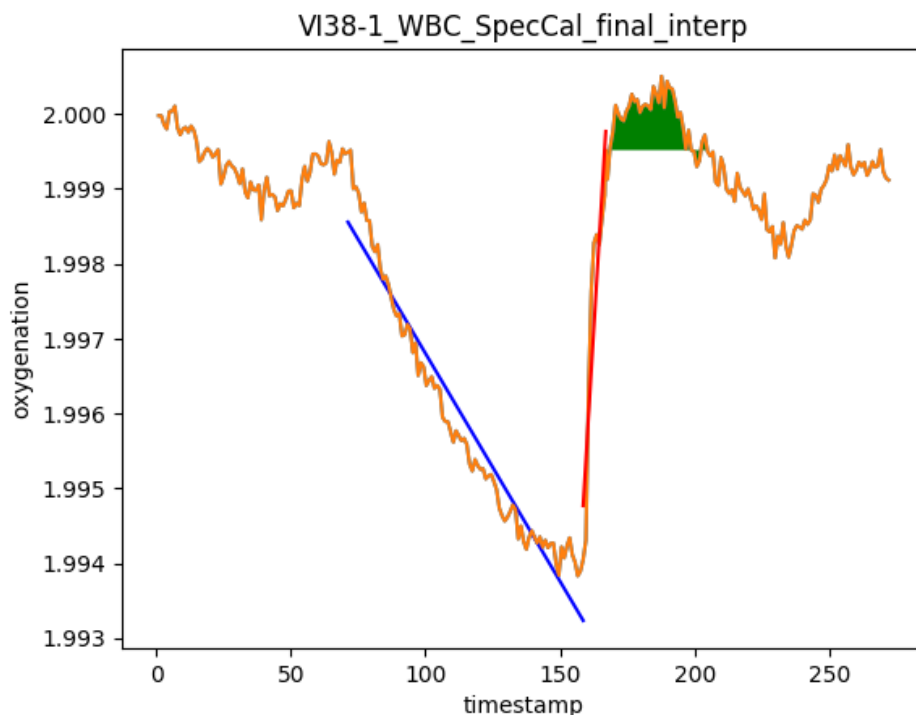


Figure 7. especially the area under the curve, the desaturation slope and the resaturation slope (in this figure linear interpolations in specific areas of the oxygenation curve) are of clinical value. In a planned publication we will discuss these further and show the results obtained with the visual range camera

Furthermore, special attention should be taken for the spectral correction and the influence of the method chosen should be further studied this will be part of a future publication focussing on the effect of the spectral correction on the final results. A more robust oxygenation estimation could be performed and the final implementation in real time should be evaluated. Adjustment to guarantee full real time processing should be straight forward with the chosen approach. Furthermore, as shown in Figure 7 a numerical comparison between these marked key features of the two oxygenation results is planned in another publication. These key features of the oxygenation curves provide useful information about the arterial health. This study has limitations including among others the selection of volunteers. The sample size and diversity among the volunteers measured should be improved in order to show robustness against different skin types and other intra volunteer differences. Furthermore, all the volunteers were healthy and patients in care could affect the measurements outcome, due to lower blood pressure. Robustness to these special conditions has to be shown for a clinical application of these methods. Oxygenation estimation could be further improved with additional wavelength to reduce noise and a real time implementation should be feasible. Regardless of the shortcomings mentioned using NIR SFA imaging for spatially resolved oxygenation measurement shows potential for clinical applications.

5. CONCLUSION

This research focussed on a method to estimate oxygenation of in vivo tissue using a near infrared spatial filter array camera with low computationally demands. The proposed method shows good agreement with expectations according to the occlusion protocols and agreement with our reference INVOS measurement system especially in

clinically relevant aspects of the oxygenation curves. It can be easily adapted to be performed in real time and provides a relative spatial oxygenation map. In order to ensure feasibility for a clinical setup several improvements for the approach are discussed in the previous section.

Acknowledgment

This research has been supported by the Research Council of Norway through project no. 247689 IQ-MED: Image Quality enhancement in MEDical diagnosis, monitoring and treatment.

REFERENCES

- [1] MacKinnon, N., Vasefi, F., Gussakovsky, E., Bearman, G., Chave, R., and Farkas, D. L., "In vivo skin chromophore mapping using a multimode imaging dermoscope (SkinSpec)," *SPIE BiOS* **8587**, 85870U–85870U–13 (Feb. 2013).
- [2] Randeberg, L. L., Eivind L. P. Larsen, and Svaasand, L. O., "Hyperspectral imaging of blood perfusion and chromophore distribution in skin," *Proc. SPIE BiOS: Biomedical Optics* **7161**, 71610C–71610C–12, International Society for Optics and Photonics (Feb. 2009).
- [3] Huang, J., *Multispectral imaging of skin oxygenation*, PhD thesis, The Ohio State University (2013).
- [4] Lu, G. and Fei, B., "Medical hyperspectral imaging: a review," *Journal of Biomedical Optics* **19**, 010901–010924 (Jan. 2014).
- [5] Sowa, M. G., Leonardi, L., Payette, J. R., Cross, K. M., Gomez, M., and Fish, J., "Classification of burn injuries using near-infrared spectroscopy," *Journal of Biomedical Optics* **11**, 11 – 11 – 6 (2006).
- [6] Spigulis, J., Rubins, U., Kviesis-Kipge, E., and Rubenis, O., "SkImager: a concept device for in-vivoskin assessment by multimodal imaging," *Proceedings of the Estonian Academy of Sciences* **63**(3), 301–308 (2014).
- [7] Ferguson-Pell, M. and Haggisawa, S., "An empirical technique to compensate for melanin when monitoring skin microcirculation using reflectance spectrophotometry," *Medical Engineering & Physics* **17**(2), 104–110 (1995).
- [8] Gioux, S., Mazhar, A., Lee, B. T., Lin, S. J., Tobias, A. M., Cuccia, D. J., Stockdale, A., Oketokoun, R., Ashitate, Y., Kelly, E., Weinmann, M., Durr, N. J., Moffitt, L. A., Durkin, A. J., Tromberg, B. J., and Frangioni, J. V., "First-in-human pilot study of a spatial frequency domain oxygenation imaging system," *Journal of Biomedical Optics* **16**, 086015–086015–10 (Aug. 2011).
- [9] Klaessens, J. H. G. M., Noordmans, H. J., de Roode, R., and Verdaasdonk, R. M., "Non-invasive skin oxygenation imaging using a multi-spectral imaging system, Effectiveness of different concentration algorithms applied on human skin," in [*World Congress on Medical Physics and Biomedical Engineering, September 7 - 12, 2009, Munich, Germany*], 725–728, Springer Berlin Heidelberg, Berlin, Heidelberg (2009).
- [10] Klaessens, J. H. G. M., Landman, M., de Roode, R., Noordmans, H. J., and Verdaasdonk, R. M., "Thermographic and oxygenation imaging system for non-contact skin measurements to determine the effects of regional block anesthesia," *Proc.SPIE* **7548**, 7548 – 7548 – 11 (2010).
- [11] Klaessens, J. H. G. M., De Roode, R., Verdaasdonk, R. M., and Noordmans, H. J., "Hyperspectral imaging system for imaging o₂hb and h₁hb concentration changes in tissue for various clinical applications," *Proc.SPIE* **7890**, 7890 – 7890 – 10 (2011).
- [12] Delpy, D. T., Cope, M., van der Zee, P., Arridge, S., Wray, S., and Wyatt, J., "Estimation of optical pathlength through tissue from direct time of flight measurement," *Physics in Medicine Biology* **33**(12), 1433 (1988).
- [13] Nishidate, I., Maeda, T., Niizeki, K., and Aizu, Y., "Estimation of Melanin and Hemoglobin Using Spectral Reflectance Images Reconstructed from a Digital RGB Image by the Wiener Estimation Method," *Sensors* **13**, 7902–7915 (June 2013).

An Evaluation Framework for Spectral Filter Array Cameras to Optimize Skin Diagnosis

Paper E

This chapter is a reprint of the publication:

Jacob R. Bauer; Jean-Baptiste Thomas; Jon Y. Hardeberg and Rudolf M. Verdaasdonk; "An Evaluation Framework for Spectral Filter Array Cameras to Optimize Skin Diagnosis" *Sensors* 2019, 19(21), 4805.

Article

An Evaluation Framework for Spectral Filter Array Cameras to Optimize Skin Diagnosis

Jacob Renzo Bauer ^{1,*} , Jean-Baptiste Thomas ¹, Jon Yngve Hardeberg ¹  and Rudolf M. Verdaasdonk ²

¹ The Norwegian Colour and Visual Computing Laboratory, Norwegian University of Science and Technology (NTNU), 2815 Gjøvik, Norway; jean.b.thomas@ntnu.no (J.-B.T.); jon.hardeberg@ntnu.no (J.Y.H.)

² Biomedical Photonics and Imaging group, Faculty of Science and Technology, University of Twente, 7522NB Enschede, The Netherlands; r.m.verdaasdonk@utwente.nl

* Correspondence: jacob.bauer@ntnu.no

Received: 10 September 2019; Accepted: 1 November 2019; Published: 5 November 2019

Abstract: Comparing and selecting an adequate spectral filter array (SFA) camera is application-specific and usually requires extensive prior measurements. An evaluation framework for SFA cameras is proposed and three cameras are tested in the context of skin analysis. The proposed framework does not require application-specific measurements and spectral sensitivities together with the number of bands are the main focus. An optical model of skin is used to generate a specialized training set to improve spectral reconstruction. The quantitative comparison of the cameras is based on reconstruction of measured skin spectra, colorimetric accuracy, and oxygenation level estimation differences. Specific spectral sensitivity shapes influence the results directly and a 9-channel camera performed best regarding the spectral reconstruction metrics. Sensitivities at key wavelengths influence the performance of oxygenation level estimation the strongest. The proposed framework allows to compare spectral filter array cameras and can guide their application-specific development.

Keywords: spectral filter array; multispectral imaging; biomedical optics; image quality; reflectance spectroscopy; oxygenation; tissue optics

1. Introduction

Spectral filter array (SFA) cameras are a new single-shot spectral imaging technology [1], which is gaining popularity in different fields of research [2]. The light entering the camera is filtered with narrow spectral bandpass filters on each pixel or subpixel. Spatial decomposition of the spectral signal allows capturing of all spectral bands at the same instance.

Prototypes have been proposed in academia [3] and commercial models are now available including the XIMEA xiSpec camera [4,5] and Silios technologies SFA camera [6]. With increased adoption and commercial availability of SFA cameras, it is important to analyze parameters contributing to image quality parameters of these cameras and provide tools to guide further development for specific applications.

Image quality performance of cameras for close range imaging is a broad field of research [7–9] covering many different aspects including: spatial resolution [10–12], spectral or color accuracy [3,13,14], reproducibility, noise behavior [15], optical distortions and post-processing steps. The required accuracy of spectral reconstructions, number of channels and wavelength of interest are application dependent and should be evaluated in the context of specific applications. If SFAs combine accurate spectral reconstruction with real-time acquisition speed and ease of use, they could potentially be a powerful new imaging modality for the medical field. Digital imaging is already widely adopted for skin imaging, which could benefit from additional spectral information [16–20]. Small color variations in the skin can carry relevant information for physicians. There is a need for

more reliable and quantitative methods to measure physiologic parameters of patients in non-contact. SFA cameras could combine non-contact monitoring of vital functions and diagnosis of diseased skin tissue in real time [21–28]. In particular, dynamic processes such as oxygenation would highly benefit from spectral and spatially resolved images in real time [27,29–32].

Previous work by Preece and Claridge [33] has investigated optimal filter sensitivities for a three-channel system for skin diagnosis. An extensive hardware focused analysis of spectral imagers for biomedical applications is provided by Gutiérrez-Gutiérrez et al. [34]. The main focus of their work was the technical limitations including acquisition speed, efficiency, object plane curvature, spatial resolution, distortions, and noise. They emphasized an imaging system for biomedical applications should be selected after thorough testing of these parameters. A comprehensive emulation framework has been proposed by Saager et al. [35] giving an overview of the performance of different spectral imagers including a Xispec SFA camera and an RGB sensor a burn wound mouse model and photoaging experiment. High-resolution spectral measurements were performed using a spatial frequency domain spectroscopy (SFDS) system. In the computer graphic domain with Jimenez et al. [36] and Iglesias-Guitian et al. [37] described physically based skin appearance models to show color changes due to emotions or ageing. The same models can be used as to generate skin reflectance training sets.

The aim of this study is the development and testing of a framework for comparison of SFA cameras for spectral reconstruction, skin imaging, and oxygenation level estimation without prior patient measurements. A generated specialized training set is quantified for spectral reconstruction.

This framework could be considered prior to the hardware focused selection by Gutiérrez-Gutiérrez et al. [34] and provides a simplified measurement free alternative to the method proposed by Saager et al. [35]. The framework could also be applied as a guide for the development of application-specific SFA cameras.

Three aims of study can be formulated as:

- comparison framework of spectral filter array cameras for skin imaging and medical diagnosis
- illustrate the impact of spectral reflectance reconstruction using a specialized training set for SFA camera applications in skin imaging.
- recommendation of commercially available SFA cameras for monitoring of vital functions and diagnosis.

2. The Proposed Framework

The proposed framework has three main elements: (1) calculation of a spectral reconstruction matrix, (2) simulated sensor responses and (3) an evaluation block. It is shown in Figure 1 and follows the concepts of a spectral filter array processing pipeline proposed by Lapray et al. [38].

As a first part, a spectral reconstruction is performed to estimate the full spectra using the limited number of SFA bands providing a measure of the performance of the different cameras independent of applications. In addition, the estimated spectra are then analyzed regarding their accuracy for oxygenation level estimation being an example for a specific application. Three SFA cameras, one prototypical, two commercially available and an RGB camera are evaluated. The impact of gaussian spectral bands (GSB) is tested by simulating sensor sensitivities with gaussian shapes for each of the SFA cameras channels.

A set of (10,000) [39] skin reflectances is generated using a Monte Carlo skin model and compared to a Munsell reflectance patch database [40,41] for training the spectral reconstruction. A database of spectral measurements of skin reflectances (100 measurements) [42] is used for testing the spectral reflectance reconstruction. The spectral reconstruction accuracy is compared numerically using Root Mean Square Error (RMSE) and ΔE_{00} color differences [43]. Differences in estimated oxygenation levels are numerically compared using a proposed metric. Spatial aspects are not considered in this study since the standard clinical measurement of oxygenation levels are usually averaged over a small area and the skin simulation is only considering homogeneous tissue over the simulated surface.

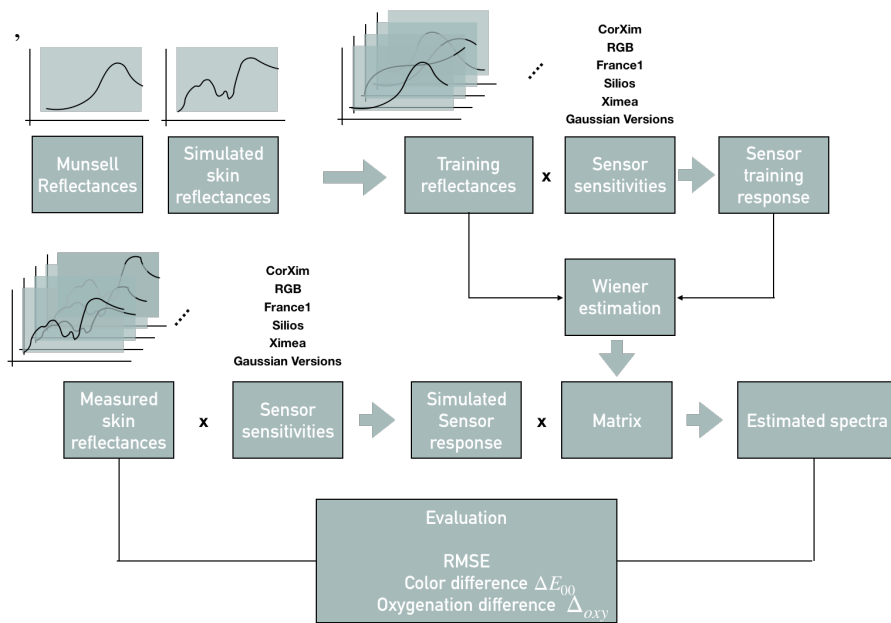


Figure 1. Framework, including training set, testing set, sensor sensitivities, reconstructed spectra and the evaluation according to RMSE, ΔE_{00} , ΔO_{xy} .

3. Prerequisites

For full spectral reconstruction simulated sensor responses are needed. The spectral reconstruction accuracy needs to be evaluated regarding spectral accuracy and in relation to specific applications. The framework could be applied to any channel-based spectral imager with known spectral sensitivities. For comparing specific spectral imagers, sensor sensitivities, training and test data and evaluation metrics must be chosen.

3.1. Spectral Imaging Model and Spectral Reconstruction

Spectral reconstruction is a useful estimation technique to estimate full spectra from a limited number of bands. The wavelengths of interest might also be unknown prior to the practical applications. It allows comparison of spectral cameras with different sensitivity peaks in a common space.

The spectral reconstruction is based on the inversion of a commonly known imaging model, which can be described with the equation:

$$P_i = \int_{\lambda} E(\lambda) R_j(\lambda) Q_i(\lambda) d\lambda \quad (1)$$

where P_i is the channel response of the i^{th} channel of the sensor. $E(\lambda)$ is the illumination spectral power distribution (SPD) per wavelength, $R_j(\lambda)$ is the spectral reflectance of sample j and $Q_i(\lambda)$ describes the spectral sensitivity of the i^{th} channel of the sensor. Noise can be described as an additive constant to each channel.

Two simplification have been applied to the imaging model for this study. Noise per channel has not been considered and illumination has been assumed to be of equi-energy. Both variables influence the performance of the cameras in a real setup. Specific light-source power distributions might favor a particular camera hindering the comparability. A mathematical description of noise might not be an adequate descriptions of practical noise behavior of a physical camera. A chosen noise model could also favor one camera for the comparison.

This model can be inverted for spectral reconstruction, by estimating $R_j(\lambda)$. Several different techniques have been proposed including the pseudo-inverse method [44] (linear least-square fitting) or linear least-square fitting in lower-dimensional space (Imai–Berns method) [45]. For this study, a commonly used spectral reconstruction technique known as Wiener estimation [45–50] is applied. Before inverting Equation (1) it is rewritten into discrete formulation:

$$P_i = \sum_{k=0}^N E(\lambda_k) R_j(\lambda_k) Q_i(\lambda_k) \quad (2)$$

N is the number of spectral bands depending on the wavelength range and spectral resolution, in this case, $\lambda \in [400, 700]$ with a sampling rate of 2 nm steps and $N = 151$. For all j reflectances of the training set, the channels i of the sensor and k distinct spectral bands, we can write in matrix form:

$$\mathbf{p} = \mathbf{R}\mathbf{E}\mathbf{Q} \quad (3)$$

\mathbf{p} is of $J \times I$ dimensionality with J spectral samples and I channels, \mathbf{R} of $J \times N$, \mathbf{E} of $N \times N$ (diagonal matrix) and \mathbf{Q} of $N \times I$ where N is 151 different wavelengths for this research. This is inverted according to the Wiener estimation method [45–47], in this study the implementation by Nishidate et al. [49] is followed and describes a reconstructed reflectance with:

$$\tilde{\mathbf{r}} = \mathbf{W}\mathbf{p}, \quad (4)$$

where \mathbf{W} describes the Wiener estimation matrix, $\tilde{\mathbf{r}}$ the resulting vector of reflectance estimation or reconstruction and \mathbf{p} the vector of sensor responses for each channel. The Wiener matrix is calculated by minimizing the square error of reconstructed and given reflectance for a training set of reflectances.

This matrix needs to be calculated for each camera and training set combination. Sensor responses can be simulated by multiplying the sensor sensitivities and the reflectance spectrum of an object. Spectral reconstructions can then be performed given this sensor response and the pre-trained Wiener estimation matrix \mathbf{W} .

3.2. Sensors

Most SFA sensors are based on micro interference filters (often Fabry–Pérot interference) that can be simulated with GSB as shown by Lapray et al. [51] with width and shape as main parameters [52,53].

The framework enables the comparison of any multi-band sensors with known spectral sensitivities or optimize the design of ‘virtual’ SFA cameras for specific applications. SFA cameras have a limited number of wavelength bands divided over the sensor. The design of SFA sensors will be a trade-off between spectral resolution and spectral range covered. A narrower spectral band per filter will improve the spectral resolution, but would require more spectral bands to cover the whole sensitivity. Broader sensitivities on the other hand, reduce the spectral resolution, but require less filters and avoid (“holes”) in the covered spectrum. However, for specific applications only a few primary wavelengths are needed as in case of oxygenation estimation.

In this study, we included simulated GSB they were chosen with a full width half max that make them comparable with their real sensor sensitivities of the cameras tested.

3.3. Training and Test Set

The training set will contribute to the accuracy of spectral reconstruction using Wiener estimation which calculates a transformation matrix that translates SFA responses to a full spectrum. This transformation matrix should minimize the difference between the reference spectrum and a reconstructed spectrum. The reference spectrum used to determine this matrix is called the training set.

For training two sets were compared to see the impact on the reconstruction accuracy for the different cameras: The Munsell database is used as a standard for color testing and the second training

set was a generated for skin color simulation using a wide array of skin optical properties. The skin simulation (training set) assumes an equi-energy illumination and therefore represents illumination corrected skin spectra. Both sets are normalized using a feature scaling so that all values cover a range from 0 to 1. A more detailed description of this skin database follows in the experimental setup. For the validation of the spectral reconstruction another set based on skin reflectances was used. These skin reflectances (test set) are measured using a spectrophotometer and illumination corrected as described in [42].

The three sets are illustrated in Figure 2. This Figure allows comparison of the area covered by all sets and highlights three reflectances for each dataset. It includes the database of 100 measured skin reflectances [42], 10000 Monte Carlo simulated reflectances and the Munsell reflectances color patches [40,41].

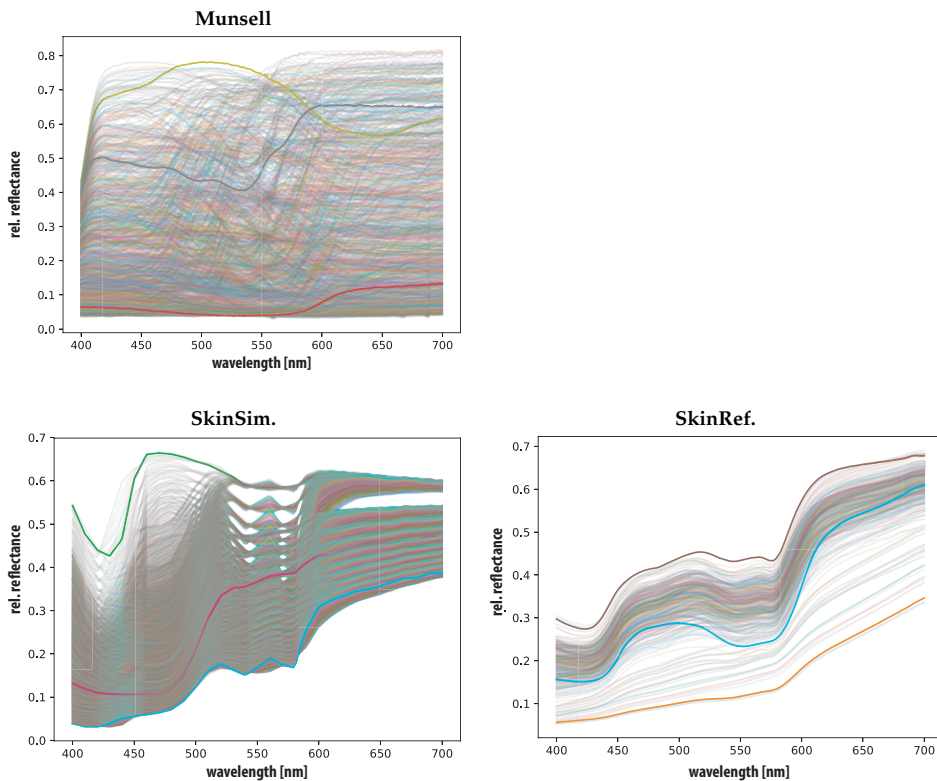


Figure 2. Measured Munsell reflectances [40] (munsell), measured skin reflectances [42] (SkinRef), simulated skin reflectances (SkinSim). Three reflectances highlighted for visibility in each set.

3.4. Evaluation Metrics

The validation of the proposed framework can be tested by applying it to a specific clinical application, oxygen level estimation. This should show which spectral filter array camera is most suitable for this specific application. Three different evaluation metrics are considered. Two of the metrics focus on spectral reconstruction quality regarding shape and color. The third metric is application-specific and in this case quantifies the ability of each camera to estimate oxygen levels, it will be discussed in detail in the next section.

The first metric calculates the color difference ΔE_{00} [43] of two spectra which is the distance between two colors in the human perceptual colorspace. Each spectrum is converted into color

coordinates using the, D65 illumination for the calculations, and CIE 1931 2 Degree Standard Observer color-matching functions. A ΔE_{00} of around 2 is a just noticeable color difference for a human observer.

The second spectral reconstruction metric is the root mean square error (RMSE) between the reference spectrum and a reconstructed spectrum. There is no need to include the Goodness of fit coefficient (GFC) or the angular error, since previous studies [54] have shown that these correlate strongly with the RMSE.

3.5. Application-Specific Metric and Oxygenation Level Estimation

The third metric is a validation of the oxygenation level estimations. This parameter can be approximated through calculations using the reflectance spectrum of skin. The reflectance spectrum of skin is the result of concentrations of particular chromophores present in the skin. The ratio between oxygenated and deoxygenated hemoglobin reflects the relative oxygenation level in the skin and is an important parameter for diagnostics. Hemoglobin occurs in different forms but only these two are relevant for oxygenation. Different methods have been proposed to estimate oxygenation levels from particular wavelengths [27,29,49,55].

For this study, the estimation uses a multiple regression method described by Nishidate et al. [49]. A fast way of estimating absorbance $A(\lambda)$ from reflectance assumes the Lambert-Beer law:

$$A(\lambda) = -\log_{10}R(\lambda) \quad (5)$$

According to the simplified Lambert-Beer law the total absorbance of skin tissue can be described with:

$$A(\lambda) = C_m l_e(\lambda, C_m) \varepsilon_m(\lambda) + C_{bi} l_d(\lambda, C_{bi}) \varepsilon_{bi}(\lambda) + C_{ob} l_d(\lambda, C_{ob}, C_{db}) \varepsilon_{ob}(\lambda) + C_{db} l_d(\lambda, C_{ob}, C_{db}) \varepsilon_{db}(\lambda), \quad (6)$$

where $\varepsilon_m, \varepsilon_b, \varepsilon_{ob}, \varepsilon_{db}$ describe the molar extinction coefficients of melanin, bilirubin, oxygenated and deoxygenated hemoglobin and C_m, C_b, C_{ob}, C_{db} describe the concentration of each specific chromophore. l_e describes the mean optical path length for epidermis, l_d for dermis and $D(\lambda)$ describes the attenuation due to scattering these values are taken from literature. This equation can be solved by multiple regression analysis and is therefore reformulated to:

$$\begin{aligned} A(\lambda_1) &= c_m \varepsilon_m(\lambda_1) + c_{bi} \varepsilon_{bi}(\lambda_1) + c_{ob} \varepsilon_{ob}(\lambda_1) + c_{db} \varepsilon_{db}(\lambda_1) \\ A(\lambda_2) &= c_m \varepsilon_m(\lambda_2) + c_{bi} \varepsilon_{bi}(\lambda_2) + c_{ob} \varepsilon_{ob}(\lambda_2) + c_{db} \varepsilon_{db}(\lambda_2) \\ A(\lambda_3) &= c_m \varepsilon_m(\lambda_3) + c_{bi} \varepsilon_{bi}(\lambda_3) + c_{ob} \varepsilon_{ob}(\lambda_3) + c_{db} \varepsilon_{db}(\lambda_3) \\ &\vdots \\ A(\lambda_n) &= c_m \varepsilon_m(\lambda_n) + c_{bi} \varepsilon_{bi}(\lambda_n) + c_{ob} \varepsilon_{ob}(\lambda_n) + c_{db} \varepsilon_{db}(\lambda_n), \end{aligned} \quad (7)$$

where c_m, c_b, c_{ob}, c_{db} are closely related to the concentrations of melanin, bilirubin, oxygenated and deoxygenated blood and represent the unit-less contribution of each extinction coefficient to the total absorbance A . Any number of wavelengths can be used to calculate the absorbances. Reflectance spectra can be converted to absorbance spectra according to Equation (5) and then used with the following equation. The calculation of the concentration of any chromophore can then be formulated in matrix notation as:

$$\begin{aligned} \mathbf{a} &= \boldsymbol{\varepsilon} \mathbf{c} \\ \mathbf{c} &= \boldsymbol{\varepsilon}^{-1} \mathbf{a} \end{aligned} \quad (8)$$

Finally, oxygen saturation can be calculated with:

$$S_{oxy} = \frac{C_{ob}}{C_{ob} + C_{db}} \quad (9)$$

Even though a simplification of the physical light skin interactions, methods based on these principles have been used for oxygenation level estimation [49,56–58]. This approach allows rapid calculation of tissue parameters with low computational complexity. It is assumed that most other chromophores are constant over time. The oxygenation of blood is not constant, due to oxygen consumption by tissue. According to Equation (9) oxygenation level estimation is calculated using both the reflectance spectra and reconstructed spectra. The Euclidean distance between the two resulting oxygenation level estimation values is then calculated and used as a quality metric to judge the reconstruction accuracy with:

$$\Delta Oxy = | S_{oxy1} - S_{oxy2} | \quad (10)$$

4. Experimental Setup

This section will be discussing the concrete choices of sensors, training and test data, and finally, summarize the approach. A new database of simulated skin spectra is also created and described in detail in this section.

4.1. Sensors

Five cameras are investigated the Sinarback 54 RGB camera (RGB) as representative for common three-channel imaging, three spectral filter array cameras are considered, XIMEA xiSpec MQ022HG-IM-SM4X4-VIS [4,5], Silios technologies CMC-C [6] (Silios) and a prototypical device by Thomas et al. [3] (France1). Table 1 provides an overview of their key features and is sorted by the number of bands. The CorXim 'virtual cameras is added, which is the corrected version of the Ximea xispec [4] camera by applying a linear transformation matrix provided by the manufacturer which reduces the effect of secondary transmission peaks in some filter bands [59]. It is considered to be an independent camera to test the impact of such a correction.

Table 1. Features of the included cameras. RGB camera [60], commercially available XIMEA Xispec SFA camera [4,5] (Ximea and CorXim), Silios technologies SFA camera [6] (Silios), and a prototypical device from academia [3] (France1).

Property	RGB	France1	Silios	CorXim	Ximea
spectral bands	3	8	9	10	16
spectral peak range [nm]	480–610	440–850	445–710	465–630	465–630
frame rate [Hz]	60	60	60	170	170
resolution per band	4080 × 5440	160 × 128	426 × 339	512 × 272	512 × 272
size [mm]	38.8 × 50.0	NA	56 × 56 × 22	26 × 26 × 26	26 × 26 × 26

Figures 3 and 4 show the spectral sensitivities of all cameras in the spectral range of (400–700 nm) with a measurement interval of 2 nm steps. All sensitivities are measured and provided by the camera manufacturers and interpolated to this range and measurement interval. Additionally, for each camera a virtual GSB sensor is generated and included in the study. The GSB are generated according to Thomas [52] at each of the sensitivity peaks of each camera (GRGB, GFrance1, GSilios, GCorXim, GXimea). All GSB have a $\sigma = 15$ nm and provide a virtual version of each camera with perfectly shaped narrow band sensitivities.

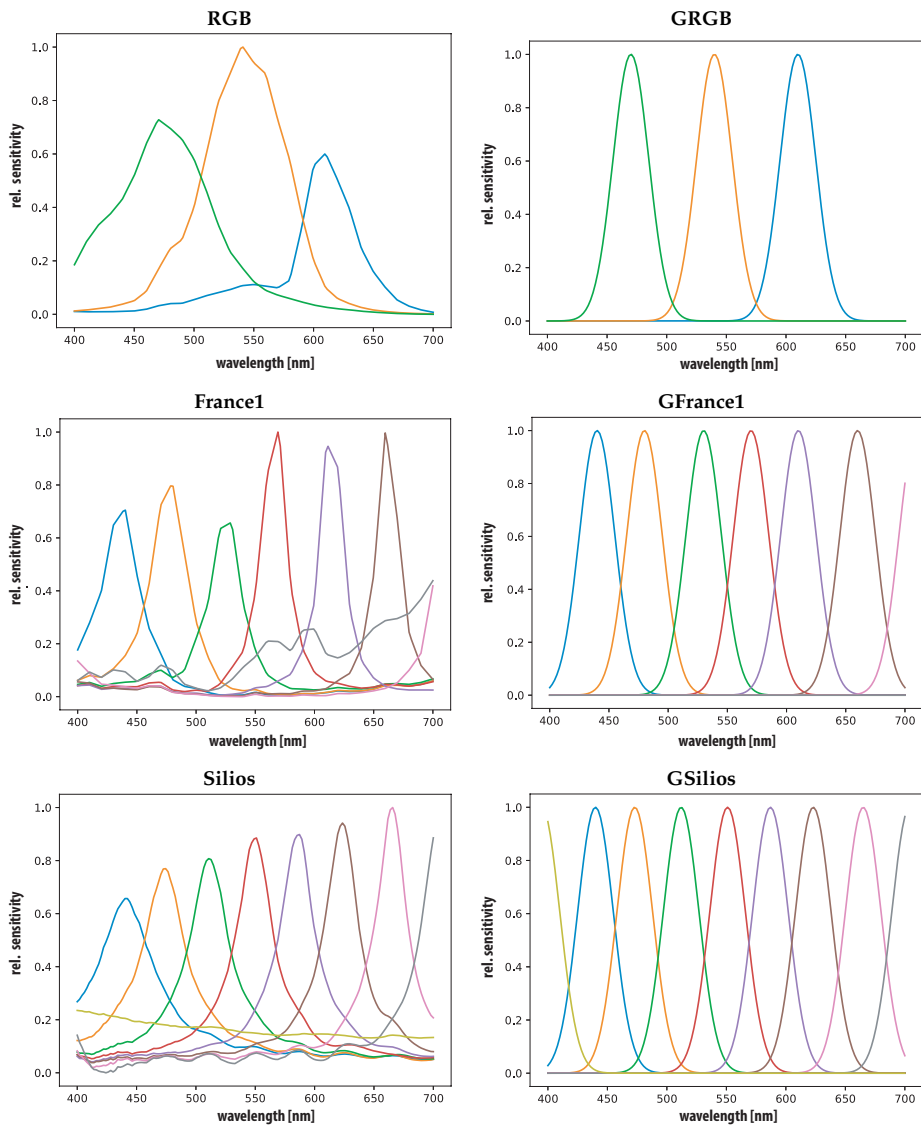


Figure 3. Sensor sensitivities, one RGB camera [60], a prototypical implementation by Thomas et al. [3] (*France1*) and commercially available Silios [6] (*Silios*) (all left) and simulated GSB (*GRGB*, *GFrance1* and *GSilios*) versions (all right).

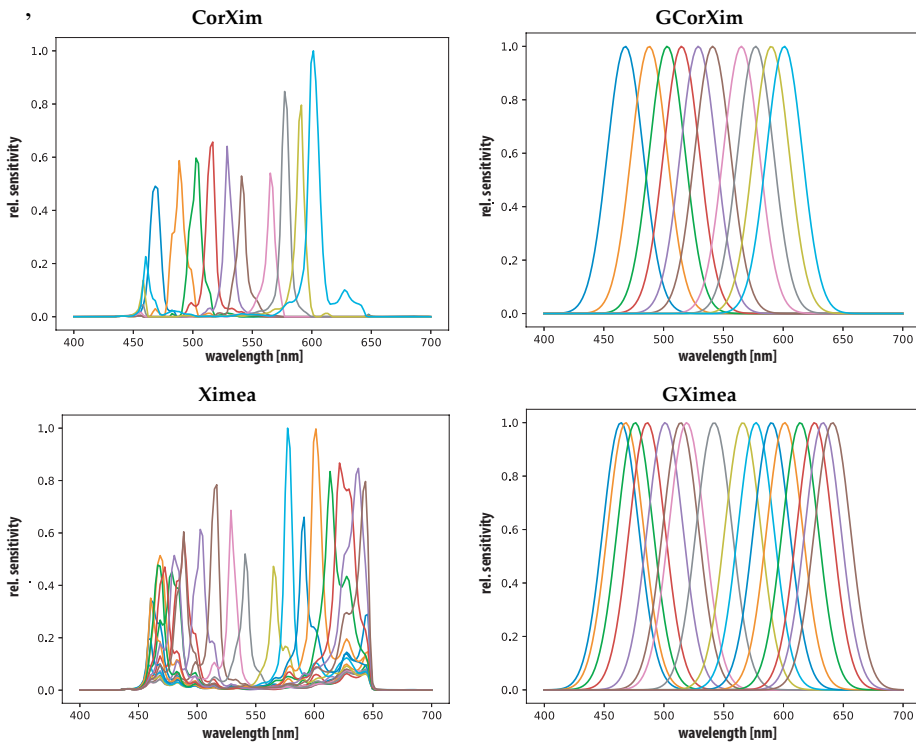


Figure 4. Sensor sensitivities, Ximea xispec [4] (Ximea and CorXimea) (all left) and simulated GSB (GCorXim and GXimea) versions (all right).

4.2. Generating a Training Set

The skin simulations are generated using a modification of the multi-layered Monte Carlo tissue model (MCML) published by Atencio et al. [39]. This code was modified to vary and simulate combinations chromophore concentrations and blood volume fractions [61]. Changing Bilirubin concentration C_{bi} , oxygen saturation S_{oxy} , blood and melanin volume fractions f_{bl} and f_{mel} were changed and 10,000 skin reflectances were calculated.

This simulation environment is based on a three-layer skin model and initially proposed to simulate bilirubin concentration in the skin of the forehead of newborns. The three layers are epidermis, dermis and a bone layer. This model assumes each of the layers as infinite homogenous media with a defined absorption per layer. Scattering is assigned uniformly to both layers. Each layer has different chromophores contributing to its absorption based on the volume fractions of melanin (f_{mel}) blood, (f_{bl}) and bilirubin (f_{bi}). Epidermis contains melanin, dermis contains bilirubin and oxy- deoxygenated hemoglobin. The total absorbance of each of the layers is the sum of the absorbance fractions of chromophores present in that particular layer and defined as μ_a . The chromophore parameters for the Monte Carlo simulation, were chosen to cover the entire range defined by Atencio et al. [39] (see Table 2). For melanin volume fractions of approximately 1% to 6.3% equivalent to fair skin according to Jacques [62].

Table 2. Parameter range for MCML (Monte Carlo modelling of light transport in multi-layered tissues) skin simulation [39,61] resulting in 10,000 different parameter combinations. S_{oxy} is the saturation of oxygenation, f_{bl} and f_{mel} the volume fraction of blood and bilirubin, and C_{bi} describes the bilirubin concentration. Green and red Shadings indicate extreme values of simulation range.

Parameter	Level: 1	2	3	4	5	6	7	8	9	10
S_{oxy}	10%	20%	30%	40%	50%	60%	70%	80%	90%	100%
f_{bl}	0.1%	0.2%	0.3%	0.4%	0.5%	0.6%	0.7%	0.8%	0.9%	1%
C_{bi}	0.0	0.025	0.05	0.075	0.1	0.125	0.15	0.175	0.2	0.225
f_{mel}	0	2%	3%	4%	5%	6%	7%	8%	9%	10%

Each of the chromophore absorption coefficients is modelled from the data provided by Jacques et al. [63]. This μ_a can be seen as analogous to the Absorption A in previous equations, but in the context of defining optical properties of skin it is referred to as μ_a . For the epidermis, the absorption μ_{a_e} only depends on melanin the only chromophore present in this layer with:

$$\mu_{a_{epi}} = f_{mel}\mu_{a_{mel}}(\lambda) \quad (11)$$

The Monte Carlo simulation framework by Atencio et al. mentions specifically that the model needs further testing and verification to simulate darker skin types, therefore even higher melanin volume fractions were not included as parameters for the simulation. To calculate the final absorption of the dermis layer both bilirubin and blood are the main contributors:

$$\mu_{a_{derm}} = f_{bl}\mu_{a_{bl}}(\lambda) + f_{bi}\mu_{a_{bi}}(\lambda) \quad (12)$$

f_{bi} is considered to be constant and the parameter is the concentration of bilirubin as:

$$\mu_{a_{bil}}(\lambda) = \ln(10) \frac{C_{bi}}{P_{Mbi}} \epsilon_{bi}(\lambda), \quad (13)$$

where P_{Mbi} is a constant and $\epsilon_{bi}(\lambda)$ are the literature values for the extinction coefficients for bilirubin [63]. f_{bl} describes the volume fraction of total blood in the dermis layer. The volume fraction parameters for this simulation cover typical values homogeneously distributed blood in the dermis layer [63]. Due to differences in absorbance for oxygenated hemoglobin and deoxygenated hemoglobin $\mu_{a_{blo}}(\lambda)$ is calculated as:

$$\mu_{a_{blo}} = S\mu_{a_{ob}}(\lambda) + (1 - S)\mu_{a_{db}}(\lambda) \quad (14)$$

S describes the oxygen saturation in the blood and is to be estimated. The dataset will be verified in the Results Section 5 using a principle component analysis.

5. Results and Discussion

5.1. Training Set Validation

The first results presented in this study address the skin simulation database and can be seen as an additional verification for using this simulated training set. It is based on principle component analysis (PCA) of the sets included in this research.

The principle components allow representation of the multidimensional set in a lower-dimensional space. If the principle components are calculated for a combined set they represent the orthogonal axes of a space describing the sets. The area covered by the sets plot into this orthogonal space describes the diversity of the particular set. If multiple sets are plot into the same principle component space the difference in diversity and area covered within that PCA space can be analyzed.

The sets are shown along the first two principal components of the combined set in Figure 5. Table 3 shows the resulting principle components of each of the sets and the combined set. The Munsell

set is the most diverse considering its low first principle component. The skin simulation set covers a wider range of reflectances compared to measured skin reflectances. This is represented in a lower first principle component. Physiological parameters cover a wider range than living tissue see Table 2.

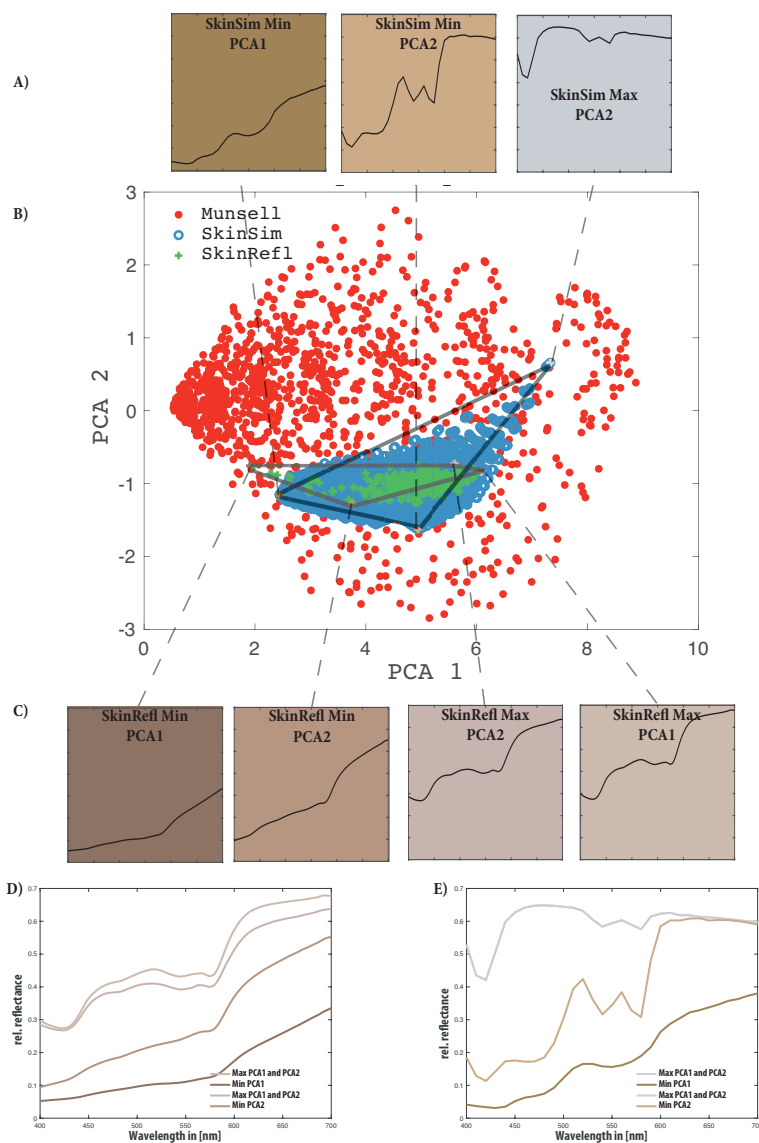


Figure 5. Dimensionality analysis of all sets combined (B) skin simulation (blue), skin reflectance (green) and Munsell reflectances (red). Colored markings for maximum PCA1, minimum PCA1, maximum PCA2, minimum PCA2, for skin simulation and skin reflectance, respectively. Color patch recreation (under D65 light source) of the extreme spectra for the skin simulation (A) and skin reflectance database (C) with minimum PCA 1 and PCA 2 and maximum PCA 1 and PCA 2. Plot of the maximum and minimum spectra for the skin reflectance database (D) and skin simulation database (E) according to PCA analysis.

Table 3. Resulting PCAs for all sets. Variance of each of the sets along the first 4 principle components.

PCA	Munsell	SkinSim	SkinRefl	Combined
1	76.8	87.1	96.0	74.7
2	15.8	7.7	2.1	17.0
3	6.0	4.3	1.5	4.8
4	0.8	0.5	0.2	2.1

In Figure 5 it can be observed that the skin simulation covers all the measured skin reflectances except for a few measurements. This can be ascribed to the limited number of parameters for the simulation, resulting in some measured skin reflectances not being represented within the skin simulation. The skin model is limited to Caucasian fair skin and initially designed for neonatal babies. To further analyze the parameter of the skin simulation, which falls far out of the measured skin reflectance, the extreme curves were plotted.

Figure 5D,E shows these extreme curves of both the skin reflectance and the skin simulation set as marked in Figure 5A. In Table 4 it becomes apparent that the main factor for the simulations is the blood volume parameter. All extreme results according to the PCA analysis have an extreme value for the blood volume. The melanin parameter also contributes to extreme values within the principle component space indicating the strong influence of melanin on the resulting skin spectra. In this principle component space, the bilirubin concentration parameter spreads the distribution of points.

Table 4. Monte Carlo Simulation parameters for the extreme points according to the principle components. Red background items indicate the maximum of their particular parameter, while green background indicate minima for the range of input parameters.

Parameter	Max PCA1 and PCA2	Min PCA1	Min PCA2
StO_2 Saturation	10%	100 %	10%
f_{Blood}	0.1%	1%	1%
$C_{Bilirubin}$	0.225	0.0	0.225
$f_{Melanin}$	0.0 %	10%	10%

Figure 5 also contains sRGB [64] color swatches reproduced under a virtual D65 illumination. These provide a visual impression of the color of the extreme points in the principle component space. They show that the extreme value curves, not included within the skin simulation represent darker skin types and that extreme values of the skin simulation can include physiologically unlikely scenarios of grey skin.

5.2. Spectral Reconstruction

Results for the two spectral reconstruction metrics calculated for each of the four sensors and their simulated GSB versions are shown in Figure 6. Each of the graphs shows mean results and standard deviation of the actual sensor as a circle and the GSB sensor results as a cross. All metrics are calculated with the different training sets (Munsell and skin simulation) for the spectral reconstruction and plotted. The cartesian coordinate system consists of the number of channels on the x-axes and the value for each of the metrics on the y-axes.

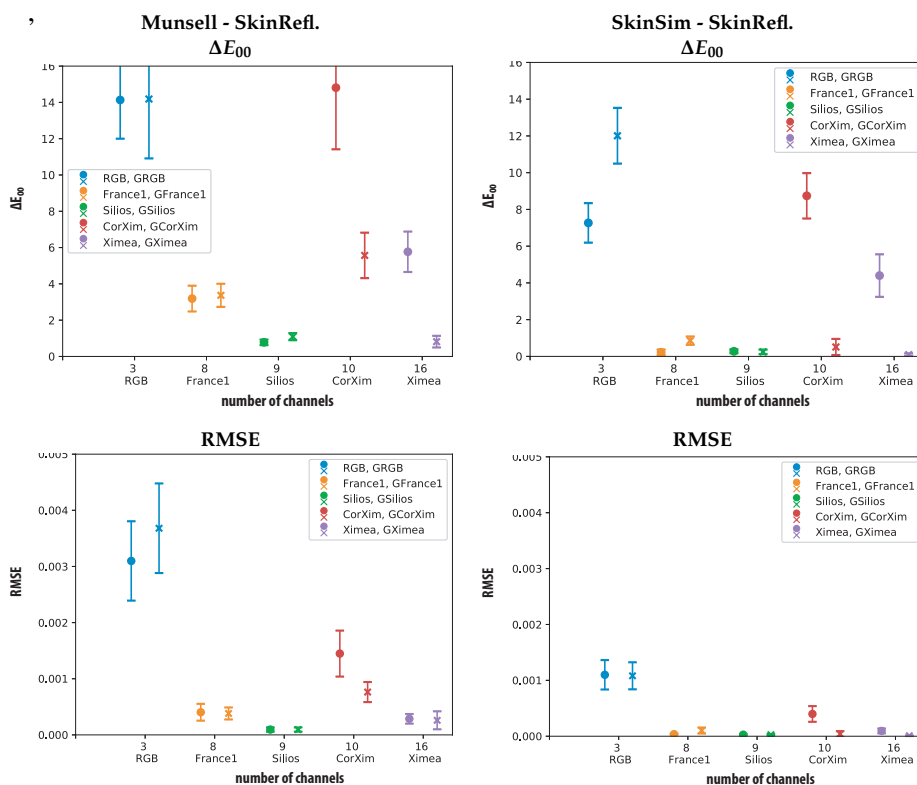


Figure 6. Resulting metrics of ΔE_{00} (D65, CIE 2° 1931) (top) and $RMSE$ calculated between reconstruction and training (bottom). All Sensors, Munsell set (left) and Skin Simulation set (right) as training including standard deviation of the resulting data. For all graphs, the filled “o” represents the original sensor and the “x” represents the GSB.

These plots allow the comparison between the sensors according to the different metrics in two scenarios. It can be observed that the performance in $RMSE$ and ΔE_{00} correspond to each other.

Figure 6 provides a plot of the ΔE_{00} difference between the test reflectances and their reconstruction. Surprisingly, the plots show that the corrected Ximea performs the worst in the case of Munsell patches for training and according to ΔE_{00} . This can be ascribed to the cut of spectral sensitivity imposed by the linear correction transformation. Figure 4 shows the low sensitivity of this sensor at the edges of the chosen spectral range (400 nm to 700 nm).

Figure 7 contains plots of the spectral reflectances ground-truth and reconstructed that are responsible for the highest ΔE_{00} results for the corrected and uncorrected Ximea camera. The plot allows appreciation of the areas of the spectra that cause high ΔE_{00} results. In the case of the corrected Ximea camera spectral regions that have low or zero sensitivity are wrongly reconstructed. This is not surprising but confirms the poorer performance of the corrected Ximea camera in comparison with the uncorrected Ximea camera in the ΔE_{00} and $RMSE$ metric. The more limited spectral coverage of the corrected spectral imager negatively influences the spectral reconstruction ability of this camera.

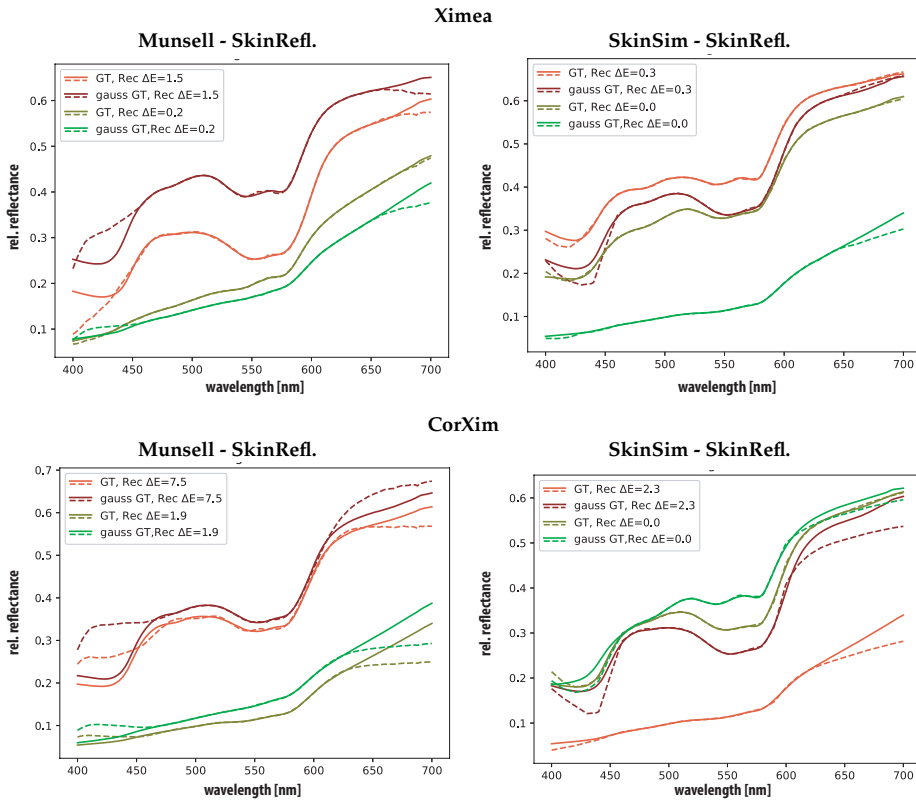


Figure 7. Visualization of worst and best ΔE_{00} results for the uncorrected Ximea (Ximea top) and corrected Ximea (CorXim bottom), Munsell set (left) and Skin simulation (SkinSim) set (right) as training. Each graph includes GSB sensor results, ground-truth in solid lines and estimation with dashed lines.

The second worst performer regarding color differences (Mean $\Delta E_{00} = \sim 14$ and Mean $\Delta E_{00} = \sim 12$) is the RGB camera. Both the low number of channels and their specific overlap in the spectral region seems to influence the estimation accuracy negatively. The lower performance of the GSB version can be ascribed to the low sigma ($\sigma = 15$) of the gaussian filters. In the case of the RGB sensor, the coverage of the spectral range of interested is as seen in Figure 3 not optimal. The spectral distribution shows significant areas of very low spectral sensitivity and negatively influences the spectral reconstructions.

Both corrected (CorXim) and uncorrected Ximea benefit greatly from GSB improving the performance according to the ΔE_{00} metric. For the Silios camera, the GSB only improve the ΔE_{00} performance when using the expert training set as the skin simulation set. One explanation could be the sharp cut off for the GSB resulting from the bands that exceed the spectral range of this analysis. The prototypical sensor *France1* has initially already close to gaussian sensitivities and does not benefit from the GSB.

The RMSE metric shows a similar trend compared to ΔE_{00} . The Ximea camera scores better results regarding the RMSE in comparison with ΔE_{00} . Differences between original sensors and GSB sensors are smaller considering this metric.

Training the Wiener estimation matrix with the proposed specialized skin simulation set results in a more robust reconstruction according to ΔE_{00} and RMSE for all tested cameras. The more general Munsell set lacks skin spectral shapes and is contains two dissimilar spectra in comparison with the

skin test set. The similar shapes and increased number of spectra in the generated specialized database improve the spectral reconstructions.

5.3. Oxygenation Level Estimation

The oxygenation estimations were performed using six wavelengths as proposed by Nishidate et al. (500 nm, 520 nm, 540 nm, 560 nm, 580 nm, 600 nm) and three wavelengths (480 nm, 560 nm, 600 nm) the results are shown in Figure 8.

These two oxygenation metrics show different behavior for all cameras compared to the spectral accuracy metrics. The eight and nine channel cameras (*France1* and *Silios*) perform the worst for the Munsell training case and six wavelengths. This is surprising since these two cameras perform the best according to the spectral reconstruction metrics ΔE_{00} and RMSE. For this case, the performance differences between the GSB sensor and the original sensor are very small. One explanation can be that these key wavelengths all fall into valleys between the sensitivity peaks for the *Silios* and *France1* sensor. The GSB sensors could be affected equally or stronger, due to the relatively small sigma ($\sigma = 15$).

The wavelengths proposed by Nishidate et al. are optimized for an RGB sensor. For the specialized training set, the RGB camera performs the worst. Illustrating that the spectral reconstruction using a specialized training set benefits from narrow spectral channels.

Figure 8 also contains results for the oxygenation metric using three wavelengths (480 nm, 560 nm, 600 nm). It can be observed that the choice of the training set for this configuration influences the different cameras independently. For Munsell patch training, the RGB camera performs the worst and both versions of the Ximea camera the best. Using the specialized training set the differences between all cameras are smaller and the RGB camera still performs worst. The other sensors are less affected by the change of training sets only slightly lowering their oxygenation metric differences when using the specialized training set. For the idealized GSB RGB sensor lower oxygenation metric differences can be observed compared to some of the SFA sensors. This could be ascribed to the wavelength chosen for oxygenation level estimation which all fall well within high sensitivity of the gaussian RGB (GRGB) sensor.

A camera with sensitivity peaks at the wavelength of interest should perform optimally. This can be used if the wavelength of interest are known. None of the investigated cameras has optimal filter sensitivity peaks for oxygenation estimation. Table 5 provides an overview of the statistical results for all sensors, considering the better performing skin simulation training data set.

The proposed specialized training set improved the final oxygenation parameters (estimated with three wavelengths). In the case of six wavelengths the skin training set performs worse than the Munsell set. One explanation is that using six wavelengths includes wavelengths at the outer edges of the considered spectral range. The specialized set provides too little variety for these areas and the diverse Munsell set trains these regions better.

For future work noise should be incorporated into the framework. The chosen wiener estimation method has room to incorporate a noise term into the spectral estimation and the impact of different kind of noise should be studied. The framework also allows simulation and comparison of spectral filter array cameras in different spectral ranges. Near infrared should be considered for future work as it is used in traditional oximetry systems. Furthermore, oxygenation estimation methods that use the full spectra based on inverse Monte Carlo methods should be tested in conjunction with spectral reflectance reconstruction.

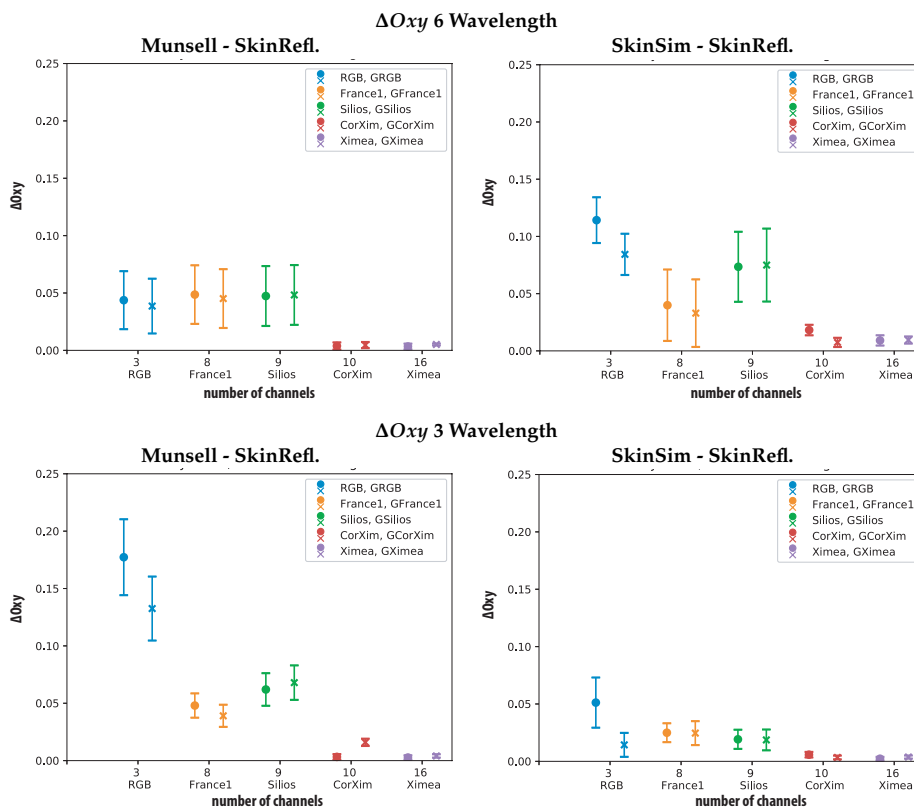


Figure 8. Resulting values for ΔOxy metric calculated using six wavelength (500 nm, 520 nm, 540 nm, 560 nm, 580 nm, 600 nm) (top) and three wavelengths (480 nm, 560 nm, 600 nm) (bottom) for all Sensors. Munsell set (left) as training and Skin Simulation set (right) including standard deviation of the data.

Table 5. Statistical results (minimum, maximum, mean, standard deviation, 98%) for all sensors for ΔE_{00} (top), RMSE (2nd from top), ΔOxy 6wvl (3rd from top) and ΔOxy 3wvl (bottom). All values are based on skin simulation set as training and skin reflectance set as testing.

ΔE_{00}											
Sensor	Min	Max	Mean	Std	98%		Min	Max	Mean	Std	98%
RGB	5.04	11.03	7.27	1.08	9.20	GRGB	8.89	16.76	12.01	1.52	14.87
France1	0.02	0.93	0.22	0.15	0.68	GFrance1	0.40	1.50	0.86	0.23	1.35
Silios	0.04	0.66	0.28	0.11	0.49	GSilios	0.03	0.75	0.25	0.12	0.51
CorXim	5.82	11.99	8.74	1.24	11.50	GCorXim	0.02	2.27	0.51	0.44	2.18
Ximea	0.89	6.81	4.40	1.16	6.38	GXimea	0.00	0.30	0.09	0.07	0.25
RMSE											
Sensor	Min	Max	Mean	Std	98%		Min	Max	Mean	Std	98%
RGB	0.000647	0.002112	0.001099	0.000263	0.001717	GRGB	0.00067	0.00194	0.00108	0.00024	0.00180
France1	0.00001	0.00009	0.00004	0.00001	0.00007	GFrance1	0.00003	0.00037	0.00010	0.00005	0.00022
Silios	0.000003	0.00006	0.00003	0.00001	0.00005	GSilios	0.000003	0.00006	0.00003	0.00001	0.00006
CorXim	0.000184	0.00099	0.00040	0.00014	0.00081	GCorXim	0.000004	0.00028	0.00004	0.00005	0.00026
Ximea	0.000007	0.00028	0.00010	0.00004	0.00020	GXimea	0.000002	0.00003	0.00001	0.00001	0.00003
Oxyg. Metric 6wvl											
Sensor	Min	Max	Mean	Std	98%		Min	Max	Mean	Std	98%
RGB	0.070	0.169	0.114	0.020	0.155	GRGB	0.051	0.125	0.084	0.018	0.119
France1	0.001	0.150	0.040	0.031	0.109	GFrance1	0.0001	0.145	0.033	0.030	0.102
Silios	0.002	0.140	0.073	0.031	0.131	GSilios	0.006	0.151	0.075	0.032	0.134
CorXim	0.001	0.028	0.018	0.005	0.027	GCorXim	0.0002	0.017	0.007	0.004	0.016
Ximea	0.000	0.019	0.009	0.004	0.018	GXimea	0.0002	0.017	0.009	0.003	0.016
Oxyg. Metric 3wvl											
Sensor	Min	Max	Mean	Std	98%		Min	Max	Mean	Std	98%
RGB	0.010	0.132	0.051	0.022	0.090	GRGB	0.0001	0.051	0.014	0.010	0.044
France1	0.001	0.041	0.025	0.008	0.038	GFrance1	0.002	0.048	0.025	0.010	0.043
Silios	0.001	0.043	0.019	0.008	0.035	GSilios	0.001	0.048	0.019	0.009	0.036
CorXim	0.00004	0.011	0.006	0.002	0.010	GCorXim	0.0001	0.008	0.003	0.002	0.007
Ximea	0.001	0.041	0.025	0.008	0.038	GXimea	0.00001	0.007	0.004	0.001	0.006

5.4. Summary and Conclusions

A straightforward framework to evaluate spectral filter array cameras based on spectral sensitivities and publicly available skin and reflectance databases was proposed. It allows to compare and quantify the performance of SFA cameras for medical applications and skin imaging in particular. The framework does not require prior measurements and is based on a readily available skin databases for testing, a proposed generated skin simulation database and sensor sensitivities of the cameras included.

Reconstructing full reflectances from sensor responses allows to comparison and is useful when the application-specific bands of interest are unknown. It can be useful to recreate color images and benefits from a specialized training set. If the bands of interest are known a camera with high sensitivity for those exact bands is advisable. Several observations particular to spectral filter array cameras were made:

- Spectral shapes of the filters should be adapted application-specific
- Careful choice of the spectral bands should be adapted application-specific
- Selecting an optimal training set for spectral reflectances reconstruction improves the results for SFAs with narrow spectral sensitivities
- GSB improve spectral reconstruction considering ΔE_{00} color differences and RMSE
- GSB have a small impact on oxygenation level estimation if the bands are not close to the ideal wavelength for oxygen estimation

The framework has been applied to compare commercially available SFA cameras for skin diagnosis and skin oxygenation level estimation.

The corrected Ximea camera performed the best in terms of oxygenation level estimations. Regarding the spectral reconstruction and ΔE_{00} color difference metrics the Silios camera shows the best results. Recommending it for applications where the specific bands of interest are not known.

SFA cameras hold great potential for monitoring vital functions and medical diagnosis as a non-contact, real-time spectral imaging modality. This framework provides a basis for using spectral filter array cameras effectively for medical applications. It can be used to design spectral filter sensitivities for specific applications by optimizing the wavelength bands and transmission shapes of the filters. It is, however, necessary to verify the findings with experimental data and extend the framework to include spatial aspects.

Author Contributions: Conceptualization, J.R.B., J.-B.T., J.Y.H. and R.M.V.; Data curation, J.R.B.; Formal analysis, J.R.B.; Investigation, J.R.B.; Methodology, J.R.B. and J.-B.T.; Project administration, J.R.B., J.Y.H. and R.M.V.; Resources, J.Y.H. and R.M.V.; Software, J.R.B.; Supervision, J.-B.T., J.Y.H. and R.M.V.; Validation, J.R.B., J.-B.T., J.Y.H. and R.M.V.; Visualization, J.R.B. and J.-B.T.; Writing—original draft, J.R.B.; Writing—review & editing, J.R.B., J.-B.T., J.Y.H. and R.M.V.

Funding: This research has been supported by the Research Council of Norway through project no. 247689 “IQ-MED: Image Quality enhancement in MEDical diagnosis, monitoring and treatment”.

Conflicts of Interest: The authors declare no conflict of interest.

Abbreviations

The following abbreviations are used in this manuscript:

SFA	spectral filter array
GFC	goodness of fit coefficient
RMSE	root mean square error
sRGB	standard RGB
MCML	Monte Carlo modelling of light transport in multi-layered tissues
GSB	gaussian spectral bands

References

1. Lapray, P.J.; Wang, X.; Thomas, J.B.; Gouton, P. Multispectral filter arrays: Recent advances and practical implementation. *Sensors* **2014**, *14*, 21626–21659. [[CrossRef](#)] [[PubMed](#)]
2. Ewerlöf, M.; Larsson, M.; Salerud, E.G. Spatial and temporal skin blood volume and saturation estimation using a multispectral snapshot imaging camera. *Proc. SPIE* **2017**. [[CrossRef](#)]
3. Thomas, J.B.; Lapray, P.J.; Gouton, P.; Clerc, C. Spectral Characterization of a Prototype SFA Camera for Joint Visible and NIR Acquisition. *Sensors* **2016**, *16*, 993. [[CrossRef](#)] [[PubMed](#)]
4. Ximea. Hyperspectral Cameras. 2018. <https://www.ximea.com> (accessed on 2 December 2018).
5. IMEC. Hyperspectral-Imaging. 2018. Available online: <https://www.imec-int.com> (accessed on 2 December 2018).
6. SILIOS. Multispectral-Imaging. 2018. Available online: <https://www.silios.com> (accessed on 2 December 2018).
7. Pedersen, M.; Hardeberg, J.Y.; others. Full-reference image quality metrics: Classification and evaluation. *Found. Trends[®] Comput. Graph. Vis.* **2012**, *7*, 1–80. [[CrossRef](#)]
8. Wang, Z.; Bovik, A.C.; Sheikh, H.R.; Simoncelli, E.P. Image Quality Assessment: From Error Visibility to Structural Similarity. *IEEE Trans. Image Process.* **2004**, *13*, 600–612. [[CrossRef](#)]
9. Chandler, D.M. Seven Challenges in Image Quality Assessment: Past, Present, and Future Research. *ISRN Signal Process.* **2013**, *2013*, 1–53. [[CrossRef](#)]
10. Miao, L.; Qi, H.; Ramanath, R.; Snyder, W.E. Binary tree-based generic demosaicking algorithm for multispectral filter arrays. *IEEE Trans. Image Process.* **2006**, *15*. [[CrossRef](#)]
11. Monno, Y.; Tanaka, M.; Okutomi, M. Multispectral demosaicking using adaptive kernel upsampling. In Proceedings of the 2011 18th IEEE International Conference on Image Processing, Brussels, Belgium, 11–14 September 2011; pp. 3157–3160.
12. Wang, C.; Wang, X.; Hardeberg, J.Y. A Linear Interpolation Algorithm for Spectral Filter Array Demosaicking. In *Image and Signal Processing*; Springer International Publishing: Cham, Switzerland, 2014; pp. 151–160.
13. Wang, X.; Thomas, J.B.; Hardeberg, J.Y.; Gouton, P. A Study on the Impact of Spectral Characteristics of Filters on Multispectral Image Acquisition. In Proceedings of the 12th Congress of the International Colour Association, Newcastle Gateshead, UK, 8–12 July 2013; Volume 4, pp. 1765–1768.
14. Park, C.; Kang, M. Color Restoration of RGBN Multispectral Filter Array Sensor Images Based on Spectral Decomposition. *Sensors* **2016**, *16*, 719. [[CrossRef](#)]
15. Nazari, R.M. Denoising and Demosaicking of Color Images. Ph.D. Thesis, Université d’Ottawa/University of Ottawa, Ottawa, ON, Canada, 2017.
16. Bersha, K.S. Spectral Imaging and Analysis of Human Skin. Master’s Thesis, University of Estern Finland, Joensuu, Finland, 2010.
17. Kuzmina, I.; Diebele, I.; Jakovels, D.; Spigulis, J.; Valeine, L.; Kapostinsh, J.; Berzina, A. Towards noncontact skin melanoma selection by multispectral imaging analysis. *J. Biomed. Opt.* **2011**, *16*, 060502. [[CrossRef](#)]
18. Nishidate, I.; Tanaka, N.; Kawase, T.; Maeda, T.; Yuasa, T.; Aizu, Y.; Yuasa, T.; Niizeki, K. Noninvasive imaging of human skin hemodynamics using a digital red-green-blue camera. *J. Biomed. Opt.* **2011**, *16*, 086012. [[CrossRef](#)]
19. Jakovels, D.; Spigulis, J. RGB imaging device for mapping and monitoring of hemoglobin distribution in skin. *Lith. J. Phys.* **2012**, *52*, 50–54. [[CrossRef](#)]
20. Jakovels, D.; Kuzmina, I.; Berzina, A.; Spigulis, J. RGB imaging system for monitoring of skin vascular malformation’s laser therapy. *Proc. SPIE* **2012**, *8427*, 842737.
21. Kumar, A.; Dhawan, A.P.; Relue, P.; Chaudhuri, P.K. Multi-spectral optical imaging of skin to diagnose malignant melanoma. In Proceedings of the Engineering in Medicine and Biology, Atlanta, GA, USA, 13–16 October 1999; Volume 2, p. 1098.
22. Cotton, S.; Claridge, E.; Hall, P. A skin imaging method based on a colour formation model and its application to the diagnosis of pigmented skin lesions. In Proceedings of the Medical Image Understanding and Analysis, BMVA, Oxford, UK, 19–20th July 1999; pp. 49–52.
23. Tsumura, N.; Kawabuchi, M.; Haneishi, H.; Miyake, Y. Mapping Pigmentation in Human Skin by Multi-Visible-Spectral Imaging by Inverse Optical Scattering Technique. *Color Imaging Conf.* **2000**, *2000*, 81–84.

24. Balas, C.; Themelis, G.; Papadakis, A.; Vasgiouraki, E. A novel hyper-spectral imaging system: Application on in-vivo detection and grading of cervical precancers and of pigmented skin lesions. In Proceedings of the IEEE Computer Society Workshop on Computer Vision Beyond the Visible Spectrum, Kauai, HI, USA, 14 December 2001.
25. Kerekes, J.; Subramanian, N.; Kearney, K.; Schad, N. Spectral imaging of skin: Experimental observations and analyses. *Proc. SPIE* **2006**, *6142*, 61423V.
26. Randeberg, L.L.; Baarstad, I.; Løke, T.; Kaspersen, P.; Svaasand, L.O. Hyperspectral imaging of bruised skin. *Proc. SPIE* **2006**, *6078*. [[CrossRef](#)]
27. Klaessens, J.H.G.M.; Noordmans, H.J.; de Roode, R.; Verdaasdonk, R.M. Non-invasive skin oxygenation imaging using a multi-spectral camera system: Effectiveness of various concentration algorithms applied on human skin. *Proc. SPIE* **2009**, *7174*. [[CrossRef](#)]
28. Spigulis, J.; Jakovels, D.; Rubins, U. Multi-spectral skin imaging by a consumer photo-camera. *Proc. SPIE* **2010**, *7557*. [[CrossRef](#)]
29. Huang, J. Multispectral Imaging of Skin Oxygenation. Ph.D. Thesis, The Ohio State University, Columbus, OH, USA 2013.
30. Poxon, I.; Wilkinson, J.; Herrick, A.; Dickinson, M.; Murray, A. Pilot study to visualise and measure skin tissue oxygenation, erythema, total haemoglobin and melanin content using index maps in healthy controls. *Proc. SPIE* **2014**, *8951*, 89510X.
31. Van Gastel, M.; Stuijk, S.; De Haan, G. New principle for measuring arterial blood oxygenation, enabling motion-robust remote monitoring. *Sci. Rep.* **2016**, *6*, 38609. [[CrossRef](#)]
32. Bauer, J.R.; van Beekum, K.; Klaessens, J.H.G.M.; Noordmans, H.J.; Boer, C.; Hardeberg, J.Y.; Verdaasdonk, R.M. Towards real-time non contact spatial resolved oxygenation monitoring using a multi spectral filter array camera in various light conditions. *Proc. SPIE* **2018**, *10489*. [[CrossRef](#)]
33. Preece, S.J.; Claridge, E. Spectral filter optimization for the recovery of parameters which describe human skin. *IEEE Trans. Pattern Anal. Mach. Intell.* **2004**, *26*, 913–922. [[CrossRef](#)] [[PubMed](#)]
34. Gutiérrez-Gutiérrez, J.; Pardo, A.; Real, E.; López-Higuera, J.; Conde, O.M. Custom Scanning Hyperspectral Imaging System for Biomedical Applications: Modeling, Benchmarking, and Specifications. *Sensors* **2019**, *19*, 1692. [[CrossRef](#)] [[PubMed](#)]
35. Saager, R.B.; Baldado, M.L.; Rowland, R.A.; Kelly, K.M.; Durkin, A.J. Method using in vivo quantitative spectroscopy to guide design and optimization of low-cost, compact clinical imaging devices: Emulation and evaluation of multispectral imaging systems. *J. Biomed. Opt.* **2018**, *23*, 1–12. [[CrossRef](#)] [[PubMed](#)]
36. Jimenez, J.; Scully, T.; Barbosa, N.; Donner, C.; Alvarez, X.; Vieira, T.; Matts, P.; Orvalho, V.; Gutierrez, D.; Weyrich, T. A practical appearance model for dynamic facial color. *ACM Trans. Graph. (Proc. SIGGRAPH Asia)* **2010**, *29*, 141:1–141:10.
37. Iglesias-Guitian, J.A.; Aliaga, C.; Jarabo, A.; Gutierrez, D. A Biophysically-Based Model of the Optical Properties of Skin Aging. *Comput. Graph. Forum* **2015**, *34*, 45–55, doi:10.1111/cgf.12540. [[CrossRef](#)]
38. Lapray, P.J.; Thomas, J.B.; Gouton, P. High Dynamic Range Spectral Imaging Pipeline For Multispectral Filter Array Cameras. *Sensors* **2017**, *17*. [[CrossRef](#)] [[PubMed](#)]
39. Delgado Atencio, J.A.; Jacques, S.L.; Montiel, S.V. *Monte Carlo Modeling of Light Propagation in Neonatal Skin*; InTech: London, UK, 2011.
40. Hiltunen, J. Munsell Book of Color: Matte Finish Collection Measured by J. Hiltunen. 2019. Available online: <https://www.uef.fi/web/spectral/munsell-colors-matt-spectrofotometer-measured> (accessed on 2 December 2018).
41. Munsell Color. *Munsell Book of Color: Matte Finish Collection*; Munsell Color: Baltimore, MD, USA, 1976.
42. Cooksey, C.C.; Allen, D.W.; Tsai, B.K. Reference Data Set of Human Skin Reflectance. *J. Res. Natl. Inst. Stand. Technol.* **2017**, *122*, 1–5. [[CrossRef](#)]
43. Publication, CIE. *CIE 15: Technical Report: Colorimetry*, 3rd ed.; CIE Cent. Bur.: Vienna, Austria, 2004; Volume 3.
44. Hardeberg, J.Y. Acquisition and Reproduction of Color Images: Colorimetric and Multispectral Approaches. Ph.D. Thesis, Ecole Nationale Supérieure des Télécommunications, Paris, France, 1999.
45. Imai, F.H.; Berns, R.S. Spectral estimation using trichromatic digital cameras. In Proceedings of the International Symposium on Multispectral Imaging and Color Reproduction for Digital Archives, Chiba, Japan, 21–22 October 1999; Volume 42, pp. 1–8.

46. Shimano, N.; Terai, K.; Hironaga, M. Recovery of spectral reflectances of objects being imaged by multispectral cameras. *J. Opt. Soc. Am. A* **2007**, *24*, 3211. [[CrossRef](#)]
47. Shimano, N.; Hironaga, M. Recovery of spectral reflectances of imaged objects by the use of features of spectral reflectances. *J. Opt. Soc. Am. A* **2010**, *27*, 251–258. [[CrossRef](#)]
48. Stigell, P.; Miyata, K.; Hauta-Kasari, M. Wiener estimation method in estimating of spectral reflectance from RGB images. *Pattern Recognit. Image Anal.* **2007**, *17*, 233–242. [[CrossRef](#)]
49. Nishidate, I.; Maeda, T.; Niizeki, K.; Aizu, Y. Estimation of Melanin and Hemoglobin Using Spectral Reflectance Images Reconstructed from a Digital RGB Image by the Wiener Estimation Method. *Sensors* **2013**, *13*, 7902–7915. [[CrossRef](#)] [[PubMed](#)]
50. Heikkinen, V.; Lenz, R.; Jetsu, T.; Parkkinen, J.; Hauta-Kasari, M.; Jääskeläinen, T. Evaluation and unification of some methods for estimating reflectance spectra from RGB images. *J. Opt. Soc. Am. A* **2008**, *25*, 2444–2458. [[CrossRef](#)] [[PubMed](#)]
51. Lapray, P.J.; Thomas, J.B.; Gouton, P.; Ruicheck, Y. Energy balance in Spectral Filter Array camera design. *J. Eur. Opt. Soc.-Rapid Publ.* **2017**, *13*, 1. [[CrossRef](#)]
52. Thomas, J.B. Illuminant estimation from uncalibrated multispectral images. In Proceedings of the 2015 Colour and Visual Computing Symposium (CVCS), Gjøvik, Norway, 25–26 August 2015; pp. 1–6. [[CrossRef](#)]
53. Wang, X.; Thomas, J.B.; Hardeberg, J.Y.; Gouton, P. Multispectral imaging: Narrow or wide band filters? *JAIC J. Int. Colour Assoc.* **2014**, *12*, 44–51.
54. Khan, H.A.; Thomas, J.B.; Hardeberg, J.Y.; Laligant, O. Illuminant estimation in multispectral imaging. *J. Opt. Soc. Am. A* **2017**, *34*, 1085–1098. [[CrossRef](#)]
55. Randeberg, L.L.; Winnem, A.; Blindheim, S.; Haugen, O.; Svaasand, L. Optical classification of bruises. *Proc. SPIE* **2004**, *5312*, 54–64. [[CrossRef](#)]
56. Humphreys, K.; Ward, T.; Markham, C. A CMOS camera-based pulse oximetry imaging system. In Proceedings of the 2005 IEEE Engineering in Medicine and Biology 27th Annual Conference, Shanghai, China, 17–18 January 2006; pp. 3494–3497.
57. Kong, L.; Yi, D.; Sprigle, S.; Wang, F.; Wang, C.; Liu, F.; Adibi, A.; Tummala, R. Single sensor that outputs narrowband multispectral images. *J. Biomed. Opt.* **2010**, *15*. [[CrossRef](#)]
58. Spigulis, J.; Oshina, I.; Berzina, A.; Bykov, A. Smartphone snapshot mapping of skin chromophores under triple-wavelength laser illumination. *J. Biomed. Opt.* **2017**, *22*, 091508. [[CrossRef](#)]
59. Bauer, J.R.; Bruins, A.A.; Hardeberg, J.Y.; Verdaasdonk, R.M. A Spectral Filter Array Camera for Clinical Monitoring and Diagnosis: Proof of Concept for Skin Oxygenation Imaging. *J. Imaging* **2019**, *5*. [[CrossRef](#)]
60. Day, D. *Spectral Sensitivities of the Sinarback 54 Camera*; Technical Report; Munsell Color Science Laboratory, Chester F. Carlson Center for Imaging Science, Rochester Institute of Technology: Rochester, NY, USA, 2003.
61. Bauer, J.R.; Pedersen, M.; Hardeberg, J.Y.; Verdaasdonk, R. Skin color simulation - review and analysis of available Monte Carlo-based photon transport simulation models. *Color Imaging Conf.* **2017**, *2017*, 165–170.
62. Jacques, S. Origins of tissue optical properties in the UVA, visible, and NIR regions. *Adv Opt Imaging Photon Migr.* **1996**, *2*, 364–369.
63. Jacques, S.L.; Prahl, S.A. A Collaboration of Oregon Health & Science University, Portland State University, and the Oregon Institute of Technology. Optical Spectra, 2015. Available online: <https://www.omlc.org> (accessed on 2 December 2018).
64. IEC. *International Standard: International Electrotechnical Commission*; IEC 61966-2-1:1999; IEC: Geneva, Switzerland, 1999.



© 2019 by the authors. Licensee MDPI, Basel, Switzerland. This article is an open access article distributed under the terms and conditions of the Creative Commons Attribution (CC BY) license (<http://creativecommons.org/licenses/by/4.0/>).

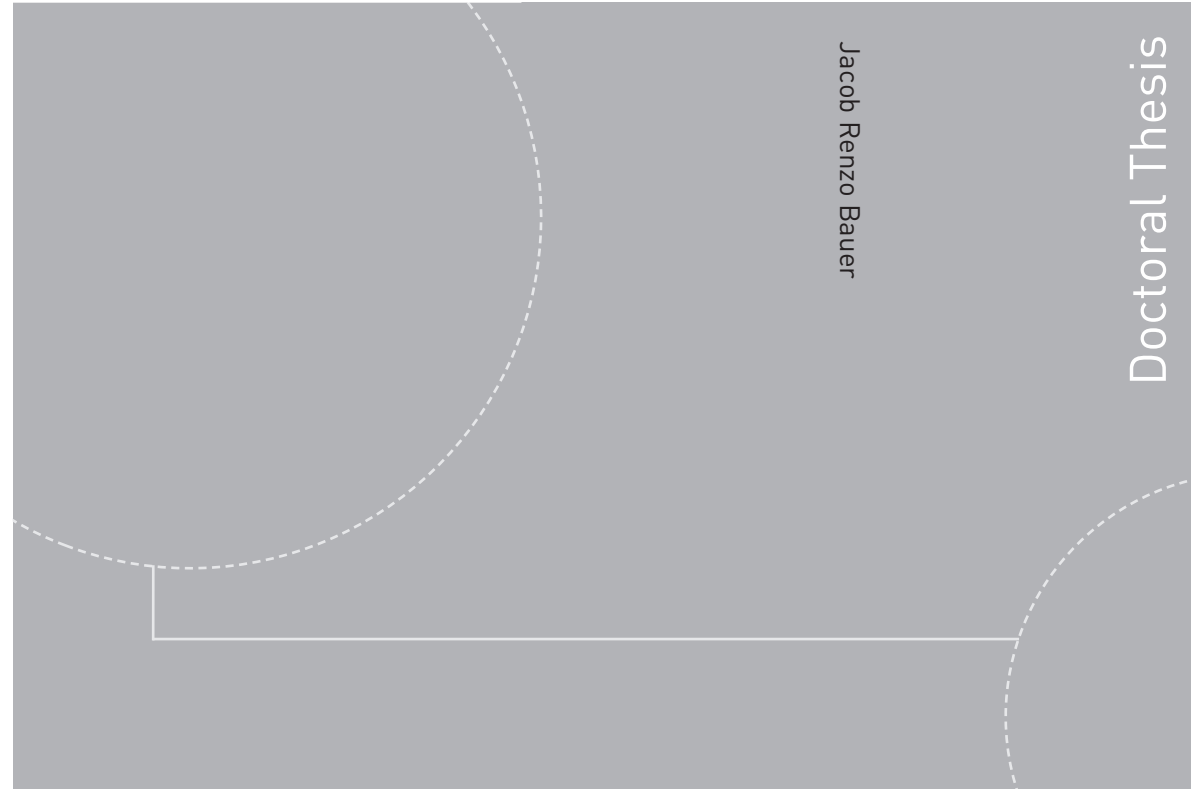
The vascular occlusion test using multispectral imaging: a validation study.

Paper F

*This chapter is a reprint of the publication: Arnoud A. Bruins; Diederik G.P.J. Geboers; Jacob R. Bauer; John H.G.M. Klaessens; Rudolf M. Verdaasdonk; Christa Boer; “The vascular occlusion test using multispectral imaging: a validation study.” *Journal of Clinical Monitoring and Computing* (2020).*

This Paper is not included due to copyright available at <https://doi.org/10.1007/s10877-019-00448-z>

ISBN 978-82-326-4464-3 (printed version)
ISBN 978-82-326-4465-0 (electronic version)
ISSN 1503-8181



Doctoral theses at NTNU, 2020:55

Jacob Renzo Bauer

Spectral filter array cameras as a diagnostic skin imaging tool

Doctoral theses at NTNU, 2020:55

NTNU
Norwegian University of
Science and Technology
Faculty of Information Technology
and Electrical Engineering
Department of Computer Science

 **NTNU**
Norwegian University of
Science and Technology

 NTNU

 **NTNU**
Norwegian University of
Science and Technology